The Influence of Temperature Fluctuations on Dust Formation in Dust Driven Winds of Asymptotic Giant Branch Stars

vorgelegt von
Dipl.-Phys. Vasco Schirrmacher
aus Berlin

Von der Fakultät II - Mathematik und Naturwissenschaften
der Technischen Universität Berlin
zur Erlangung des akademischen Grades
Doktor der Naturwissenschaften
– Dr. rer. nat. –

genehmigte Dissertation

Promotionsausschuss:

Vorsitzender: Prof. Dr. Harald Engel
Berichter: Prof. Dr. Erwin Sedlmayr
Berichterin: Prof. Dr. Heike Rauer

Tag der wissenschaftlichen Aussprache: 19. Oktober 2007

Berlin 2007

D 83

Contents

List of Symbols

Table 1: List of symbols

Symbol	Unit	Description	Section
a	–	dimensionless particle radius	2.1.6
a_ℓ	–	lower edge of the particle size distribution function in units of a	2.1.6
$a_{\max}$	–	size of the biggest dust particle	2.1.6
$a_{\rm grav}$	cm s^{-2}	gravitational deceleration of a fluid element	2.3
$a_{\rm rad}$	cm s^{-2}	radiative acceleration of a fluid element	2.3
$a_{\rm tot}$	cm s^{-2}	total acceleration of a fluid element	2.3
$\underline{\underline{A}}$	–	matrix containing the net growth rates (see Eq. 2.50)	2.2.1
A_1	cm^2	(hypothetical) surface of a monomer	–
A_N	cm^2	surface of a grain consisting of N monomers	–
A_T,$A^{\mu\nu}_{\hat{\mathbf{K}}}$, $A^{\mu}_{T\hat{\mathbf{K}}}$	–	coefficients for the second derivatives of the Fokker-Planck equation (2.41)	2.2.1
$A_{\rho\nu}$	–	matrix elements of $\underline{\underline{A}}$	–
$\mathbf{b}$	–	vector containing the nucleation rates (see Eq. 2.50)	2.2.1
b_i	–	departure coefficient for carbon polymers	2.1.4
b_ρ	–	ρ-th component of the vector $\mathbf{b}$	2.2.1
$b^{\rm c}_{i,m}$	–	generalized departure coefficient for carbon polymers with respect to chemical reactions	2.1.4
B_T,$B^{\mu}_{\hat{\mathbf{K}}}$	–	coefficients for the first derivatives of the Fokker-Planck equation (2.41)	2.2.1
c_0	cm s^{-1}	speed of light in the vacuum	–

List of symbols

Symbol	Unit	Description	Section
$\mathring{c}(N)$	cm^{-3}	equilibium concentration of clusters of size N	2.1.3
$[C/O]$	–	ratio ϵ_C/ϵ_O of carbon and oxygen abundancies	–
$Cov(\cdot,\cdot)$	–	covariance of $(\cdot,\cdot)$	2.2.1
d	–	spatial dimension of the dust grains	2.1.2
D_i	–	dissociation constant of species i	2.1.4
$D_{i,m}$	–	dissociation constant of molecule labeled by i and m	2.1.4
$D^{\mathrm{r}}_{i,m}$	–	dissociation constant of the molecule formed by the backward reaction of the growth reaction m.	2.1.4
$E(\cdot)$	–	expectation value of $(\cdot)$	–
E_{trans}	erg	translational energy of all gas particles	2.3
E_{rot}	erg	rotational energy of the molecules	2.3
E_{vib}	erg	vibrational energy of molecules	2.3
E_{el}	erg	excitation energy of all electrons	2.3
E_{ion}	erg	ionization energy of all ions	2.3
E_{diss}	erg	dissociation energy of all molecules	2.3
f	–	number of the degrees of freedom of the gas	2.3
f_k	–	left hand side of the Fokker-Plank-system 2.66 at the time k	3.2
$f(N,t)$	–	grain size distribution function (per hydrogen core)	–
F	$\mathrm{erg\ s^{-1}\ cm^{-2}}$	frequency integrated radiation flux	3.4
G	$\mathrm{cm^3\ g^{-1}\ s^{-2}}$	gravitational constant	–
$\Delta_{\mathrm{f}}G_1^{\circ}(s)$	$\mathrm{erg\ mol^{-1}}$	standard molar Gibbs free energy of formation of the solid phase	–
$\Delta_{\mathrm{f}}G^{\circ}(1)$	$\mathrm{erg\ mol^{-1}}$	standard molar Gibbs free energy of formation of the monomer	–
H	$\mathrm{erg\ s^{-1}\ cm^{-2}}$	frequency integrated Eddington flux	2.3
H_ν	$\mathrm{erg\ s^{-1}\ cm^{-2}\ Hz^{-1}}$	frequency dependent Eddington flux	2.3
i	–	a) number of monomers that an i-mer consists of	–
		b) index of the dust moments K_{i}	2.1.2

List of symbols

Symbol	Unit	Description	Section
		c) index labeling a particular growth species	2.1.4
I	erg s^{-1} cm^{-2}	frequency integrated light intensity	2.3
I_ν	erg s^{-1} cm^{-2} Hz^{-1}	spectral light intensity	2.3
$I^+(R)$, $I^-(R)$	erg s^{-1} cm^{-2}	intensity of the in- ($I^-(R)$) and outwards ($I^+(R)$) directed radiation in the two stream approximation by Lucy (1971)	2.3.3
j	–	discretized variable of the temperature deviation T during the numerical evaluation of Eq. 2.66	3.2
J_{N_ℓ}	s^{-1}	creation/destruction rate of clusters with size N_ℓ (per hydrogen core)	2.1.2
J_{ev}	s^{-1}	destruction rate of clusters with size N_ℓ (per hydrogen core)	2.1.2
J_*	s^{-1}	stationary nucleation rate (per hydrogen core)	2.1.3
k	–	discretized time variable during the numerical evaluation of Eq. 2.66	3.2
k_{B}	erg K^{-1}	Boltzmann constant	–
K_{i}	–	(deterministic) i-th moment of the grain size distribution function	2.1.2
$\hat{K}_i$	–	random variable for the stochastical modeling of the moment K_{i}	–
$\mathbf{K}$	–	vector containing (K_0, K_1, K_2, K_3)	–
$\hat{\mathbf{K}}$	–	vector containing $(\hat{K_0}, \hat{K_1}, \hat{K_2}, \hat{K_3})$	–
$\mathcal{K}$	–	dust component of the stochastic process $(\Theta, \mathcal{K})_t$	–
$L_\star$	erg s^{-1}	stellar luminosity	–
$L_\odot$	erg s^{-1}	solar luminosity	–
m	–	index labeling particular chemical reaction	2.1.4
m_{u}	g	atomic mass unit	–
$M(R)$	g	mass inside of the radial distance R from the star	2.3
$M_\star$	g	stellar mass	–
$M_\odot$	g	solar mass	–

List of symbols

Symbol	Unit	Description	Section
$n(1)$	cm^{-3}	number density of monomers	2.1.4
$\tilde{n}$	cm^{-3}	equilibrium number density of monomers	2.1.4
$\tilde{n}_{i,m}$	cm^{-3}	equilibrium number density (see $n_{i,m}$)	2.1.4
n_{atoms}	cm^{-3}	number density of atoms	2.3
$n_{\mathrm{molecules}}$	cm^{-3}	number density of molecules	2.3
n_{ions}	cm^{-3}	number density of ions	2.3
$n_{\mathrm{electrons}}$	cm^{-3}	number density of electrons	2.3
n_{c}	cm^{-3}	number density of monomers condensed into dust grains	–
n_{C}	cm^{-3}	number density of C-atoms	–
$n_{\mathrm{C_2}}$	cm^{-3}	number density of C_2-molecules	–
$n_{\mathrm{C_2H}}$	cm^{-3}	number density of C_2H-molecules	–
$n_{\mathrm{C_2H2}}$	cm^{-3}	number density of C_2H_2-molecules	–
n_{d}	cm^{-3}	number density of dust grains	–
n_{H}	cm^{-3}	number density of H-atoms	–
$n_{\mathrm{H_2}}$	cm^{-3}	number density of H_2-molecules	–
$n_{\hat{\mathrm{H}}}$	cm^{-3}	number density of hydrogen cores	–
$n_{i,m}$	cm^{-3}	number density of a growth species which will deposit an i-mer to a grain via the chemical reaction labeled with m	2.1.4
N	–	grain size	–
N_*	–	size of the critical cluster	–
$N_{*,\infty}$	–	parameter to calculate the size of the critical cluster	2.1.3
N_0	–	number of the highest i-mer important for nucleation	2.1.3
N_{d}	–	particle size for which $\sigma_{\mathrm{surf}}(N)$ reduces to one half of the value of σ_{surf} for bulk material	2.1.3
N_ℓ	–	minimum grain size of a macroscopic particle	2.1.2
N_{start}	–	initial value of grid points	3.4
N_{final}	–	final number of grid points	3.4
p	$\mathrm{dyn\ cm}^{-2}$	gas pressure of a fluid element	2.3
$p^{\ominus}$	$\mathrm{dyn\ cm}^{-2}$	pressure of a chemical reference state	–
p_1	$\mathrm{dyn\ cm}^{-2}$	a) gas pressure of the monomer-species	2.1.1

List of symbols

Symbol	Unit	Description	Section
	–	b) one-point probability function	2.2
$\mathring{p}_{\rm sat}(1)$	dyn cm^{-2}	partial pressure of the monomer species in phase equlibrium over a flat surface.	–
$p_{\rm sat}(r)$	dyn cm^{-2}	saturation pressure over a curved surface of radius r	2.1.1
p_∞	dyn cm^{-2}	saturation pressure over a flat surface	2.1.1
p^t	–	joint transition probability density	2.2.1
p^t_T	–	temperature component of the transition probability density	2.2.1
p^t_K	–	conditional transition probability density of the dust component	2.2.1
$p^t_{\mathcal{K}}$	–	transition probability density of the dust component of the stochastical process $(\Theta, \mathcal{K})_t$	2.2.1
$P(\omega)$	–	relative intensity of a wave with angular frequency ω, that is part of the fluctuation field	2.2.2
Q_ρ	–	ρ-th moment of $p_1(t, T, \hat{\mathbf{K}})$ acc. to Eq. (2.56)	2.2.1
$\dot{Q}$	erg g^{-1} s^{-1}	net heating/cooling rate	2.3
$\dot{Q}_{\rm ad}$	erg g^{-1} s^{-1}	net heating/cooling rate via hydrodynamical compression/expansion	2.3
$\dot{Q}_{\rm rad}$	erg g^{-1} s^{-1}	net radiative heating/cooling rate	2.3
$\dot{Q}_{\rm vis}$	erg g^{-1} s^{-1}	viscous heating rate by dissipation	2.3
$Q'(T_{\rm dust})$	–	extinction efficiency of the dust	3.4
$q_\rho(t, T)$	–	conditional expectation value of the random variable $\hat{K}_\rho$ at the time t under the condition T (see Eq. (2.64)	2.2.1
r	cm	grain radius	2.1.1
r	cm	position of a fluid element at the moment t_0	2.3
r_0	cm	(hypothetical) grain radius of a monomer	–
$r_{\rm crit}$	cm	(hypothetical) radius of the critical cluster	–
R	cm	radial position of a fluid element	2.3

List of symbols

Symbol	Unit	Description	Section
$R_\star$	cm	stellar radius in the rest position of the piston	2.3
$\mathcal{R}$	erg mol^{-1} K^{-1}	universal gas constant	2.1.3
$\mathbb{R}_0^+$	–	the set of positive real numbers	–
$R_\odot$	cm	solar radius	–
$R_{\rm in}$	cm	radial position of the inner boundary of a dynamical wind model	2.3.3
$R_{\rm out}$	cm	radial position of the outer boundary of a dynamical wind model	2.3.3
$Q'(T_{\rm dust})$	–	extinction efficiency of the dust	3.4
$s_i(N)$	–	sticking coefficient of the i-mer on a grain of size N	–
S	–	supersaturation ratio	–
$S_{\rm crit}$	–	critical supersaturation ratio needed for nucleation from the gas phase	–
t	s	time	–
t_0 t_1,$t_{\rm old}$, ...	s	particular moments in time	–
$t_{\rm pis}$	s	Time for the initial acceleration of the piston	3.4
$t_{\rm rezone}$	s	Time intervall between two rezoning procedures	3.4
Δt	s	numerical time step	3.3
T	K	a) temperature in thermal equilibrium	2.1.1
		b) temperature deviation of the stochastic fluctuation	2.2
$T_{\rm gas}$	K	gas temperature	–
$T_{\rm dust}$	K	dust temperature	–
$\overline{T}$	K	(deterministic) mean temperature	–
$T_{\rm min}$	K	lower boundary of the temperature deviation T	–
$T_{\rm max}$	K	upper boundary of the temperature deviation T	–
$\Delta T_{\rm max}$	K	maximum temperature deviation T	–
v	cm s^{-1}	velocity of a fluid element	2.3
$v_{\rm th}(i)$	cm s^{-1}	mean thermal velocity of an i-mer	
$v_{\rm th}(i,m)$	cm s^{-1}	mean thermal velocity (see $n_{i,m}$)	
$v_{\rm amp,0}$	cm s^{-1}	initial piston amplitude	3.4

List of symbols

Symbol	Unit	Description	Section
V_0	$\mathrm{cm}^3\ \mathrm{g}^{-1}$	specific volume of a fluid element at the moment t_0	2.3
$Var(\cdot)$	–	Variance of the quantity $(\cdot)$	–
Z	–	Zeldovich factor	2.1.3
yr	s	solar year	–
$\alpha(R)$	–	radiative acceleration in units of the local gravitational deceleration	2.3
α_i	–	sticking coefficient of the i-mer from a flat surface	–
$\alpha_*(i)$	–	coefficient describing non-TE effects in the homogeneous particle growth	2.1.4
$\alpha_\mathrm{c}(i,m)$,$\alpha_m^\mathrm{c}(i)$	–	reaction efficiency for chemical particle growth	2.1.4
$\overset{\circ}{\alpha}_\mathrm{c}(i,m)$	–	TE-reaction efficiency for chemical particle growth in thermal equilibrium	2.1.4
$\alpha_*^\mathrm{c}(i,m)$	–	coefficient describing non-TE effects in the chemical particle growth	2.1.4
β	s^{-1}	rate of i-mers impinging on a cluster of size N	2.1.3
$\beta_\mathrm{c}(i,m)$	–	reaction efficiency for the reverse reactions for chemical particle growth	2.1.4
$\overset{\circ}{\beta}_\mathrm{c}(i,m)$	–	TE-reaction efficiency for the reverse reactions for chemical particle growth in thermal equilibrium	2.1.4
γ	–	numerical parameter, which determines the maximum numerical temperature deviation ΔT_max	–
γ_ad	–	adiabatic exponent	3.3
Γ	–	random "force" describing the temperature fluctuation in Eq. (2.44)	2.2.1
$\delta(\cdot)$	–	delta distribution	–
ϵ_C	–	carbon abundancy	–
$\epsilon_{\mathrm{C},0}$	–	carbon abundancy of the dust free gas	–
ϵ_P	–	fraction of the period P for maximum time step	3.4
ϵ_CFL	–	*Courant-Friedrichs-Levy*-factor	3.4

List of symbols

Symbol	Unit	Description	Section
$\epsilon_{a_{\max}}$	–	maximum relative change of the particle sizes per time step	3.4
$\epsilon_{\kappa_{\rm d}}$	–	maximum relative change of the dust extinction $\kappa_{\rm d}$ per time step	3.4
$\epsilon_{\rm K_0}$	–	maximum relative change of the number of dust particles per time step	3.4
$\epsilon_{\rm K_3}$	–	maximum relative change of the 3$^{\rm rd}$ dust moment per time step	3.4
ϵ_T	–	maximum relative change of $T_{\rm gas}$ per time step	3.4
$\eta_{\rm opt}$	K^{-1}	parameter for the calculation of the dust opacity	2.3.4
$\kappa_{\rm gas}$	cm^2 g^{-1}	frequency integrated gas opacity	2.3.4
$\kappa_{\rm dust}$	cm^2 g^{-1}	frrequency integrated dust opacity	2.3.4
λ	s	correlation time of a fluctuation	–
μ	$m_{\rm u}$	a) molecular mass	2.1
	–	b) index labeling the μ-th random variable $\hat{K}_\mu$	2.2
μ_r	–	cosine of the separation angle dividing the solid angle into two domains with the intensities $I^+(R)$, and $I^-(R)$.	2.3.3
ν	–	index of $\hat{K}_\nu$, $A_{\rho\nu}$, ...	2.2
ρ	g cm^{-3}	a) mass density	–
		b) index of K_ρ, $A_{\rho\nu}$, ...	–
$\overline{\rho}$	g cm^{-3}	(deterministic) mean mass density	–
$\rho_{\rm corr}(s,t)$	–	correlation of the stochastic process Θ	–
σ	K	rms temperature deviation of a fluctuation	–
$\sigma_{\rm B}$	erg cm^{-2} s^{-1} K^{-4}	Stefan-Boltzmann constant	2.3.3
$\tilde{\sigma}$	K s^{-1}	scaling factor of the random term in the Langevin equation (2.44)	2.2.1
$\sigma_{\rm surf}$	erg cm^{-2}	surface tension	2.1
τ^{-1}	s^{-1}	net growth rate (per dust particle per monomer surface)	–
$\tau_{\rm gr}^{-1}$	s^{-1}	growth rate (per dust particle per monomer surface)	–

List of symbols

Symbol	Unit	Description	Section
τ_{ev}^{-1}	s^{-1}	evaporation rate (per dust particle per monomer surface)	–
θ	–	numerical parameter to switch between implicit $\theta = 0$ or explicit $\theta = 1$ integration	3.2
θ_N	K	parameter needed for the description of the surface contribution to the free energy difference between monomers and clusters of size N	2.1.3
θ_∞	K	parameter needed for the calculation of θ_N	2.1.3
Θ	–	temperature component of the stochastic process $(\Theta, \mathcal{K})_t$	2.2.1
Θ_0	–	initial condition of the stochastic process Θ_t	2.2.1
Θ_t^{OU}	–	Ornstein Uhlenbeck process with parameter t	2.2.1
χ_{H}	cm^{-1}	flux weighted extinction coefficient	2.3
ω	s^{-1}	angular frequency	2.2.2

Table 2: Natural constants

Symbol	Value	Description
c_0	2.9979250×10^{10} cm s^{-1}	speed of light
k_{B}	1.380622×10^{-16} erg cm K^{-1}	Boltzmann constant
G	6.6732×10^{-8} cm^3 g^{-1} s^{-2}	gravitational constant
m_{u}	1.660531^{-24} g	atomic mass unit
m_{H}	1.008 m_{u}	mass of a hydrogen atom
m_{C}	12.01 m_{u}	mass of a carbon atom
$L_\odot$	3.82×10^{33} erg s^{-1}	solar luminosity
$M_\odot$	1.989×10^{33} g	solar mass
$\mathcal{R}$	8.314472×10^{-7} erg mol^{-1} K^{-1}	universal gas constant
$R_\odot$	6.96×10^{10} cm	solar radius
yr	3.1556952×10^7 s	solar year
π	3.1415926536	Archimedes' constant
σ_{B}	5.66961×10^{-5} erg cm^{-2} s^{-1} K^{-4}	Stefan-Boltzmann constant

List of Figures

List of Tables

Chapter 1

Introduction

In this work, the influence of temperature fluctuations on the dust formation in dust driven winds of Asymptotic Giant Branch (AGB) stars is investigated.

AGB-stars are intermediate mass stars in a late stage of their stellar evolution. They are usually unstable against radial pulsations, which develop in their convective stellar envelope. Furthermore, AGB-stars often develop strong stellar winds, which are driven by radiation pressure on dust, which forms in their pulsationally elevated atmospheres. These winds lead to a substantial mass-loss of the star, which results in an evolution of the AGB-star to a planetary nebula with a White Dwarf – the former core of the AGB-star – as its central object.

The dust driven winds of AGB-stars play a central role for the evolution of intermediate mass stars. Furthermore, they constitute an important input of dust grains and heavy elements into the interstellar medium, and play a key role in the modelling of the chemical evolution of galaxies.

Since the main driving mechanism of these dust-driven winds is the radiation pressure from the stellar radiation on the newly formed dust particles, the details of the dust condensation process are important for a quantitative analysis of these objects.

A standard method to investigate the physical processes in AGB-winds are self-consistent numerical model calculations, that solve the coupled equations of hydrodynamics, thermodynamics, radiative transfer, chemistry and time dependent dust nucleation, growth, and evaporation for pulsating AGB-stars (see Fleischer et al. 1992; Fleischer 1994; Winters et al. 1997; Woitke et al. 1999; Jeong et al. 2003; Schirrmacher et al. 2003; Dorfi & Höfner 1991; Gautschy-Loidl et al. 2004; Woitke 2006). Despite the fact, that the stellar pulsations originate inside the turbulent convective stellar envelope, the influence of temperature fluctuations has, so far, been ignored. The spatial and temporal resolution of such numerical hydrodynamical calculations is

limited, and any processes that take place on time scales shorter than the numerical time-steps, or on spatial scales smaller than the typical grid zones must be described by subgrid models of these processes. In this context, the possible presence of fluctuations is usually ignored by saying, that all presented numerical quantities represent *mean values*, which are averaged over all subgrid scales. While this assumption is usually very good for hydrodynamical processes, and leads to realistic hydrodynamical wind structures, the complete neglection of the influence of possible temperature fluctuations can lead to quite large errors for processes, which show a strong asymmetric temperature dependence, like chemical reaction networks, or the nucleation and growth of dust particles.

The key feature, that motivates the investigation of the interplay of dust formation and temperature fluctuations, is the circumstance, that the seed particles will only nucleate from the gas phase, if the supersaturation ratio exceeds a certain critical value $S_{\rm crit}$, while an existing dust particle will continue to grow also at moderate supersaturations. Since, the supersaturation ratio S depends very sensibly on the temperature, a situation is realised, where the presence of temperature fluctuations could lead to substantial dust condensation in a situation, where no dust nucleation would occur under the assumption, that the *mean* temperature represents the *real* temperature on all subgrid scales.

In order to investigate the influence of the temperature fluctuations, the dust formation is first formulated as a stochastic process using a formalism developed by Dirks (2000). This formulation leads to a system of Fokker-Planck equations for the probability distribution of the moments of the grain-size distribution function. Since this set of Fokker-Planck equations cannot be implemented directly into self-consistent numerical model calculations describing an AGB-wind, a series of gasbox-calculations is presented, in order to investigate i) of what order of magnitude the temperature fluctuations would have to be in order to have a remarkable influence on the dust formation, and ii) at which time-scales of the correlation time a microturbulent description of the fluctuation is admissible. The gasbox-models are also compared with Monte-Carlo simulations of the same stochastic process. Guided by the results of these gasbox-calculations, a one-parametric microturbulent approach is developed and implemented into self-consistent, time-dependent numerical model calculations. Subsequently, a large number of dynamical wind models was calculated and evaluated. The results are ambivalent, depending on the details of the underlying microscopic description of the gas. For an ideal monoatomic gas with an LTE-cooling function, the results show a clear trend of increasing massloss rates with an increasing strength of the

temperature fluctuations. For models with a more sophisticated gas model combined with tabulated NLTE-cooling functions, this trend was not as clear.

This work is embedded in the scientific work of the Zentrum für Astronomie und Astrophysik (ZAA) of the Technical University of Berlin in several ways. The investigation of dust formation in astrophysical situations has a long standing tradition at the ZAA, in particular the development of a method, which describes the dust complex by moments of the grain-size distribution function (see, e.g. Gail et al. 1984; Gail & Sedlmayr 1985, 1987a, 1988, 1987b; Patzer et al. 1998), has made it possible to implement a time dependent description of dust nucleation, growth, and evaporation into self-consistent hydrodynamical model calculations of AGB-stars (see, e.g. Fleischer et al. 1992; Winters et al. 1994b; Fleischer et al. 1995; Winters et al. 1995; Arndt et al. 1997; Schirrmacher et al. 2003; Jeong et al. 2003), and other astrophysical objects like Brown Dwarfs (see, e.g. Helling et al. 2001, 2003), or RCorBor-stars (see, e.g. Goeres & Sedlmayr 1992; Woitke et al. 1994). The stochastic description of the dust formation applied in this work was developed by Dirks (2000) based on a similar method for the stochastic treatment of radiative transfer developed by Gail et al. (1975b), (see also Gail et al. 1976, 1980, 1975a; Gail & Sedlmayr 1974). One idea of this work is to find a way to make the stochastic dust description developed by Dirks (2000) suitable for implementation into self-consistent hydrodynamical model calculations. Since, with the so-called CHILD-code, a running and well-tested code for the self-consistent time-dependent modelling of carbon rich AGB-winds is available at the ZAA, it seemed a natural choice, to aim for an implementation of the stochastic dust description into this code.

The structure of this work is as follows. In Chapter 2 the basic physical concepts are presented and discussed, in Chapter 3 the numerical methods used in this work are described, the results of the gasbox models are presented in Chapter 4 and discussed in Chapter 5. Guided by these results, the construction of a tables for a microturbulent nucleation rate is described in Chapter 6. This microturbulent nucleation rate is then implemented into self-consistent dynamical wind calculations, the results of which are presented in Chapter 7 and discussed in Chapter 8. Finally, a summary of this work and an outlook for a possible future development is given in Chapter 9.

Chapter 2

Basic Physical Concepts

2.1 Dust formation in astrophysical situations

Dust is found in a wide variety of astrophysical situations - from planetary atmospheres to the intergalactic space. Whenever dust is present in a hydrodynamic medium, it dominates its optical appearance, because it effectively absorbs visible light and reradiates the energy as thermal IR-emission, an effect which can be observed as extinction of the light of distant stars in the main plane of the milky way. This affects not only the optical appearance of many astrophysical objects, but can also dominate their energy balance: the collapse of an interstellar cloud to a protostar, for example, requires the cooling effect of dust, which consists in the circumstance, that dust grains cool by radiating in the IR, and are subsequently reheated by collisions with the gas, which in turn has no effective way of cooling by radiation at the temperatures typical for interstellar clouds.

Moreover, dust is not only important for the energetical and momentum coupling between a hydrodynamical medium and a trespassing radiation-field, it also plays a very important role for the chemistry of the gas, acting as a catalyzer for many chemical reactions: the formation of H_2 from atomic hydrogen at typical interstellar densities, for example, would take longer than the typical life time of a cool molecular cloud. The ability of dust grains to collect interstellar atoms and molecules on their surface, and moreover the ability of the solid bulk material of the grain to absorb the excess energies of exothermic reactions considerably enhance the potential of the interstellar material to produce complex organical and anorganical molecules.

In this work, I used the dust moment method, developed by Gail, Keller, & Sedlmayr (1984) in the form described by Gauger et al. (1990), where dust formation is described as a two step process consisting in grain nucleation

and subsequent growth to macroscopic particles. In this section, I want to resume the microphysical model presented in Gail et al. (1984) and Gauger et al. (1990) and the references therein, in order to make clear how exactly the dust moments $K_{\rm i}$, the nucleation rate J_{N_ℓ} and the net growth rate τ^{-1} are calculated throughout this work, and especially how they depend on the thermodynamical input parameters $T_{\rm gas}$, $T_{\rm dust}$, and ρ which will be the free variables in all hydrodynamical studies presented in chapters 4, and 7.

A carbon rich situation is assumed, i.e. it is assumed that the number density of carbon atoms is higher than that of oxygen atoms. Thus, due to the high binding energy of the CO-molecule, the oxygen will be effectively locked in CO and is therefore not available for the formation of high temperature condensates, which could condense to solid grains under astrophysical thermodynamical conditions. Grains will then be formed only by the excess carbon, which is not locked in CO. Physical objects where a carbon rich dust chemistry is observed are, for example, C-stars, i.e. stars during the late stages of their evolution along the *Asymptotic Giant Branch* (AGB) or WC-stars, i.e. carbon rich *Wolf-Rayet*-stars.

Mathematically, the formation, growth and evaporation of dust particles are described by the time development of moments of the particle size distribution $f(N,t)$. In order to be able to describe the dust complex via a one dimensional distribution function, which depends on the particle size N only, i.e. on the number of monomers that form the particular grains, it is obviously necessary to assume, that the grains actually consist of a number of identical monomers and of these identical monomers only[1]. Therefore, the carbon is assumed to condensate to graphite clusters. The formation of carbon rich dust via *PolyAromatic Hydrocarbons* (PAH's) cannot be investigated in the framework of this method, because the resulting grains are not likely to consist of similar monomers, which prevents the description via a distribution function of the form $f(N,t)$. Already the description of dust nucleation via PAH's would require the investigation of the chemical pathway leading to the critical cluster (see e.g. Goeres 1993), a task which goes well beyond the scope of this work. For the same reason, the method cannot be applied straight forward to an oxygen-rich situation, where dust formation takes place via inhomogeneous growth, and the need of keeping track of the stoichiometric composition of the grains, requires the use of a more sophisticated distribution function. (A deterministic self-consistent model of an O-rich AGB star is presented by Jeong et al. 2003, .)

[1]The method assumes that the grains *consist* of identical monomers, this does not require that nucleation, growth and destruction are described by processes involving monomers only. Indeed, in this work not only C-atoms, but also C_2, C_2H and C_2H_2 are assumed as species contributing to nucleation and growth via chemical reactions.

2.1.1 Some general remarks about condensation processes

The saturation pressure $p_{\rm sat}(r)$ over a curved surface is always greater than that over a flat surface p_∞. In thermal equilibrium $p_{\rm sat}$ is given by the *Thomson-Helmholtz*-equation:

$$\ln\left(\frac{p_{\rm sat}(r)}{p_\infty}\right) = \frac{2\sigma_{\rm surf}\mu m_{\rm u}}{r\rho k_{\rm B}T}, \tag{2.1}$$

where $\sigma_{\rm surf}$ is the surface tension and $\mu m_{\rm u}$ the mass of the monomer. Thus, for a set of thermodynamic variables (T,ρ) there will be a specific grain size $r_{\rm crit}$ at which grains will be in stable phase equilibrium with the gas phase.

Grains of the size $r_{\rm crit}$ are called critical clusters. Grains smaller than the critical cluster will evaporate, whereas grains larger than the critical cluster will grow by catching monomers from the gas phase. Since the condensable material in the gas is depleted by the growth process of the particles larger than $r_{\rm crit}$, $r_{\rm crit}$ will increase according to Eq. (2.1) leading to the evaporation of more grains and so on, until an equilibrium between the new solid phase and the depleted gas establishes, where the partial pressure of the monomers corresponds to the saturation pressure over the solid surface, while the partial pressures of the remaining i-mers should be in chemical equilibrium (CE) with the monomers.

The supersaturation ratio is defined as the ratio between the partial pressure of the monomer p_1 and the pressure of a saturated vapour of a flat surface p_∞:

$$S = \frac{p_1}{p_\infty} \tag{2.2}$$

This definition of the supersaturation ratio yields the problem, that in a situation with $S = 1$ the self-nucleation of particles from the gas phase is impossible, because the size of the critical cluster would be infinite. Thus, for nucleation to take place in a seed free environment, a finite supersaturation $S_{\rm crit} > 1$ is required, which should be of that order of magnitude, that allows the barrier of the critical cluster $r_{\rm crit}(S)$ size to be reached by a chemical fluctuation process. However, for the reasons sketched above, this state of supersaturation is intrinsically thermodynamically unstable, because the newly formed seeds will immediately start growing und thus, deplete the gas phase from condensable monomers. As a rule of thumb, the "easier" the dust nucleation takes place, the less particles form, because the growth of the big supercritical particles will usually consume the material faster, than the formation of the critical clusters, which constitutes a bottle neck of the reaction chain.

The fact, that nucleation is a phenomenon of a thermodynamical (and chemical) non-equilibrium situation yields the problem, that the description of this state via equilibrium quantities alone might not be sufficient to catch the essential aspects of the process.

2.1.2 The grain size distribution function

The grain size distribution function $f(N,t)$ yields the number of grains of size N at the moment in time t per hydrogen core[2]. $f(N,t)$ carries the complete information about the dust complex at a given moment in time. All other physical quantities concerning the dust complex can be derived by the knowledge of $f(N,t)$. For this purpose, it is very helpful to define the following moments of the distribution function (see e.g. Gauger et al. 1990, Eq. 1)[3]:

$$K_{\mathrm{i}}(t) = \sum_{N_\ell}^{\infty} N^{i/d} f(N,t), \tag{2.3}$$

with N_ℓ corresponding to the lower size limit of the distribution function, i.e. to the minimum cluster size of a macroscopic particle. d is the spatial dimension of the particle. In this work, all particles are assumed to be spherical, i.e. $d = 3$. The first four moments are:

$$\begin{aligned} K_0(t) &= \sum_{N_\ell}^{\infty} f(N,t), \\ K_1(t) &= \sum_{N_\ell}^{\infty} N^{1/3} f(N,t), \\ K_2(t) &= \sum_{N_\ell}^{\infty} N^{2/3} f(N,t), \\ K_3(t) &= \sum_{N_\ell}^{\infty} N f(N,t). \end{aligned} \tag{2.4}$$

These moments can be used to express the following physical quantities (see Gail et al. 1984, Eq.3.4 – 3.8):

[2]The quantities are normalised to the total number density of hydrogen cores $n_{\hat{\mathrm{H}}} = n_{\mathrm{H}} + 2n_{\mathrm{H_2}} + \ldots$. Thereby the moments K_{i} are independent of the local mass density and of the dissociative state of the gas.

[3]The hats used by Gauger et al. are omitted in this work.

1. particle density n_d of grains of size $\geq N_\ell$:

$$n_\mathrm{d} = K_0,$$

2. average grain radius:

$$\langle r \rangle = r_0 \frac{K_1}{K_0},$$

with r_0 as the (hypothetical) radius of a monomer,

3. average grain surface:

$$\langle A_N \rangle = 4\pi r_0^2 \frac{K_2}{K_0},$$

4. average particle size:

$$\langle N \rangle = \frac{K_3}{K_0},$$

5. number density n_c of monomers condensed into grains of size $\geq N_\ell$:

$$n_\mathrm{c} = K_3.$$

In principle, the moments K_i carry the same information as the distribution function $f(N,t)$ itself, but only, if *all* moments are taken into account, i.e. $i = -\infty, \ldots, -1, 0, 1, 2, \ldots, +\infty$. However, for the description of the dust complex at the theoretical depth desired in this work, the first four moments are sufficient (see Gail et al. 1984).

The time evolution of the first four dust moments is given by (see Gauger et al. 1990, Eq. 40)

$$\frac{dK_0}{dt} = J_{N_\ell} \tag{2.5a}$$

$$\frac{dK_\mathrm{i}}{dt} = N_\ell{}^{\frac{i}{d}} J_{N_\ell} + \frac{i}{d}\frac{1}{\tau} K_{\mathrm{i}-1}. \tag{2.5b}$$

In the case of dust growth, J_{N_ℓ} is the creation rate of clusters of size N_ℓ. It is then assumed that J_{N_ℓ} corresponds to the stationary nucleation rate J_* calculated according to classical nucleation theory (see Gail & Sedlmayr 1984, and references therein). In the case of dust evaporation, J_{N_ℓ} is the corresponding destruction rate. In contrast to the nucleation rate, the destruction rate is a function of the dust distribution function $f(N,t)$ itself, because the amount of grains, that can be destroyed in a particular situation

will obviously depend strongly on the amount and size of the grains present at the particular moment. The actual calculation of the grain destruction rate is described in Sect. 2.1.6.

τ^{-1} corresponds to the net growth rate, i.e. it also includes the effects of dust destruction. In this work, dust destruction is assumed to take place via thermal evaporation and chemical sputtering. If other processes should be included, it must be checked whether their dependence on the grain-size allows an inclusion into τ^{-1}. Otherwise, a mathematical treatment using the moments of the distribution function might no longer be possible.

Mathematically, Eq. (2.5a) is a closing condition for the equation system Eq. (2.5b), so that the moments with negative i's do not have to be evaluated. Another closing condition for the upper moments is not needed, since the K_i depend only on lower moments and J_{N_ℓ}, but not on any higher moments. Nevertheless, for obvious physical reasons, the consumption of carbon in the gas phase by condensation to the solid phase must be taken into account, which gives another equation linking the chemical abundance of carbon cores in the gas phase ϵ_C to the moment K_3

$$\epsilon_\mathrm{C}(t) = \epsilon_{\mathrm{C},0} - K_3(t), \tag{2.6}$$

where $\epsilon_{\mathrm{C},0}$ is the carbon-core abundance of the dust-free situation.

2.1.3 Nucleation

In the framework of classical nucleation theory (e.g. Feder et al. 1966), the nucleation process is regarded as a random walk problem of clusters in the cluster size space. A cluster that has reached the *critical cluster size* will most probably continue to grow to macroscopic dimensions. Smaller clusters are more likely to reevaporate. Therefore, the *nucleation rate* J_* is assumed to be the formation rate of critical clusters in a quasi stationary equilibrium situation. *Stationary* in this case means, that the clusters are assumed to grow fast from the critical size N_* to the size N_ℓ - the minimum size of a macroscopic particle, which is also the lower edge for the calculation of the moments K_i. This rate is given by (see Gail et al. 1984, Eq. 2.17)

$$J_*^s = \beta A_N Z \overset{\circ}{c}(N_*) \tag{2.7}$$

where A_N denotes the surface of a grain of size N, and β denotes the rate of i-mers growing onto a cluster of size N

$$\beta = \sum_{i=1}^{N_0} v_{th}(i)\overset{\circ}{c}(i)i^{2/3}s_i(N) \text{ (see also Gail et al. 1984, Eq.2.14)} \quad (2.8)$$

$$= \sum_{i=1}^{N_0} \sqrt{k_{\rm B}T_{\rm gas}/2\pi m_{\rm u}i}\overset{\circ}{c}(i)i^{2/3}\alpha_i \quad (2.9)$$

$$= \sqrt{k_{\rm B}T_{\rm gas}/2\pi}\sum_{i=1}^{2}\frac{\alpha_i}{\sqrt{m_{\rm u}i}}i^{2/3}\overset{\circ}{c}(i), \quad (2.10)$$

N_0 is the highest i-mer that plays a role in the nucleation process. In Eq. (2.9) the sticking coefficient $s_i(N)$ from Eq. (2.8) has been approximated by the evaporation coefficient α_i of the i-mer from a flat graphite-surface. Z is the *Zeldovich*-factor (see Gail et al. 1984, Eq. 2.18)

$$Z = \left(\frac{1}{2\pi}\frac{\partial^2 \ln \overset{\circ}{c}}{\partial N^2}\bigg|_{N_*}\right)^{1/2}. \quad (2.11)$$

$\overset{\circ}{c}(N)$ is the equilibrium distribution of dust grains of size N in thermal equilibrium (see Gail et al. 1984, Eqs. 2.6, 2.9, and 2.7)

$$\overset{\circ}{c}(N) = n_1 \exp\left\{(N-1)\ln S - \frac{\theta_N}{T}(N-1)^{2/3}\right\}, \text{with} \quad (2.12)$$

$$\theta_N = \frac{\theta_\infty}{1+\left(\frac{N_{\rm d}}{N-1}\right)^{1/3}}, \text{and} \quad (2.13)$$

$$\theta_\infty = \sigma_{\rm surf}4\pi r_0^2/k_{\rm B}, \quad (2.14)$$

where $\sigma_{\rm surf}$ is the surface tension of the grains material, $N_{\rm d}$ is the particle size for which $\sigma_{\rm surf}(N)$ reduces to one half of the value of $\sigma_{\rm surf}$ for bulk material, and N_* is the critical cluster size calculated by (see Gail et al. 1984, Eqs. 2.15 and 2.16)

$$N_* = 1 + \frac{N_{*,\infty}}{8}\left\{1+\left[1+2\left(\frac{N_\ell}{N_{*,\infty}}\right)^{1/3}\right]^{1/2} - 2\left(\frac{N_\ell}{N_{*,\infty}}\right)^{1/3}\right\}^3 \quad (2.15)$$

$$N_{*,\infty} = \left(\frac{2\theta_\infty}{3T\ln S}\right)^3, \quad (2.16)$$

and S is the supersaturation ratio given by

$$S = \frac{n_1 k_{\rm B}T}{p_{\rm sat}} = \frac{p_1}{p_{\rm sat}}, \quad (2.17)$$

with the particle density of the monomers n_1, their corresponding partial pressure p_1 and the saturation pressure p_{sat} of the monomers with respect to the grain. In this work, p_{sat} is approximated by the saturation pressure of monomers in phase equilibrium over a flat surface $\overset{\circ}{p}_{\mathrm{sat}}(1)$ (see Patzer et al. 1998, Appendix A)

$$\overset{\circ}{p}_{\mathrm{sat}}(1) = \exp\left(\frac{\Delta_{\mathrm{f}}G_1^{\circ}(s) - \Delta_{\mathrm{f}}G^{\circ}(1)}{\mathcal{R}T}\right) p^{\circ}. \tag{2.18}$$

p° denotes the pressure of the standard state, $\Delta_{\mathrm{f}}G_1^{\circ}(s)$ is the standard molar Gibbs free energy of formation of the solid phase (referred to the standard state), and $\Delta_{\mathrm{f}}G^{\circ}(1)$ is the standard molar Gibbs free energy of formation of the monomer. The temperature used in (Eq. 2.18) corresponds to the temperature of the solid, which is supposed to be in thermal equilibrium with the gas phase. If the condition of thermal equilibrium is violated, the gas and the solid phase can have different temperatures. In this case, the pressure p_1 of the monomers must be calculated using the gas temperature T_{gas}, while the saturation pressure p_{sat} should be calculated with the dust temperature T_{dust}. Since the influence of the dust temperature on the supersaturation ratio is very strong, I want to make some remarks to the choice of the value for this temperature.

- In the case of local thermal equilibrium (LTE, see Sect. 4.1) the situation is simple: dust and gas have per definition the same temperature $T_{\mathrm{dust}} = T_{\mathrm{gas}}$.

- In non-LTE situations, T_{dust} might depend on the particle size $T_{\mathrm{dust}} = T_{\mathrm{dust}}(N)$. However, for the moment method we need to assume that $T_{\mathrm{dust}}(N)$ is constant for $N > N_\ell$, because otherwise the validity of Eq. (2.5b) breaks down. One choice in this work for T_{dust} is, for example, the deterministic mean temperature $\overline{T}$, a choice which corresponds to the assumption that the grains do not follow the fluctuations of the gas temperature, (see Sect. 4.2). In the dynamical calculations presented in Chapter. (7), T_{dust} is usually set to the radiation temperature T_{rad} for the calculation of the growth rate τ^{-1}, because under conditions typical for AGB star winds the energetic coupling of the macroscopic grains to the radiation field is stronger than that to the surrounding gas.

- For the calculation of the nucleation rate however, the essential temperature is that of the *critical* cluster. Since the critical cluster is very small, in most parts of this work, its temperature is assumed to be equal

to the gas temperature $T_{\rm gas}$. Therefore, in most cases, the supersaturation ratio for the nucleation rate is calculated with $T_{\rm dust} = T_{\rm gas}$. In order to investigate the influence of the temperature of the critical cluster on the nucleation rate some models were calculated with $T_{\rm dust} = \overline{T}$ for the nucleation rate. These results are presented in Sect. (4.2).

Throughout this entire work, the supersaturation ratio S is calculated using a fitting polynomial based on molecular data from the JANAF-tables, calculated by H.-P. Gail, in the version that is used in the CHILD-Code (e.g. Fleischer et al. 1992; Fleischer 1994; Schirrmacher et al. 2003).

2.1.4 Growth and Evaporation Rates

In principle, the net growth rate τ^{-1} is calculated according to Eq. (18) from Gauger et al. (1990), assuming C, C_2, C_2H and C_2H_2 as growth species, it is the difference between the (pure) growth rate $\tau_{\rm gr}^{-1}$ and the evaporation rate $\tau_{\rm ev}^{-1}$

$$\tau^{-1} = \tau_{\rm gr}^{-1} - \tau_{\rm ev}^{-1}.$$

According to Eq. (20) from Gauger et al. (1990), the growth rate $\tau_{\rm gr}^{-1}$ is given by

$$\begin{aligned} \tau_{\rm gr}^{-1} &= \sum_{i=1}^{I} iA_1 v_{\rm th}(i)\alpha(i)f(i,t) + \\ &\quad \sum_{i=1}^{I'} iA_1 \sum_{m=1}^{M_i} v_{\rm th}(i,m)\alpha_m^{\rm c}(i)n_{i,m}. \end{aligned} \tag{2.19}$$

i is the number of monomers added to an arbitrary cluster, m labels the individual chemical reactions contributing to the grain growth, $A_1 = 4\pi r_0^2$ is the (hypothetical) monomer surface, $v_{\rm th}$ is the mean thermal velocity of the corresponding species, $\alpha(i)$ and $\alpha_m^{\rm c}(i)$ are the sticking coefficients of the corresponding species. Note, that in this approach the growth rate is independent from the size of the growing clusters, if this was not the case, Eq. (2.5b) would lose its validity. Assuming as growth processes

a) the homogeneous growth by association of C and C_2 onto the cluster surface (first term in Eq. 2.19) and

b) the chemical growth via the reactions (second term in Eq. 2.19) : $C_{N-2} + C_2H \rightarrow C_N + H$ and $C_{N-2} + C_2H_2 \rightarrow C_N + H_2$

Eq. 2.19 becomes

$$\begin{aligned}\tau_{\rm gr}^{-1} &= A_1 v_{\rm th,C}\alpha_{\rm C} n_{\rm C} + \\ &\quad 2A_1 v_{\rm th,C_2}\alpha_{\rm C_2} n_{\rm C_2} + \\ &\quad 2A_1 v_{\rm th,C_2H}\alpha^{\rm c}_{\rm C_2H} n_{\rm C_2H} + \\ &\quad 2A_1 v_{\rm th,C_2H_2}\alpha^{\rm c}_{\rm C_2H_2} n_{\rm C_2H_2}.\end{aligned} \tag{2.20}$$

Using

$$v_{\rm th}(i) = \sqrt{\frac{k_{\rm B}T_{\rm gas}}{2\pi m_i}}, \tag{2.21}$$

we obtain:

$$\tau_{\rm gr}^{-1} = A_1\sqrt{\frac{kT_{\rm gas}}{2\pi}}\left\{\frac{\alpha_{\rm C}}{\sqrt{m_{\rm C}}}n_{\rm C} + 2\left(\frac{\alpha_{\rm C_2}}{\sqrt{m_{\rm C_2}}}n_{\rm C_2} + \frac{\alpha_{\rm C_2H}}{\sqrt{m_{\rm C_2H}}}n_{\rm C_2H} + \frac{\alpha_{\rm C_2H_2}}{\sqrt{m_{\rm C_2H_2}}}n_{\rm C_2H_2}\right)\right\}. \tag{2.22}$$

According to Gauger et al. (1990) (Eq. 21), the evaporation rate $\tau_{\rm ev}^{-1}$ is given by

$$\begin{aligned}\tau_{\rm ev}^{-1} &= \sum_{i=1}^{I} iA_1 v_{\rm th}(i)\alpha_i f(i,t)\frac{1}{S^i}\frac{1}{b_i}\alpha_*(i) + \\ &\quad \sum_{i=1}^{I'} iA_1 \sum_{m=1}^{M_i} v_{\rm th}(i,m)\alpha^{\rm c}_m(i) n_{i,m}\frac{1}{S^i}\frac{1}{b^{\rm c}_{i,m}}\alpha^{\rm c}_*(i,m).\end{aligned} \tag{2.23}$$

The $\alpha_*(i)$, $\alpha^{\rm c}_*(i,m)$, b_i and $b^{\rm c}_{i,m}$ are quantities describing non-TE effects (see Gail & Sedlmayr 1988, Eq. (18) and Eq. (22)); the evaluation of these coefficients is discussed in section 2.1.5.

Assuming as destruction processes

a) the evaporation of C or C_2 from the grain (first term in Eq. 2.23) or

b) chemical sputtering via the reactions (second term in Eq. 2.23) $C_N + H \rightarrow C_{N-2} + C_2H$ and $C_N + H_2 \rightarrow C_{N-2} + C_2H_2$,

Eq. 2.23 becomes

$$\begin{aligned}\tau_{\rm ev}^{-1} &= A_1 v_{\rm th,C}\alpha_{\rm C} n_{\rm C}\frac{1}{S}\frac{1}{b_{\rm C}}\alpha_{*,\rm C} + \\ &\quad 2A_1 v_{\rm th,C_2}\alpha_{\rm C_2} n_{\rm C_2}\frac{1}{S^2}\frac{1}{b_{\rm C_2}}\alpha_{*,\rm C_2} + \\ &\quad 2A_1 v_{\rm th,C_2H}\alpha^{\rm c}_{\rm C_2H} n_{\rm C_2H}\frac{1}{S^2}\frac{1}{b_{\rm C_2H}}\alpha_{*,\rm C_2H} + \\ &\quad 2A_1 v_{\rm th,C_2H_2}\alpha^{\rm c}_{\rm C_2H_2} n_{\rm C_2H_2}\frac{1}{S^2}\frac{1}{b_{\rm C_2H_2}}\alpha_{*,\rm C_2H_2}.\end{aligned} \tag{2.24}$$

2.1.5 Chemistry

In order to determine the particle densities of the dust forming species, a description of the chemical processes in the gas in needed. Following a gas kinetic approach would require the solution of a chemical rate network, where all reactions involving a chemical element contributing to the species of interest, contribute with a separate rate equation, balancing forward and backward reaction. Since every rate equation depends on the particle densities of all species involved in the particular reaction, all equations involving a particular species are coupled and have to be solved together. Besides the fact that the solution of such a rate network is very tricky and time consuming, the reaction rate coefficients are usually unknown – especially for astrophysical thermodynamical situations – and available estimates are only very rough approximations. The solution of all these problems goes well beyond the scope of this work.

Therefore, throughout this work, the gas is assumed to be in *chemical equilibrium* (CE), i.e. we expect the chemistry to be in a stationary state, where all forward reactions rates are balanced by the corresponding backward reaction rates. In this case, the local particle density of each species is constant and can be calculated by the *Law of Mass Action*. The partial pressure of each species can then be calculated from the partial pressure of its constituents and a specific constant for the particular species called the *dissociation constant* D. The dissociation constant can be calculated by the forward and backward reaction constants of the chemical reaction. Since atomic species cannot dissociate the corresponding constants can be formally set to 1.

Using the assumption of CE, it is possible to calculate the coefficients $\alpha_*^{\mathrm{c}}(i,m)$, b_i and $b_{i,m}^{\mathrm{c}}$ describing the non-equilibrium effects, introduced in section 2.1.4.

Taking Eq. (18) from Gail & Sedlmayr (1988)

$$\alpha_*(N,i) = \frac{\mathring{\alpha}(N-i,i,T_{\mathrm{dust}})}{\alpha(N-i,i)} \sqrt{\left(\frac{T_{\mathrm{dust}}(N)}{T_{\mathrm{gas}}}\right)}, \tag{2.25}$$

the quotient of the rate coefficients $\mathring{\alpha}(N-i,i,T_{\mathrm{dust}})/\alpha(N-i,i)$ becomes 1 (in CE), and neglecting the size dependence of the dust temperature (cf. section 2.1.3) the $\alpha_*(i)$ can be approximated by

$$\alpha_*(i) = \alpha_* = \sqrt{\frac{T_{\mathrm{dust}}}{T_{\mathrm{gas}}}}. \tag{2.26}$$

According to Gail & Sedlmayr (1988) (Eq. 22), the coefficients $\alpha_*^{\rm c}(i,m)$ are given by

$$\alpha_*^{\rm c}(i,m) = \frac{\mathring{\alpha}_{\rm c}(i,m)}{\alpha_{\rm c}(i,m)} \frac{\beta_{\rm c}(i,m)}{\mathring{\beta}_{\rm c}(i,m)} \tag{2.27}$$

where the "circled" quantities are the equilibrium rates of clusters of size i growing onto a grain[4] via the reaction m; the "uncircled" quantities describe the *real* rate, i.e. in CE $\alpha = \mathring{\alpha}$ and $\beta = \mathring{\beta}$ and therefore

$$\alpha_*^{\rm c}(i,m) = 1. \tag{2.28}$$

The departure coefficients b_i and $b_{i,m}^{\rm c}$ are calculated according to Appendix A from Gauger et al. (1990). Eq.(A9) therein states

$$b_i = \left(\frac{n(1)}{\tilde{n}(1)}\right)^{-i} \frac{n(i)}{\tilde{n}(i)} \frac{D_i(T_{\rm gas})}{D_i(T_{\rm dust})} \frac{T_{\rm dust}}{T_{\rm gas}}. \tag{2.29}$$

This time, the $\tilde{n}$ stand for the equilibrium values, while the n are the "real" values; again in CE we have $\tilde{n} = n$, the first two terms become unity, and we get

$$\begin{aligned} b_i &= \frac{D_i(T_{\rm gas})}{D_i(T_{\rm dust})} \frac{T_{\rm dust}}{T_{\rm gas}}, \qquad (2.30)\\ b_{\rm C} &= 1 \cdot \frac{T_{\rm dust}}{T_{\rm gas}}\,, \text{ because C is an atomic species,}\\ b_{\rm C_2} &= \frac{D_{\rm C_2}(T_{\rm gas})}{D_{\rm C_2}(T_{\rm dust})} \frac{T_{\rm dust}}{T_{\rm gas}}. \end{aligned}$$

Eq. (A12) from Gauger et al. (1990) states

$$b_{i,m}^{\rm c} = \left(\frac{n(1)}{\tilde{n}(1)}\right)^{-i} \frac{\left(\frac{n_{i,m}}{\tilde{n}_{i,m}}\right)}{\left(\frac{n_{i,m}^{\rm r}}{\tilde{n}_{i,m}^{\rm r}}\right)} \frac{\left(\frac{D_{i,m}(T_{\rm gas})}{D_{i,m}(T_{\rm dust})}\right)}{\left(\frac{D_{i,m}^{\rm r}(T_{\rm gas})}{D_{i,m}^{\rm r}(T_{\rm dust})}\right)}, \tag{2.31}$$

again the first two terms involving the deviation of the particle densities from CE vanish; $D_{i,m}^{\rm r}$ is the dissociation constant of the molecule formed by the backward reaction of the growth reaction m. Considering the chemical

[4]Like in Gauger et al. (1990) the dependence of these quantities from the grain size N is neglected in this work.

growth via the reactions $C_{N-2}+C_2H \rightarrow C_N+H$ and $C_{N-2}+C_2H_2 \rightarrow C_N+H_2$ and chemical sputtering via the corresponding reverse reactions, we obtain:

$$b^{\rm c}_{C_2H} = \frac{\frac{D_{C_2H}(T_{\rm gas})}{D_{C_2H}(T_{\rm dust})}}{\frac{1}{1}} = \frac{D_{C_2H}(T_{\rm gas})}{D_{C_2H}(T_{\rm dust})} \tag{2.32}$$

$$b^{\rm c}_{C_2H_2} = \frac{\frac{D_{C_2H_2}(T_{\rm gas})}{D_{C_2H_2}(T_{\rm dust})}}{\frac{D_{H_2}(T_{\rm gas})}{D_{H_2}(T_{\rm dust})}} = \frac{D_{C_2H_2}(T_{\rm gas})D_{H_2}(T_{\rm dust})}{D_{C_2H_2}(T_{\rm dust})D_{H_2}(T_{\rm gas})}.$$

2.1.6 Dust destruction

In principle, the determination of the dust destruction rate, i.e. the number density of dust grains that shrink by evaporation to a size below N_ℓ, requires the knowledge of the dust distribution function $f(N,t)$. Unfortunately the reconstruction of $f(N,t)$ from its first four moments $K_{\rm i}$ $(i=0,1,2,3)$ alone is usually impossible, which makes it necessary to keep track of the distribution function along the calculation. Gauger, Gail, & Sedlmayr (1990) have presented a method, where the dust destruction is calculated from the history of the evolution of the dust moments $K_{\rm i}$. The key idea of this method is a variable transformation of the equation system (2.5a,2.5b) describing the temporal change of the dust moments $K_{\rm i}$, which will considerably facilitate the treatment of evaporation. The time evolution of the dust moments on the usual time-axis is given by Eq. (2.5a,2.5b)

$$\begin{aligned} \frac{dK_0}{dt} &= J_{N_\ell} \\ \frac{dK_{\rm i}}{dt} &= N_\ell{}^{\frac{i}{d}} J_{N_\ell} + \frac{i}{d}\frac{1}{\tau}K_{\rm i-1}. \end{aligned} \tag{2.33}$$

Introducing the dimensionless particle radius a by

$$a = N^{\frac{1}{d}} \tag{2.34}$$

the change of a of for a given dust particle is given by

$$\frac{da}{dt} = \frac{1}{d}\frac{1}{\tau}\left(= \frac{1}{3}\frac{1}{\tau}\right). \tag{2.35}$$

The important point for the applicability of the described method is the fact that the temporal change of the dimensionless particles radius da/dt for any given particle is *independent* of its current value a, i.e. da/dt is equal for *all* particles in a given volume element and the physical processes of growth or evaporation correspond to a constant shift of the whole distribution function

$f(a,t)$ in the a-space[5]. A direct consequence of this behaviour is that the shape of the function (and all of its moments K_i) remains untouched except for the "material" inserted by nucleation or removed by grain destruction at the lower edge a_ℓ. It is therefore very useful to perform a variable transformation on the equation system (Eq. 2.5b). Instead of the variable t, a variable a_max corresponding to the maximum particle radius of the grains in a given volume element is introduced. At a given point in time t_0, when the condensation process sets in, the maximum particle radius will be that corresponding to the cluster size $a_\ell = N_\ell^{\frac{1}{3}}$, therefore $a_\mathrm{max}(t_0) = a_\ell$. For an uninterrupted growth process, each point in time t_1 after t_0 can be labelled by the particular value of the size of the biggest particle $a_\mathrm{max}(t_1)$, irrespective of how erratic the growth process may have proceeded in time:

$$a_\mathrm{max}(t_1) = \frac{1}{d}\int_{t_0}^{t_1} \frac{1}{\tau(t')} dt' + a_\ell. \tag{2.36}$$

During the phase of dust growth, the time evolution $K_\mathrm{i}(t)$ is stored as a function of a_max, i.e. as $K_\mathrm{i}(a_\mathrm{max})$. In a phase of evaporation, the dimensionless particle size of the biggest grain a_max shrinks in exactly the same way as all others, namely according to Eq. (2.35). Since in the a-space all particles shrink exactly alike, the effect on the K_i is the same, as if they had never grown to a_max. The evaporation process corresponds to a shift of the dust distribution $f(a, a_\mathrm{max})$ to smaller a by an amount $\mathrm{d}a = 1/3\tau^{-1}\mathrm{d}t$. Thus, in case of evaporation, the new dust moments $K_\mathrm{i}(t_\mathrm{new})$ can be calculated by simply restoring them to their value at the time corresponding to $K_\mathrm{i}(a_\mathrm{max}(t_\mathrm{new}))$, after $a_\mathrm{max}(t_\mathrm{new})$ has been calculated according to Eq. (2.35). The dust destruction rate J_ev is then given implicitly by

$$J_\mathrm{ev} = \frac{1}{\Delta t}\left(K_0(t_\mathrm{old}) - K_1(t_\mathrm{new})\right). \tag{2.37}$$

2.1.7 Input data needed for the dust description

Table 2.1 gives an overview of the material data required for the calculation of dust nucleation, growth and evaporation.

[5]Obviously the newly formed dust needs to be inserted at the lower edge.

Table 2.1: Material constants required for the dust calculation

Symbol	Value	Source	Description
α_i	$\alpha_{\rm C} = 0.37$ $\alpha_{\rm C_2} = 0.34$	Hölzel et al. (1968)	sticking coefficients (actually the data in Hölzel et al. (1968) correspond to the evaporation coefficients.)
$\log(\epsilon_{\rm H})$ $\log(\epsilon_{\rm He})$ $\log(\epsilon_{\rm O})$ $\epsilon_{\rm C}$	0.00 -1.00 -3.18 $\epsilon_{\rm C} = [C/O]\,\epsilon_{\rm O}$	Allen (1973) Allen (1973) Allen (1973)	hydrogen abundance helium abundance oxygen abundance carbon abundance, usually given by the parameter $[C/O]$
r_0 A_1	0.128 nm $A_1 = 4\pi r_0^2$ $=20.7\ 10^{-16}$ cm^2	Gail et al. (1984)	hypothetical monomer radius hypothetical monomer surface
$\sigma_{\rm surf}$ $N_{\rm d}$	1400 erg cm^{-}2 5	Gail et al. (1984) Gail et al. (1984), Eq. (5.4)	surface tension of the grain material particle size for which $\sigma_{\rm surf}(N)$ reduces to one half of the value of $\sigma_{\rm surf}$ for bulk material
D_i,$D_{i,m}$		Chase Jr. et al. (1985) (JANAF)	dissociation constants
$\Delta_{\rm f}G_1^{\circ}(s)$ $\Delta_{\rm f}G^{\circ}(1)$		Chase Jr. et al. (1985) (JANAF) Chase Jr. et al. (1985) (JANAF)	standard molar Gibbs free energy of formation of the solid phase standard molar Gibbs free energy of formation of the monomer

2.2 Temperature Fluctuations

Fluctuations are ubiquitous in the universe. They can, for example, be a result of various types of waves, stellar convection or turbulent velocity fields. In the circumstellar envelopes (CSE) of AGB stars, turbulent dissipation of the shock waves, that originate from the stellar pulsation, and steepen up in the outer atmosphere, seems to be a good candidate for causing temperature fluctuations. Furthermore, it has to be pointed out, that the stellar pulsation itself is generated in the convective stellar[6] envelope, which also makes it plausible to assume the presence of fluctuations.

Due to the limited spatial resolution of hydrodynamical model calculations, fluctuations that occur on scales smaller than the scale of the grid cannot be resolved by the code. Usually, these fluctuations are ignored by interpreting all hydrodynamical quantities as *mean values* averaged over any subgrid structure. Whereas this procedure gives usually good results for typical hydrodynamical investigations, the complete ignorance of any small scale thermodynamical features might camouflage the possibility of certain chemical processes that are very sensitive to temperature fluctuations. Especially dust formation in a dust free situation, which requires a high supersaturation ratio $S \gg 1$ for nucleation, whereas the growth of the dust particles will continue as long as there is *any* supersaturation $S > 1$, yields the possibility that the use of averaged values for the temperature might strongly underestimate the potential of the circumstellar gas to form dust out of the gas phase.
Since

- there is no satisfactory theory for describing the exact nature of the temperature fluctuations induced by convection, turbulence or dissipation, and
- a later application for hydrodynamical sub-grid modeling will require a description which depends on a few parameters only,

in this work, an approach is chosen, which describes the fluctuations by two parameters: σ, the rms temperature deviation, and λ the correlation time of the fluctuations. It is *not* the scope of this work to determine values of these parameters from the physical processes that might cause the fluctuations, but to investigate the influence of the temperature fluctuations on the dust formation, in order to answer questions like:

- How large would temperature fluctuations have to be, in order to have a significant impact on the dust formation?

[6] The *circumstellar* envelope is a region outside the star, starting above the photosphere, the *stellar* envelope lies inside the star below the photosphere

- How large would temperature fluctuations have to be, in order to have a significant impact to the hydrodynamical structure of a stellar wind?
- What influence do the time-scales of the fluctuations have?

The approach presented in the following sections, will help to answer these questions for simple gas box models (see Sect. 4) and guided by these answers a method will be presented in Sect. 6 which will allow for the inclusion of the effects of temperature fluctuations into self-consistent time-dependent models of AGB-star winds (see Sect. 7).

2.2.1 Description of the fluctuations

The stochastic approach presented in this section has been developed by Dirks (2000), based on works from Gail, Sedlmayr, & Traving (1975b) (also Gail et al. 1976, 1980) about a stochastic formulation of the radiative transfer problem. In this section, I will give a brief summary of the method in order to discuss the implications of the necessary assumptions in Sect. 2.2.2.

Starting from a parametrised description of the temperature fluctuations as a Markov-process, in this section, a 6-dimensional Fokker-Planck equation (2.55) will be derived that describes the time development of the one-point probability $p_1(t, T(t), \hat{\mathbf{K}}(t))$, which gives the probability of finding a certain value

$$\hat{\mathbf{K}} := (\hat{K}_0, \hat{K}_1, \hat{K}_2, \hat{K}_3) \tag{2.38}$$

at a given moment in time t under the condition

$$T_{\text{gas}}(t) = \overline{T}(t) + T(t). \tag{2.39}$$

Note that in Eq.(2.39) as in the rest of this section T denotes a temperature deviation and not the gas temperature T_{gas} itself, i.e. T can have positive and negative values. $\overline{T}$ stands for a deterministic mean temperature.

In the end of this section, that Fokker-Planck equation is transformed into a set of four 2-dimensional Fokker-Planck equations for adequately defined moments of p_1, which is better suited for the subsequent numerical treatment.

Modeling the fluctuations as a stochastic process

The fluctuations are modeled via a 5-dimensional stochastic process $(\Theta, \mathcal{K})_t; t \in \mathbb{R}_0^+$. The paths of this process represent the possible joint evolutions of the five random variables T, $\hat{K}_0$,$\hat{K}_1$,$\hat{K}_2$, and $\hat{K}_3$ for the temperature deviation and the dust moments:

$$(\Theta, \mathcal{K})_t(T, \hat{\mathbf{K}}) = (T, \hat{K}_0, \hat{K}_1, \hat{K}_2, \hat{K}_3)(t). \tag{2.40}$$

Note, that the $\hat{K}_\rho$ denote the random variables of the stochastic process, whereas the K_ρ stand for the deterministic moments of the grain-size distribution function as presented in Chapter 2.1. It is assumed that the process $(\Theta, \mathcal{K})_t$ is a Markov process, i.e. for any given moment in time t, any future values of $(T, \hat{\mathbf{K}})(t_{\text{fut}})$ with $t_{\text{fut}} > t$ do not depend on the history of the process $(T, \hat{\mathbf{K}})(t_{\text{past}})$ with $t_{\text{past}} < t$.

Under these circumstances, a Fokker-Planck equation for the one-point probability $p_1(t, T, \hat{\mathbf{K}})$ can be derived (see Dirks 2000):

$$\begin{aligned}\frac{\partial p_1(t,T,\hat{\mathbf{K}})}{\partial t} &= -\frac{\partial(p_1(t,T,\hat{\mathbf{K}})\,B_T)}{\partial T} - \frac{\partial(p_1(t,T,\hat{\mathbf{K}})\,B^\mu_{\hat{\mathbf{K}}})}{\partial \hat{K}_\mu} \\ &+ \frac{1}{2}\frac{\partial^2(p_1(t,T,\hat{\mathbf{K}})\,A_T)}{\partial T^2} + \frac{1}{2}\frac{\partial^2(p_1(t,T,\hat{\mathbf{K}})\,A^{\mu\nu}_{\hat{\mathbf{K}}})}{\partial \hat{K}_\mu\,\partial \hat{K}_\nu} + \frac{\partial^2(p_1(t,T,\hat{\mathbf{K}})\,A^\mu_{T\hat{\mathbf{K}}})}{\partial \hat{K}_\mu\,\partial T},\end{aligned} \tag{2.41}$$

using the sum convention for the Greek indices $\mu, \nu = 0, 1, 2, 3$. The coefficient functions for μ, ν and $\delta > 0$ are defined by the following infinitesimal moments (see again Dirks 2000). For a better readability the dependency of p^t on t, T, $\hat{\mathbf{K}}$ and Δt, ΔT, $\Delta\hat{\mathbf{K}}$: is omitted in Eq. 2.42:

$$B_T(t,T,\hat{\mathbf{K}}) = \lim_{\Delta t\to 0}\frac{1}{\Delta t}\iint\limits_{\|(\Delta T,\Delta\hat{\mathbf{K}})\|<\delta} \Delta T\,p^t\,\mathrm{d}\Delta T\,\mathrm{d}^4\Delta\hat{\mathbf{K}}, \tag{2.42a}$$

$$B^\mu_{\hat{\mathbf{K}}}(t,T,\hat{\mathbf{K}}) = \lim_{\Delta t\to 0}\frac{1}{\Delta t}\iint\limits_{\|(\Delta T,\Delta\hat{\mathbf{K}})\|<\delta} \Delta\hat{K}_\mu\,p^t\,\mathrm{d}\Delta T\,\mathrm{d}^4\Delta\hat{\mathbf{K}}, \tag{2.42b}$$

$$A_T(t,T,\hat{\mathbf{K}}) = \lim_{\Delta t\to 0}\frac{1}{\Delta t}\iint\limits_{\|(\Delta T,\Delta\hat{\mathbf{K}})\|<\delta} (\Delta T)^2\,p^t\,\mathrm{d}\Delta T\,\mathrm{d}^4\Delta\hat{\mathbf{K}}, \tag{2.42c}$$

$$A^{\mu\nu}_{\hat{\mathbf{K}}}(t,T,\hat{\mathbf{K}}) = \lim_{\Delta t\to 0}\frac{1}{\Delta t}\iint\limits_{\|(\Delta T,\Delta\hat{\mathbf{K}})\|<\delta} \Delta\hat{K}_\mu\,\Delta\hat{K}_\nu\,p^t\,\mathrm{d}\Delta T\,\mathrm{d}^4\Delta\hat{\mathbf{K}}, \tag{2.42d}$$

$$A^\mu_{T\hat{\mathbf{K}}}(t,T,\hat{\mathbf{K}}) = \lim_{\Delta t\to 0}\frac{1}{\Delta t}\iint\limits_{\|(\Delta T,\Delta\hat{\mathbf{K}})\|<\delta} \Delta\hat{K}_\mu\,\Delta T\,p^t\,\mathrm{d}\Delta T\,\mathrm{d}^4\Delta\hat{\mathbf{K}}. \tag{2.42e}$$

$p^t = p^t(t, T, \hat{\mathbf{K}}, t+\Delta t, T+\Delta T, \hat{\mathbf{K}}+\Delta\hat{\mathbf{K}})$ is the transition probability density that gives the probability of finding the system in the state $(T+\Delta T, \hat{\mathbf{K}}+\Delta\hat{\mathbf{K}})$ at time $t+\Delta t$ under the condition that it was in the state $(T, \hat{\mathbf{K}})$ at the moment t.

For the determination of the coefficients (2.42) of the Fokker-Planck equation (2.41), the transition probability density $p^t(t, T, \hat{\mathbf{K}}, t+\Delta t, T+\Delta T, \hat{\mathbf{K}}+\Delta\hat{\mathbf{K}})$ is required. In order to find an expression for p^t, it is at first assumed that the transition probability density factorises into the transition probability density p^t_{T} for the temperature component of the stochastic process (2.40) and the conditional transition probability $p^t_{\mathrm{K}}(T)$ for the dust moment component:

$$\begin{aligned} p^t(t, T, \hat{\mathbf{K}}, t+\Delta t, T+\Delta T, \hat{\mathbf{K}}+\Delta\hat{\mathbf{K}}) = \\ = p^t_{\mathrm{T}}(t, T, t+\Delta t, T+\Delta T) p^t_{\mathrm{K}}(t, T, \hat{\mathbf{K}}, t+\Delta t, \hat{\mathbf{K}}+\Delta\hat{\mathbf{K}}). \end{aligned} \quad (2.43)$$

Note that p^t_{K} depends on T, whereas p^t_{T} does not depend on $\hat{\mathbf{K}}$. This factorisation of p^t corresponds to the physical assumption (see discussion in Sect. 2.2.2), that the local dust formation at the moment of the fluctuation has no influence on the temperature fluctuation itself. As a consequence, the transition probability densities p^t_{T} and p^t_{K} from (2.43) can be determined separately.

The transition probability of the temperature component

The temperature component Θ of the stochastic process 2.40 is modelled via a Langevin equation

$$\mathrm{d}\Theta(t) = -\frac{1}{\lambda}\Theta(t)\mathrm{d}t + \tilde{\sigma}\Gamma(t)\mathrm{d}t. \quad (2.44)$$

This is a stochastic differential equation, the solutions of which are stochastic processes instead of "ordinary" functions. The first term on the right hand side of Eq. (2.44) describes the tendency of the gas to relax towards a state of equilibrium, which is characterised by $T = 0$, i.e. $T_{\mathrm{gas}} = \overline{T}$. In this context, λ has the meaning of a relaxation time scale. $\Gamma(t)$ denotes a random "force" - in this context rather a random input to the thermal energy of the gas - representing a random fluctuation. $\tilde{\sigma}$ is a scaling factor of this term, describing the "strength" of the fluctuation. Again, the mathematical details of this approach are discussed in Dirks (2000). Here, I just want to state that the stochastic differential equation (2.44) is solved by a Gaussian Markovian Ornstein-Uhlenbeck process Θ^{OU}_t which - with the initial condition

of a normally distributed random variable Θ_0 with the expectation value 0 - has the following properties (see Dirks 2000, Eq. 3.8-3.10)

$$\mathrm{E}(\Theta_t^{\mathrm{OU}}) = 0, \tag{2.45a}$$

$$\mathrm{Var}(\Theta_t^{\mathrm{OU}}) = \frac{1}{2}\lambda\tilde{\sigma}^2 =: \sigma^2 \quad \text{and} \tag{2.45b}$$

$$\mathrm{Cov}(\Theta_s^{\mathrm{OU}}, \Theta_t^{\mathrm{OU}}) = \sigma^2 e^{-\frac{1}{\lambda}|t-s|}, \tag{2.45c}$$

introducing the rms temperature fluctuation σ. The one point probability density of the temperature fluctuation is then given by a Gaussian bell

$$p_1^{\mathrm{T}} = (2\pi\sigma^2)^{\frac{1}{2}} e^{-\frac{T^2}{2\sigma^2}}. \tag{2.46}$$

Furthermore, the correlation function $\rho_{\mathrm{corr}}(s,t)$ of the process is

$$\rho_{\mathrm{corr}}(s,t) = \frac{\mathrm{Cov}(\Theta_s^{\mathrm{OU}}, \Theta_t^{\mathrm{OU}})}{\sqrt{\mathrm{Var}(\Theta_s^{\mathrm{OU}})\mathrm{Var}(\Theta_t^{\mathrm{OU}})}} = e^{-\frac{1}{\lambda}|t-s|}. \tag{2.47}$$

Thus, the parameter λ represents the correlation time of the fluctuations, i.e. the temperature deviations for two moments in time $T(t_1)$ and $T(t_2)$ are correlated on a time scale comparable to λ and practically uncorrelated for $|t_2 - t_1| \gg \lambda$. The coefficients (2.42a) and (2.42c) of the Fokker-Planck equation (2.41) can then be calculated as

$$B_T(t, T, \hat{\mathbf{K}}) = -\frac{1}{\lambda}T \quad \text{and} \tag{2.48a}$$

$$A_T(t, T, \hat{\mathbf{K}}) = 2\frac{\sigma^2}{\lambda}. \tag{2.48b}$$

The transition probability of the dust component

After having determined the coefficients (2.42a) and (2.42c) of the Fokker-Planck equation (2.41), an expression for the conditional transition probability density $p_{\mathrm{K}}^t(T)$ is required in order to calculate the remaining coefficients (2.42b),(2.42d) and (2.42e).

It is assumed, that the random character of the dust component results exclusively as a consequence from the random temperature fluctuation. Thus for small time steps – i.e. $\Delta t \ll \lambda$ – the transition probability density of the dust moments $p_{\mathcal{K}}(T)$ is given by

$$p_{\mathcal{K}}(t, T, \hat{\mathbf{K}}, t + \Delta t, \hat{\mathbf{K}} + \Delta\hat{\mathbf{K}}) = \delta(\Delta\hat{\mathbf{K}} - (\underline{\underline{A}}\hat{\mathbf{K}} + \mathbf{b})_{\mathrm{T}}\Delta t), \tag{2.49}$$

where the term $\underline{\underline{A}}\hat{\mathbf{K}}+\mathbf{b}$ corresponds to the deterministic dust moments equations (2.5a,2.5b) with

$$\underline{\underline{A}} = \begin{pmatrix} 0 & 0 & 0 & 0 \\ \frac{1}{3}\tau^{-1} & 0 & 0 & 0 \\ 0 & \frac{2}{3}\tau^{-1} & 0 & 0 \\ 0 & 0 & \tau^{-1} & 0 \end{pmatrix}, \text{ and} \tag{2.50}$$

$$\mathbf{b} = \begin{pmatrix} J_{\mathrm{N}_\ell} \\ N_\ell{}^{\frac{1}{3}} J_{\mathrm{N}_\ell} \\ N_\ell{}^{\frac{2}{3}} J_{\mathrm{N}_\ell} \\ N_\ell J_{\mathrm{N}_\ell} \end{pmatrix}. \tag{2.51}$$

Using $\underline{\underline{A}}$ and $\mathbf{b}$, Eqs. (2.5a,2.5b) can be written as

$$\frac{\mathrm{d}}{\mathrm{d}t}\mathbf{K} = \underline{\underline{A}} \cdot \mathbf{K} + \mathbf{b}, \tag{2.52}$$

or - for the components of $\mathbf{K}$

$$\frac{\mathrm{d}K_\rho}{\mathrm{d}t} = A_{\rho\nu}K_\nu + b_\rho, \qquad \rho,\nu = 0,1,2,3. \tag{2.53}$$

The coefficients (2.42b),(2.42d) and (2.42e) can now be calculated using Eq. (2.49) (see Dirks 2000, p. 36–39)

$$B^\mu_{\hat{\mathbf{K}}} = A_{\mu\nu}\hat{K}_\nu + b_\mu \quad , \tag{2.54a}$$

$$A^{\mu\nu}_{\hat{\mathbf{K}}} = 0 \quad , \tag{2.54b}$$

$$A_{T\hat{\mathbf{K}}} = 0. \tag{2.54c}$$

After inserting the coefficients (2.48) and (2.54) into the Fokker-Planck equation (2.41) we obtain:

$$\frac{\partial p_1(t,T,\hat{\mathbf{K}})}{\partial t} = \frac{1}{\lambda}\frac{\partial}{\partial T}(Tp_1) + \frac{\sigma^2}{\lambda}\frac{\partial^2 p_1}{\partial T^2} - \frac{\partial}{\partial K_\mu}(p_1(A_{\mu\nu}K_\nu + b_\mu)). \tag{2.55}$$

Transforming the Fokker-Planck Equation

We will now transform the Fokker-Planck equation (2.55) for the probability distribution $p_1(t,T,\hat{\mathbf{K}})$ into a set of four coupled Fokker-Planck equations for adequately defined *moments* of p_1. This will lead to a set of equations (2.66), which will be the basis for our further investigations.

The transformation procedure is identical to that from Dirks (2000) (p. 42), except for the fact, that we do not restrict ourselves to spherically symmetric situations, but stay in the comoving Lagrangian frame.

We define the moments Q_ρ with respect to the random variable K_ρ as

$$Q_\rho := \int \hat{K}_\rho p_1(t, T, \hat{\mathbf{K}}) \mathrm{d}^4\hat{\mathbf{K}} \quad (\rho = 0, \ldots, 3). \tag{2.56}$$

This definition yields

$$\int Q_\rho(t, T)\mathrm{d}T = \iint \hat{K}_\rho p_1(t, T, \hat{\mathbf{K}})\mathrm{d}^4\hat{\mathbf{K}}\mathrm{d}T = \mathrm{E}(\hat{K}_\rho)(t), \tag{2.57}$$

$\mathrm{E}(\hat{K}_\rho)(t)$ being the expectation value of $\hat{K}_\rho$ at the time t.

We now apply the operator $\int \mathrm{d}^4\hat{\mathbf{K}}\hat{K}_\rho$ to Eq. (2.55) for all $\rho = 0, 1, 2, 3$. Thereby we transform the Fokker-Planck equation for the probability density $p_1(t, T, \hat{\mathbf{K}})$ into a set of four coupled Fokker-Planck equations for the four moments Q_ρ of p_1:

$$\begin{aligned} \frac{\partial}{\partial t} Q_\rho &= \frac{1}{\lambda}\left(\frac{\partial}{\partial T} T + \sigma^2 \frac{\partial^2}{\partial T^2}\right) Q_\rho - \\ &\quad \int \frac{\partial}{\partial K_\mu}(p_1(A_{\mu\nu}K_\nu + b_\mu))\hat{K}_\rho \mathrm{d}^4\hat{\mathbf{K}}, \quad \rho = 0, 1, 2, 3. \end{aligned} \tag{2.58}$$

Similar to the treatment from Dirks (2000) we split the last term using $(f'g = (fg)' - fg')$:

$$\begin{aligned} \int \frac{\partial}{\partial K_\mu}(p_1(A_{\mu\nu}K_\nu + b_\mu))\hat{K}_\rho \mathrm{d}^4\hat{\mathbf{K}} &= \\ \int \frac{\partial}{\partial K_\mu}(p_1(A_{\mu\nu}K_\nu + b_\mu)\hat{K}_\rho)\mathrm{d}^4\hat{\mathbf{K}} &- \int p_1(A_{\mu\nu}K_\nu + b_\mu)(\frac{\partial}{\partial K_\mu}\hat{K}_\rho)\mathrm{d}^4\hat{\mathbf{K}}. \end{aligned} \tag{2.59}$$

Using Gauss' Theorem, (still following Dirks), the first term on the rhs. of Eq. (2.59) vanishes

$$\int \frac{\partial}{\partial K_\mu}(p_1(A_{\mu\nu}K_\nu + b_\mu)\hat{K}_\rho)\mathrm{d}^4\hat{\mathbf{K}} = \int_F p_1(A_{\mu\nu}K_\nu + b_\mu)\hat{K}_\rho \mathrm{d}F = 0, \tag{2.60}$$

because the probability distribution p_1 must vanish on the surface of the configuration space, due to its normalisation:

$$\int p_1(t, T, \hat{\mathbf{K}})\mathrm{d}^4\hat{\mathbf{K}} = 1. \tag{2.61}$$

The second term of Eq. (2.59) can be simplified (see Dirks 2000, p. 43):

$$\int p_1(A_{\mu\nu}K_\nu + b_\mu)(\frac{\partial}{\partial K_\mu}\hat{K}_\rho)\mathrm{d}^4\hat{\mathbf{K}} = A_{\rho\nu} + b_\rho p^T. \tag{2.62}$$

Substituting Eq. 2.60 and Eq. 2.62 into Eq. 2.58 gives a set of four equations for the Q_ρ, which are coupled via the $A_{\rho\nu}$:

$$\frac{\partial}{\partial t}Q_\rho = \frac{1}{\lambda}\left(\frac{\partial}{\partial T}T + \sigma^2\frac{\partial^2}{\partial T^2}\right)Q_\rho + A_{\rho\nu}Q_\nu + b_\rho p^T. \tag{2.63}$$

A close inspection of Eq. (2.57) reveals, that the Q_ρ still *contain* the probability distribution p^T. Therefore the values of the Q_ρ(T) will vary by orders of magnitude, depending on the temperature deviation T from the mean temperature – a fact which causes problems during the numerical evaluation. We therefore define the "smoothened" moments

$$q_\rho(t,T) := \frac{Q_\rho(t,T)}{p^T(t,T)}, \tag{2.64}$$

yielding

$$\begin{aligned}\int Q_\rho(t,T)\mathrm{d}T &= \int q_\rho(t,T)p^T(t,T)\mathrm{d}T \\ &= \iint \hat{K}_\rho p_1(t,T,\hat{\mathbf{K}})\mathrm{d}^4\hat{\mathbf{K}}\mathrm{d}T = \mathrm{E}(\hat{K}_\rho)(t).\end{aligned} \tag{2.65}$$

The q_ρ can be interpreted as *conditional expectation values* of the $\hat{K}_\rho$, i.e. the expectation value of $\hat{K}_\rho$ under the condition that the temperature deviation has a value of T.

Inserting Eq. (2.64) into Eq. (2.63) leads us to the final set of Fokker-Planck equations, which we are going to evaluate numerically:

$$\frac{\partial}{\partial t}q_\rho = -\frac{1}{\lambda}T\frac{\partial}{\partial T}q_\rho + \frac{\sigma^2}{\lambda}\frac{\partial^2}{\partial T^2}q_\rho + A_{\rho\nu}q_\nu + b_\rho \tag{2.66}$$

This is a coupled set of equations of Fokker-Planck type, which describes the time development of the conditional expectation values $q_\rho(t)$ of the dust moments $\hat{K}_\rho$. In order to solve the equation system (2.66), we have to provide

1. the parameters σ and λ of the assumed temperature fluctuation,
2. an initial condition $q_{\rho,0}$ for $t = 0$,

3. the boundary paths $q_\rho(T_{\min}, t)$,$q_\rho(T_{\max}, t)$, and
4. a deterministic thermodynamic structure, providing $\overline{T}(t)$, $\overline{\rho}(t)$ on top of which the source terms – $A_{\rho\nu}q_\nu$ and b_ρ, containing nucleation and growth rates – are evaluated.

2.2.2 Discussion of the fluctuation model

In this Section, I want to discuss the physical and mathematical assumptions made during the process of modeling the temperature fluctuations with respect to their physical meaning.

Firstly, I want to discuss the consequences of the decision to describe the temperature fluctuations using the theory of stochastic processes. In contrast to a direct hydrodynamical description of the fluctuations, which temporally resolves the thermodynamical evolution of the fluctuations (see, e.g. Helling et al. 2001), the results obtained with a stochastical approach will always have a statistical character. The solution of the equation system (2.66) will not give information about a particular object, but on the statistical appearance of an ensemble of similar objects. Particular members of this ensemble can behave very differently than the "average" behaviour resulting from the equation system (2.66) might suggest. The correlation time λ divides the family of solutions into three domains:

- **The *microturbulent* domain:** In this domain the fluctuations are very fast compared to the time scales of nucleation and growth of the dust grains. Individual representants of processes solving the equation system (2.66) will usually look very similar to the corresponding expectation value $q_\rho(t)$ – at least if smoothened over the individual member. Within the microturbulent domain, the solution $q_\rho(t)$ from Eq. (2.66) becomes independent of the correlation time λ.

- **The *macroturbulent* domain:** In this case, the fluctuations are very slow compared to the time scales of nucleation and growth of the dust grains. Due to slow relaxation to the equilibrium state, the individual representants of the solution will often show strong deviations from the corresponding expectation values. Once the temperature deviates from the mean value in one way or another, in the macroturbulent case it will tend remain on the same "side" of the mean value.

- **The *mesoturbulent* domain:** This domain lies between the micro- and the macroturbulent case, the correlation time of the fluctuations is of the order of the time scale dominating the evolution of the dust complex.

The microturbulent limit case is of particular interest with respect to finding a subgrid-model for the influence of temperature fluctuations in hydrodynamical calculations, because in this case, the averaged[7] structure of any particular member of the ensemble resembles the structure of the expectation values resulting from Eq. (2.66). If the correlation time λ is considerably shorter than the numerical timestep Δt, the average of a quantity over the time step, corresponds to the expectation value of the quantity resulting of Eq. (2.66) in the microturbulent limit. In this case, the result of Eq. (2.66) becomes independent of λ, and a one-parametric description of the fluctuation depending only on the rms-temperature fluctuation σ is reasonable. It will therefore be a central question during the investigation of Eq. (2.66), for which values of λ the solutions of Eq. (2.66) will reach the microturbulent domain.

Another important assumption, which is essential in deriving Eq. (2.41) is that the stochastic process $(\Theta, \mathcal{K})_t$ is a Markov process. A Markov process is a process "with short memory", in the sense, that for any given moment in time t, the future evolution of the process, depends only on the present values of $(T, \hat{K}_0, \hat{K}_1, \hat{K}_2, \hat{K}_3)(t)$, but not on those in the past. Physically, this is not a dangerous assumption as long as we do not want to include effects, where the evolution of the *individual fluctuation* T of the temperature or of the dust moments $\hat{K}_\rho$ depends for example explicitly on the rate of change of these quantities *during that individual fluctuation*. It does not constitute a problem for the applicability of this method, if the evolution of the *mean* thermodynamic structure $\overline{T}$, $\overline{\rho}$ in a particular astrophysical environment shows any sort of memory effects.

The assumption, that the transition probability p^t is assumed to factorise as $p^t = p^t_{\mathrm{T}} p^t_{\mathrm{K}}(T)$ means, that the evolution of the dust moments *during an individual fluctuation* will not act back on the fluctuation itself. Again, it is perfectly permitted, that the dust formation influences the *mean* thermodynamic structure - which it usually does. In the picture, where we assume the dust formation to take place in an environment which is turbulent, because of dissipation from stellar pulsation waves, this assumption is perfectly fulfilled. It might become problematic in "pathological" situations, like e.g. a turbulence element which is accelerated so strong by radiation pressure on the newly formed dust grains, already during the dust nucleation, that it considerably changes the large scale turbulence field from which it originates itself. For the description of such a case, one would have to fall back onto

[7] *Averaged* in this context has to be understood in the sense of *smoothened*, i.e. for sufficiently small intervals the value of a quantity in that interval is set to the average of that quantity within that particular interval.

a direct hydrodynamical description which temporally and spatially resolves the fluctuation and its large scale environment. However, as already stated above, the origin of the fluctuations is not subject of this work. I therefore want to close the discussion of this aspect with the hint, that, if the fluctuation model presented in the previous section is ever to be applied to a situation where the fluctuations are triggered by the dust formation itself, the assumption of the factorisation of p^t should be subjected to a close reinspection.

During the derivation of the equation system (2.66) we have assumed that the equation system (2.5) can be linearised by Eq. (2.53). This linearisation is only an approximation of the original system (2.5) for two reasons

1. The vector $\mathbf{b}$ should contain the terms which are constant with respect to the K_i. Nevertheless, $\mathbf{b}$ contains the nucleation rate J_{N_ℓ} which depends about linearly on the carbon abundance ϵ_C, which in turn is antiproportional to K_3 (see Eq. 2.6). However this assumption is not as bad as it might seem, because in practice, it is sufficient that Eq. (2.53) is a good approximation for times in the order of the numerical timestep used to evaluate the equation system. Furthermore, the terms including the nucleation rate are usually only important at the beginning of the condensation process, when only little carbon is used up by the condensation, and ϵ_C is practically constant $\epsilon_\mathrm{C} \approx \epsilon_{\mathrm{C},0}$.

2. Another problem occurs in the case of evaporation. Again, the destruction rate J_ev will surely depend on the exact shape of the grain size distribution function $f(N,t)$. However, this term will in general be small compared to the τ_ev term contained in $\underline{\underline{A}}$, unless the evaporation is nearly complete and if the evaporation is finally complete, the moments vanish anyway ($K_\rho = 0$).

The temperature fluctuations are modelled via the Langevin equation 2.44, which is solved by a so called Ornstein-Uhlenbeck process Θ_s^OU. The resulting correlation function (2.47)

$$\rho_\mathrm{corr}(s,t) = \frac{\mathrm{Cov}(\Theta_s^\mathrm{OU}, \Theta_t^\mathrm{OU})}{\sqrt{\mathrm{Var}(\Theta_s^\mathrm{OU})\mathrm{Var}(\Theta_t^\mathrm{OU})}} = e^{-\frac{1}{\lambda}|t-s|}.$$

implies a power-law spectrum of the form (see Böger et al. 2003)

$$P(\omega) \sim \frac{\lambda}{1+\lambda^2\omega^2}. \tag{2.67}$$

where ω denotes the angular frequency a wave constituting the fluctuation field and $P(\omega)$ its relative intensity. For $\lambda\omega \gg 1$, the ω-dependence of $P(\omega)$

can be approximated by

$$P(\omega) \sim \omega^{-2}. \tag{2.68}$$

2.2.3 Another method: Direct modeling of the fluctuations

Instead of the stochastic approach presented in the previous sections, the fluctuations can be modeled "directly" by performing the integration of the dust moment equations (2.5a,2.5b) on top of a concrete realisation of the stochastic process $(\Theta, \mathcal{K})_t$, i.e. a particular random temperature structure $T_{\rm gas}(t)$, which has been gained by subjecting the deterministic structure $\overline{T}(t)$ to random temperature deviations $T(t)$. A result of such a modeling process will be the time development of the dust moments $K_{\rm i}(t)$ on the particular random temperature structure $T_{\rm gas}(t)$, which has served as input. An advantage of this method is, that the resulting representants are actual realisations of the stochastic process, i.e. they look like the structures one would expect to observe, when observing a particular real object. This is certainly not the case for the expectation values $\mathrm{E}(K_\rho)(t)$ resulting from the solutions of the equation system (2.66); in particular the *mean* temperature structure $\overline{T}(t)$ is, for example, characterised by the complete absence of temperature fluctuations.

The main disadvantage of this direct hydrodynamical modeling is the fact, that different realisations of the same process $(\Theta, \mathcal{K})_t$ with the same parameters σ, λ on top of the same mean thermodynamical structure $\overline{T}(t)$ can look very different (see Fig. 4.9). It is thus not clear, which features of a particular solution have a general validity, and which features are just random properties of the particular representant. In order to gain information about the behaviour of the entire ensemble of possible realisations of the process, it is necessary to calculate a high number representants, hoping that their average converges to a particular solution.

Another problem of the direct hydrodynamical modeling of these processes is, that all fluctuations have to be resolved numerically in space and time. This can cause numerical problems as discussed in Sect. 3.3

2.3 Dust driven winds of AGB-stars

Long Periodic Variable stars (LPVs) on the *Asymptotic Giant Branch* (AGB) in the Hertzsprung Russel Diagram develop cool dust driven winds with high mass-loss rates. Typical parameters for these objects are given in Tab. 2.2.

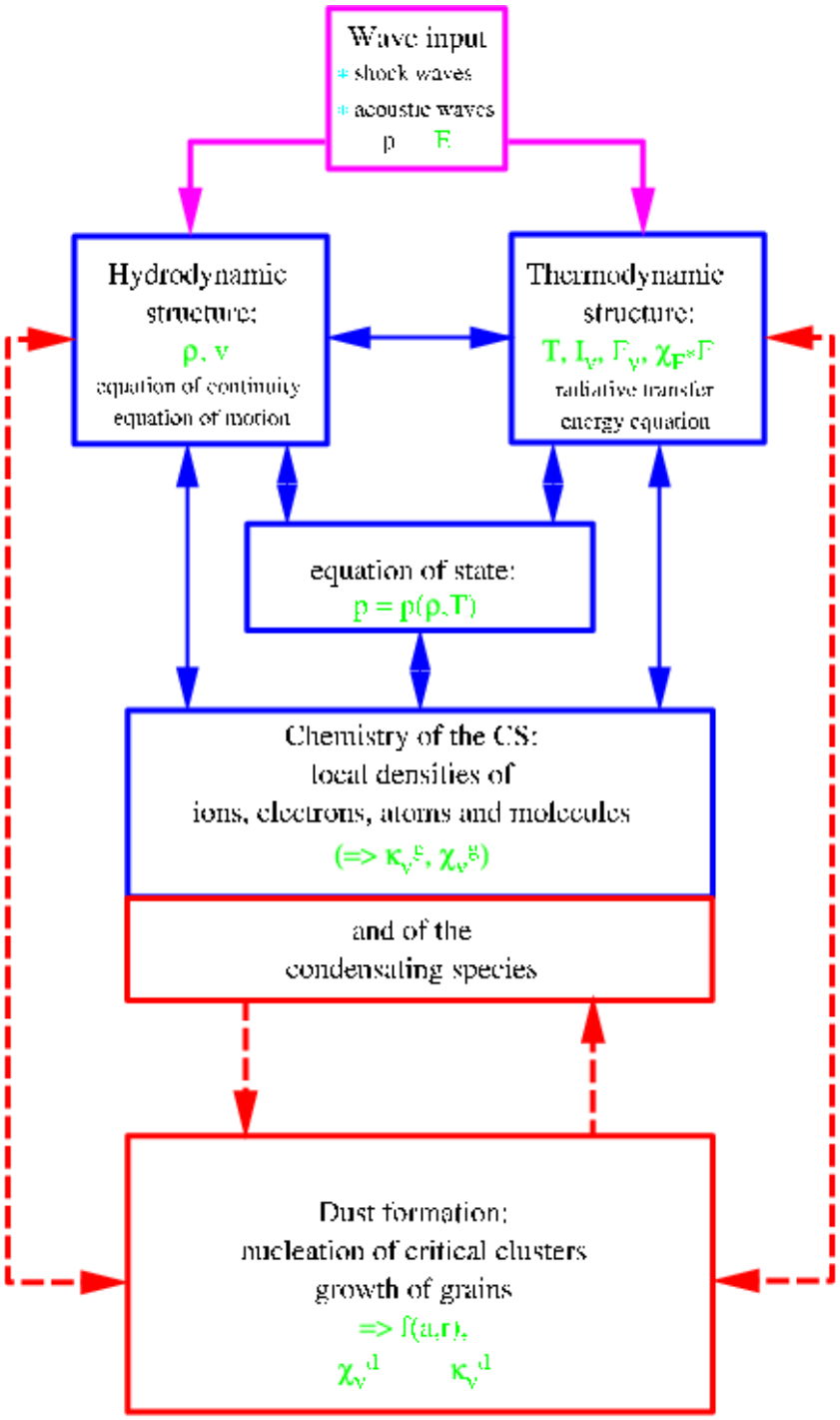

Figure 2.1: Plot of the coupling between the various physical complexes, that have to be described simultaneously, when modeling a dust-driven wind. Taken from Sedlmayr & Winters (1997)

stellar mass	$0.7 \ldots 2.0 M_\odot$
stellar luminosity	$10^3 \ldots 10^5 L_\odot$
stellar temperature	$2000 \ldots 3000$ K
mass loss rate	$10^{-7} \ldots 10^{-4} M_\odot$ yr^{-1}
final wind velocity	$10 \ldots 30$ km s^{-1}
pulsation period	$100 \ldots 1000$ days

Table 2.2: Typical values for stellar and wind parameters for dust forming late type stars. Taken from Sedlmayr & Winters (1997).

The general picture is that of an atmosphere, which is levitated by stellar pulsation waves, that have steepened up to shock waves while running through the density gradient in the outermost part of the atmosphere. In this levitated atmosphere the temperatures are low enough at simultaneously sufficiently high densities to allow for efficient dust formation. Since the newly formed dust has a considerably higher opacity than the circumstellar gas, it very efficiently absorbs the stellar radiation and is accelerated by the momentum transfer of the absorbed photons. The gas is dragged outwards by frictional coupling to the dust particles and a dust driven winds establishes.

The various physical domains relevant for the description of such a dust driven wind are shown in Fig. 2.1. They are strongly coupled via innumerable processes. The hydrodynamics, for example, couples to the dust formation via the opacity of the dust. The dust formation depends very sensibly on the local gas temperature and on the radiation field. The gas temperature again is determined by the interplay of energy input via the dissipation of hydrodynamic waves or the absorption of radiation and the cooling via hydrodynamic expansion and emission of radiation. Both the dust formation and the molecular opacity, which determines radiative heating and cooling, depend on the chemical composition of the gas, which again, even in the simplest imaginable case of *chemical equilibrium* (CE), is determined by temperature und density.

Thus, in order to achieve a selfconsistent physical description of a dust driven wind, we require the simultaneous solution of a coupled equation system describing hydrodynamics, thermodynamics, radiative transfer, chemistry and the dust condensation processes.

After pioneering studies from Wood (1979) and Bowen (1988), the first really selfconsistent dynamical 1D-models of dust-driven winds around pulsating carbon-rich AGB-stars, including a time dependent calculation of the dust component and a grey radiative transfer have been presented by Fleischer et al. (1992) (see also e.g. Fleischer 1994; Winters et al. 1997; Schirrmacher et al. 2003). Their results have been confirmed by Höfner et al. (1996)

(see also Dorfi & Höfner 1991; Höfner & Dorfi 1992; Feuchtinger et al. 1993) using a different numerical method. Jeong et al. (2003) have presented the first models for an oxygen-rich situation, where the condensation processes are more complicated, because it is neither clear which substances will start to form seed particles, nor which substances will later grow onto these seeds. Höfner et al. (2003) have investigated 1D-models with a frequency-dependent radiative transfer. Woitke (2006) has presented 2D-models of carbon-rich AGB-star-winds including time dependent hydrodynamics and dust formation coupled with a 2D Monte Carlo radiative transport, but without stellar pulsation. Wachter (2007) has investigated the interplay of mass-loss and stellar evolution for AGB-populations with subsolar metallicities.

In this work, the influence of temperature fluctuations on the dust formation will be investigated by implementing a microturbulent nucleation rate calculated as described in Sect. 6 into the CHILD-code, the 1D-hydro-code developed by Fleischer et al. (1992) in the version described in Schirrmacher et al. (2003). The physical approach followed by the CHILD-Code will be described in the following sections.

2.3.1 Hydrodynamics

The circumstellar shell is assumed to be spherically symmetric, which allows the reduction from a 3-dimensional to a 1-dimensional geometry. The 1D-geometry in turn, allows for a Lagrangean formulation of the hydrodynamic problem in a comoving frame, where R denotes the position of a fluid element, which is described by the Lagrangean variables r and t. r denotes the position of an element at the instant t_0: $r = R(t_0)$. The equation of motion then reads

$$\frac{\mathrm{D}v}{\mathrm{D}t} = -V_0 \left(\frac{R}{r}\right)^2 \frac{\partial p}{\partial r} + a_{\mathrm{tot}}, \tag{2.69}$$

where v is the velocity of the fluid element, V_0 denotes the specific volume of the fluid element at the moment t_0, p is the gas pressure, and a_{tot} stands for the sum of all accelerations, in our case the sum of radiative acceleration a_{rad} and gravitative deceleration a_{grav}

$$\begin{aligned} a_{\mathrm{tot}} &= a_{\mathrm{grav}} + a_{\mathrm{rad}} \text{ , with} \\ a_{\mathrm{grav}} &= -\frac{GM(R)}{R^2} \text{ , and} \\ a_{\mathrm{rad}} &= \frac{4\pi}{c_0}\frac{\chi_{\mathrm{H}}}{\rho} H(R) \,, \end{aligned} \tag{2.70}$$

where G denotes the gravitational constant, $M(R)$ the sum of the stellar mass M_* and the fraction of the envelope mass inside the position R, c_0 the

speed of light, $\chi_{\rm H}$ the flux weighted extinction coefficient, and $H(R)$ is the frequency integrated Eddington flux at the position R (see e.g. Sedlmayr & Winters 1997), which can be expressed by the flux weighted Eddington flux at the radius of the star R_*

$$H(R) = H_* \left(\frac{R_*}{R} \right)^2 , \tag{2.71}$$

which is a function of the stellar luminosity L_*:

$$H_* = \frac{1}{(4\pi)^2} \frac{L_*}{R_*^2}. \tag{2.72}$$

It is very useful to introduce the function

$$\alpha(R) = \frac{4\pi}{c_0 GM(R)} \frac{\chi_{\rm H}}{\rho} R^2 H(R) = \frac{1}{4\pi c_0 GM(R)} \frac{\chi_{\rm H}}{\rho} L_*, \tag{2.73}$$

which represents the radiative acceleration of a fluid element in units of the local gravitational deceleration. If $\alpha(R) > 1$ the fluid element is accelerated away from the star, otherwise it will fall back towards the star.

2.3.2 Thermodynamics

The integration of Eq. (2.69) requires a *thermal equation of state* which gives an expression for the pressure p in dependence of the thermal state variables. Depending on the gas model chosen for the description of the circumstellar gas, the thermal equation of state can have different forms. When using the model of an ideal gas, the pressure is given by

$$p(\mu, \rho, T_{\rm gas}) = \frac{\rho}{\mu m_{\rm u}} k_{\rm B} T_{\rm gas}, \tag{2.74}$$

where μ denotes the mean molecular weight of the gas particles in units of the atomic mass units $m_{\rm u}$. In this work, when using the approach of an ideal gas, the effect of a variable molecular mass is neglected, which leaves the gas pressure $p(T_{\rm gas}, \rho)$ as a function of temperature $T_{\rm gas}$ and density ρ only.

Another description used in parts of this work, is the gas model relying on Woitke (1997), who uses a multicomponent description of the gas, considering all molecular, atomic, and ionic species as well as the electrons separately. The thermal equation of state then reads

$$\begin{aligned} p\left(\rho, T_{\rm gas}, T_{\rm rad}, \left\langle \frac{{\rm d}v}{{\rm d}l} \right\rangle\right) &= p_{\rm atoms} + p_{\rm molecules} + p_{\rm ions} + p_{\rm electrons} \\ &= (n_{\rm atoms} + n_{\rm molecules} + n_{\rm ions} + n_{\rm electrons}) k_{\rm B} T_{\rm gas}, \end{aligned} \tag{2.75}$$

where the $n_{\mathrm{atoms,...}}$ stand for the particle densities of atoms, molecules, ions, and electrons, and the $p_{\mathrm{atoms,...}}$ for the corresponding partial pressures. These particle densities are obtained by solving a system of rate equations for the densities of all species involved and all relevant electronic excitation levels under the influence of a radiation field parametrised by the radiation temperature T_{rad} in statistical equilibrium as described in detail in Woitke (1997) (see also Schirrmacher et al. 2003, appendix). Since in this approach line emission is treated using the Sobolev theory, the parameter

$$\begin{aligned} \left\langle \frac{\mathrm{d}v}{\mathrm{d}l} \right\rangle &= \frac{1}{3}\left|\frac{\partial v}{\partial R}\right| + \frac{2}{3}\left(2x_0^{-1/2}-1\right)\left|\frac{v}{R}\right| \text{ with} \\ x_0 &= 1+\max\left\{0, -\frac{\partial v}{\partial R}/\frac{v}{R}\right\}, \end{aligned} \tag{2.76}$$

which describes the geometry of the circumstellar velocity field, is introduced as an additional state variable. Note that via the $\left\langle \frac{\mathrm{d}v}{\mathrm{d}l} \right\rangle$, the pressure does not only depend on the local values of T_{gas} and ρ but, in principle, also on the global velocity structure $v(R)$.

The gas temperature T_{gas} can be determined implicitly by the solution of the energy equation

$$\frac{\mathrm{d}e(T_{\mathrm{gas}},\ldots)}{\mathrm{d}t} = -p(T_{\mathrm{gas}},\ldots)\mathrm{d}V + \dot{Q}(T_{\mathrm{gas}},\ldots) \tag{2.77}$$

where e is the specific internal energy of the fluid element per unit mass and $\dot{Q}$ is the sum of all heating and cooling rates:

$$\dot{Q} = \dot{Q}_{\mathrm{rad}} + \dot{Q}_{\mathrm{vis}}. \tag{2.78}$$

$\dot{Q}_{\mathrm{rad}}$ denotes the *net* radiative rate of energy exchange between the gas and the radiation field, when $\dot{Q}_{\mathrm{rad}} > 0$ the gas is heated by the absorption of radiation, when $\dot{Q}_{\mathrm{rad}} < 0$ the gas is cooling by emission of radiation. $\dot{Q}_{\mathrm{vis}}$ is the viscous heating rate, which describes the heating of the gas by dissipation of shock waves. Throughout this work, $\dot{Q}_{\mathrm{vis}}$ is modeled via the tensor-viscosity by Tscharnuter & Winkler (1979). For the later discussion, it might be useful to introduce the *adiabatic* heating/cooling rate

$$\dot{Q}_{\mathrm{ad}} = -p\mathrm{d}V, \tag{2.79}$$

which stands for the rate of change of the internal energy of the gas via hydrodynamical compression or expansion.

The expressions for e and $\dot{Q}_{\mathrm{rad}}$ depend on the underlying model of the gas and of the energy exchange between gas and radiation field. In this work, two

different approaches are used. An overview over these two thermodynamical approaches is given in Table (2.3). The first one was presented by Fleischer et al. (1992) and describes the gas as an ideal atomic gas with the state variables $T_{\rm gas}$ and ρ. In this case, the thermal equation state is given by (2.74), while the *caloric equation of state*, which gives the dependence between the internal energy and the state variables reads

$$e\left(T_{\rm gas},\rho\right) = \frac{f}{2}\frac{1}{\mu m_{\rm u}} k_{\rm B} T_{\rm gas}, \tag{2.80}$$

f denotes the number of degrees of freedom; $f = 3$ for an atomic gas. Note that the internal energy of the ideal gas does not depend on the density. In combination with this simple gas model, the radiative cooling

$$\dot{Q}_{\rm rad} = 4\sigma_{\rm B}\kappa({T_{\rm rad}}^4 - {T_{\rm gas}}^4). \tag{2.81}$$

In the following, this cooling behaviour will be referred to as "T^4-cooling".

The second thermodynamical approach used in this work was presented in Woitke (1997) (see also Schirrmacher et al. 2003). Here the gas is understood as a mixture of various atomic, molecular and ionic species plus electrons, whose particle densities in all relevant excitation states are determined by solving a system of rate equations in statistical equilibrium with a radiation field, parametrised by its radiation temperature $T_{\rm rad}$. The internal energy is then given by

$$e = \frac{1}{\rho}\left(E_{\rm trans} + E_{\rm rot} + E_{\rm vib} + E_{\rm el} + E_{\rm ion} + E_{\rm diss}\right). \tag{2.82}$$

$E_{\rm trans}$ is the translational energy of all gas particles, $E_{\rm rot}$ and $E_{\rm vib}$ rotational and vibrational energy of the molecules, $E_{\rm el}$ is the excitation energy of the electrons, $E_{\rm ion}$ the ionisation energy of the ions and $E_{\rm diss}$ the dissociation energies of the molecules. The net radiative heating/cooling rate $\dot{Q}_{\rm rad}$ is then obtained by summing up all microscopic rates, which involve an interaction between the gas and the radiation field, i.e. those rates, where the corresponding microscopic process includes the emission or the absorption of a photon.

2.3.3 Radiative Transfer

Within the framework of a circumstellar envelope, the treatment of the radiative transfer problem is essential for the determination of the gas temperature. Since – irrespective of which of the two thermodynamic concepts

Description:	
ideal gas, LTE, T^4-cooling	multicomponent gas, non-LTE, detailed cooling function emerging from SE calculation
State variables:	
$T_{\rm gas}$, ρ	$T_{\rm gas}$, $T_{\rm rad}$, ρ, $\left\langle \frac{{\rm d}v}{{\rm d}l} \right\rangle$
Equations of state:	
thermal: $p = \rho k_{\rm B} T_{\rm gas} (\mu m_{\rm u})^{-1}$ caloric: $e = f k_{\rm B} T_{\rm gas} (2\mu m_{\rm u})^{-1}$	Eq. (2.75, thermal) and Eq. (2.82, caloric) calculated in SE
Radiative Cooling:	
analytical T^4-cooling (Eq. 2.81)	tabulated cooling rates $\dot{Q}_{\rm rad}$ resulting from summing up all radiative rates from the SE-Calculation.
Molecular weight:	
constant mean molecular weight $\mu = 1.26\, m_{\rm u}$ assuming all hydrogen is in the atomic state	the different species have their correct molecular weight, the mean molecular weight can be calculated by $\mu = \rho k_{\rm B} T_{\rm gas} / (m_{\rm u} p)$.
Literature:	
Fleischer et al. (1992) Fleischer (1994)	Woitke (1997) Schirrmacher et al. (2003)

Table 2.3: Comparison between the two thermodynamic models used for the circumstellar gas.

presented in the previous section is used – the determination of the gas temperature $T_{\rm gas}$ requires the knowledge of a radiation temperature $T_{\rm rad}$ only, it is sufficient – from a mathematical point of view – to treat the radiative transfer problem in grey approximation. In practice a two stream approximation developed by Lucy (1971, 1976) and Unno & Kondo (1976) in a version improved by Hashimoto (1995) (for details see Winters et al. 1997) has been used, which leads to the following equation for the determination of the radiation temperature $T_{\rm rad}$:

$$ {T_{\rm rad}}^4 = \frac{R^2 F(R_{\rm in})}{2\sigma_{\rm B}} \cdot \left[\frac{1}{R_{\rm out}(1+\mu_{R_{\rm out}})} + \frac{\mu_{R_{\rm out}}}{{R_{\rm out}}^2} - \right. $$
$$ \left. - \frac{\mu_R}{R^2} + \frac{3}{2} \int_R^{R_{\rm out}} \left(\chi(R') + \frac{2\mu_{R'}}{R'} \right) \frac{{\rm d}R'}{R'^2} \right], \quad (2.83) $$

where μ_R, the cosine of the separation angle of the two radiation streams $I^+(R)$, and $I^-(R)$, is itself determined by the solution of the differential

equation

$$\frac{\mathrm{d}\mu_R^3}{\mathrm{d}R} = \frac{\chi(R)}{4}\left(1 - 5\mu - R^2\right) + \frac{3\mu_R}{R}\left(1 - \mu_R^2\right). \tag{2.84}$$

2.3.4 Dust and chemistry

The dust condensation in the dynamical models is calculated using the dust moment method developed by Gail & Sedlmayr (1984), which has already been discussed in detail in Sect. 2.1. The equation system (2.5) is solved simultaneously with the hydro- and thermodynamical equations and the equation for the radiation temperature, using the gas temperature T_{gas} and density ρ as input for the source terms J and τ^{-1} in Eq. (2.5). The dust temperature T_{dust} for the determination of the supersaturation ratio S is set to T_{rad} for the determination of the growth rate τ^{-1}, while it is set to T_{gas} for the determination of the nucleation rate J. The idea behind this choice, is that the growth rate τ^{-1} is calculated for macroscopic particles, which – due to their higher absorption efficiency – couple stronger to the stellar radiation field, than to the comparatively thin circumstellar gas. In contrast the *critical* clusters, which are relevant for the calculation of the nucleation rate, are usually very small and therefore assumed to be in equilibrium with the gas phase, from which they emerge.

The chemistry is assumed to be in chemical equilibrium throughout this entire work, which means that the particle densities of the growth species can be calculated by the law of mass action.

The dust opacity

Via Eq. (2.73) the acceleration of the wind is coupled to the flux weighted extinction coefficient χ_{H}, which can be calculated by the gas and dust opacity

$$\chi_{\mathrm{H}} \;=\; (\kappa_{\mathrm{gas}} + \kappa_{\mathrm{dust}})\,\rho \tag{2.85}$$

where κ_{gas} and κ_{dust} are frequency averaged mean opacities. The following approximations are made: The gas opacity is assumed to have the constant value of $\kappa_{\mathrm{gas}} = 2 \times 10^{-4}$ cm^{2}g^{-1} based on the Rosseland-mean opacities from Alexander et al. (1983). The dust opacity is calculated according to Gail & Sedlmayr (1987b) in the small particle limit of Mie-Theory

$$\kappa_{\mathrm{dust}} = \frac{3}{4} V_0 K_3 Q'(T_{\mathrm{dust}}) \tag{2.86}$$

where the extinction efficiency $Q'(T_{\mathrm{dust}})$ of the dust is approximated by a parameter function

$$Q'(T_{\mathrm{dust}}) = \eta_{\mathrm{opt}} T_{\mathrm{dust}}. \tag{2.87}$$

Since the dust particles are energetically coupled to the radiation field, rather than to the surrounding gas, it is assumed that the dust temperature corresponds to the radiation temperature, i.e. $T_{\rm dust} = T_{\rm rad}$.

2.3.5 Discussion of the approximations

1. **Spherical symmetry:** The assumption of spherical symmetry reduces the geometry of the objects from a 3D- to a 1D-problem. Until a few years ago, this was absolutely necessary to reduce the numerical effort to solve the non-linear coupled equation system, which describes the dust-driven winds. By assuming spherical symmetry, one renounces to the investigation of effects of stellar rotation or magnetic fields, as well as to the individual hydrodynamical resolution of turbulence or convection processes. Whereas rotation and magnetic fields do not seem of particular importance for the understanding of dust-driven AGB-winds, turbulent velocity fields will certainly occur in the convective envelope inside the star at the bottom of the stellar atmospheres, as well as during the dissipation of the stellar pulsation waves in the circumstellar envelope. At the moment, the computing capacities are advancing into regions, where codes that solve the complex coupled equation system for the wind in the frame of a multidimensional hydrodynamical description are beginning to be developed (Woitke 2006, has presented 2D-models of dust driven AGB-winds, which are at the moment still neglecting the pulsation of the star.) However, even these calculations have to tackle the problem, that they cannot resolve the dissipation of the turbulence elements to the sub-grid scales. Since the aim of this work is to investigate the influences of temperature fluctuations on the dust formation, and there is no reason to believe that a multidimensional hydrodynamical frame for these investigations will make a particular difference, the use of a well understood 1D-model seems to be well justified. For the determination of suitable values of the fluctuation parameters σ and λ, models using multidimensional hydrodynamics might, however, be of some use.

2. **Carbon Dust:** Two main classes of AGB stars are observed, carbon rich and oxygen rich stars. It is by now widely accepted, that these two classes represent subsequent evolutionary stages of low and intermediate mass AGB-stars. During a thermal pulse, the convective envelope of these stars reaches the He-burning layer, where carbon is produced, and mixes the new carbon up into the stellar envelope and atmosphere. If the carbon abundance in the atmosphere exceeds the

oxygen abundance, the spectral class from the star switches from O to C.

The ratio $\epsilon_C/\epsilon_O =: [C/O]$ of carbon and oxygen abundance is a key indicator for the nature of the chemistry in the stellar atmosphere and the circumstellar envelope. Due to the high binding energy of the CO-molecule (about 11 eV), nearly all atoms of the less abundant species are blocked in CO-molecules with a striking impact on the chemistry of the remaining species. In an oxygen-rich situation, the typical high temperature condensates are silicates Si_xO_y and metal oxides, like Ti_xO_y, Mg_xO_y, Al_xO_y. In this case, it is not really clear which species nucleate at first and which species will later grow onto the seed particles. A simple grain size distribution function of the form $f(N)$ as presented in Sect. 2.1 can not be used to describe the emerging heterogeneous dust grains. (Jeong et al. 2003, have presented model calculations for such oxygen rich AGB-winds.) The carbon rich situation is simpler, when assuming that graphite is the main constituent of the dust grains. This might not be the whole picture, because probably some nucleation will also take via polyaromatic hydrocarbons (PAH's), but again, the detailed investigation of the nucleation paths is not the aim of this work. Since there seems no reason to believe, that temperature fluctuations will a priori have a different influence in the oxygen-rich case than in the carbon rich situation, in this work, for the sake of simplicity, the carbon rich formulation is used.

3. **Gas model (LTE)**: For the models calculated using the T^4-cooling acc. to Eq. (2.81), the gas is modeled as a one-atomic ideal gas with a constant molecular weight. This assumption neglects the effects of ionisation and molecule formation/dissociation. The neglection of ionisation is widely uncritical, since the radiation fields from AGB-stars have no significant short wavelength ionising component. In the context of the presented hydrodynamical models, ionisation might occur in the innermost parts, below the surface of the star, which is only included for reasons of numerical stability, and not to be the subject of the latter physical interpretation. Another case, where ionisation might occur, is in the strongest shock waves, that are developed by some models of particularly compact stars (low luminosity, high mass, strong pulsation). However, the modeling of the shock waves using shock-broadening via artificial viscosity follows a philosophy, of giving a good model of the *surroundings* of the shock, but not for the details of the thermodynamical structure of the shock itself.

The neglection of molecule formation and dissociation is more critical, because in particular the formation of molecular hydrogen from hydrogen atoms does have a significant impact on the mean molecular weight ($\mu \approx 2.3$ for H_2, and $\mu \approx 1.3$ for H) and therewith on the pressure (see Eq. 2.74), while the associated dissociation energy constitutes a significant energy reservoir, which will considerably delay radiative cooling. A proper modeling of the H_2-formation in chemical equilibrium is certainly possible, but since the implementation into the CHILD-Code is not as trivial as it might look, it has never been done, after the version including the SE-state equations and -cooling functions, which includes these effects implicitly, was running (Schirrmacher et al. 2003).

The assumption of T^4-cooling is very close to the isothermal limit case for the fastest thinkable radiative cooling (or heating) of the gas, where the gas temperature is assumed to relax immediately (i.e. on time scales shorter than the numerical time step) to the radiation temperature $T_{\rm rad}$. The general structure of the stellar wind looks quite alike in the isothermal limit case except for some extra heating in the shock front, and also very much like the models with SE-state-equations and -cooling functions. Nevertheless, these models have been included in this work, because it has turned out, that the dust condensation depends sensibly on possible temperature differences between the gas and the dust, which is assumed to couple to the radiation field via $T_{\rm dust} = T_{\rm rad}$, and it therefore seemed interesting to investigate models with a different temperature difference between $T_{\rm dust}$ and $T_{\rm gas}$.

4. **Gas model (statistical equilibrium)**: The assumptions made during the calculation of the thermal (2.75) and the caloric (2.82) equation of state, and the non-LTE cooling functions $\dot{Q}_{\rm rad}$ are discussed in detail in Woitke (1997). Here I only want to discuss those assumptions that are most important within the framework of the hydrodynamical models of this work.

   First thing to mention is, that the radiation field and the hydrodynamical structure enter the description in the form of only two parameters: $T_{\rm rad}$ and $\left\langle \frac{{\rm d}v}{{\rm d}l} \right\rangle$. This is obvious a quite rough approximation for these two nonlocal phenomena, but for the applicability of the gas model in a selfconsistent numerical calculation, this reduction was imperative.

   The description of the velocity field by the parameter $\left\langle \frac{{\rm d}v}{{\rm d}l} \right\rangle$ implies the assumption, of a velocity field which is monotonously increasing with increasing distance from the star. This is important to determine the resonance region around a line-emitting gas element, where the

emitted line photon can still be absorbed in the same line. The effect of several shells having the same velocity at various distances from the star is neglected, i.e. it is assumed, that the line radiation emitted by the innermost shell is not absorbed by an outer shell having the same velocity, as well as the heating of the outer shell by a possible high line emission from an inner shell is not taken into account. Nevertheless, in contrast to the usual complete ignorance of line cooling effects, this one-parametric description is certainly a step forward.

The reduction of the entire frequency dependent radiation field to a radiation temperature $T_{\rm rad}$ only is certainly a quite rough approximation as well. This corresponds to the assumption that the spectral energy distribution J_ν of the radiation field corresponds to that of a black body with the temperature $B_\nu(T_{\rm rad})$. This spectral energy distribution is needed to calculate the excitation levels of all species in the gas, where the effects of various lines cooling at particular wavelengths can certainly be very important. There is no principle problem, of doing the SE-calculation with an arbitrary radiation field. However, the need of including the resulting state- and cooling functions into an overall model, which only delivers a radiation temperature and no spectral information, requires an accordingly simple approximation of the spectral distribution of the radiation field.

Another assumption concerning the interaction between gas and radiation field is, that every feedback from the gas to the radiation field via particular emission processes is neglected. The SE-calculation delivers the net energy exchange rate $\dot{Q}_{\rm rad}$ between the gas and the radiation field, which is then used in the energy equation, but no corresponding term describing a possible feedback to the radiation field is included in the treatment of the radiative transfer. This might be no crucial assumption within the frame of a grey radiative transport, where any emission from a particular gas element will be a rather subtle[8] modulation of the overall radiation field. When implementing a frequency dependent radiative transfer into the overall system, where the line emission from a particular gas element can be quite important for the corresponding line intensity, this point will need a close reinspection.

[8]Note, that the neglection of feedback of the exact energy exchange rates to the radiation field, does not mean, that there is no emission from the gas taken into account when solving the radiative transfer. It means only that the quite detailed information about the exact energy exchange processes, which is obtained during the SE-calculation, is discarded after calculating the state functions, and the gas emission for the radiative transfer is later determined using a simpler model.

5. **Stationary, grey radiative transfer:** In this context, "stationarity" means, that the travelling time of the photons of one part of the circumstellar envelope to any other is neglected. When being picky about it, this assumption is not strictly fulfilled, because the light travelling time in a typical circumstellar envelope of an AGB star can be in the order of $10^2 \ldots 10^4$ s, which is about the same as typical time steps in the numerical calculation. However, in the resulting models, no effects are observed, where a sudden change of the radiation field at a certain distance from the star, has a striking immediate effect on the situation at a completely different position, which then suddenly vanishes after a time short compared to the corresponding light travelling time. The assumption of stationarity in the radiative transfer calculation does therefore not seem a crucial one.

   The restriction to a grey radiative transport, i.e. reduction of the frequency dependent radiative transfer equation for I_ν to the frequency integrated form for $I = \int_0^\infty I_\nu \mathrm{d}\nu$, using frequency integrated values for the extinction coefficients χ_ν, certainly cuts away a good deal of physical effects, like radiative heating/cooling/driving of particular lines, possible maser effects, frequency shifts in the stellar spectrum due to the opacity of the dust in the visible light, and its high emission in the IR-spectral region.

   Historically – like the restriction to 1D – this restriction was necessary to reduce the computation effort for solving the nonlinearly coupled selfconsistent equation system of the time dependent wind. By now, like for the multidimensional models, computer power is about to reach the level, where a frequency dependent treatment of the radiative transfer is possible (see e.g. Höfner et al. 2003; Gautschy-Loidl et al. 2004). Unlike in the situation for the multidimensional hydrodynamics, a frequency dependent treatment of the radiation field might very well have significant effects on the influence of temperature fluctuations on the dust formation, because it will be one of the results of this work, that the temperature of the dust, in particular of the critical clusters, are very important for the details of the condensation process. The temperature of a dust grain depends very sensibly on the interplay of its individual frequency dependent extinction coefficient and the details of the radiation field, that it is coupled to. However, the solution of an equation system, describing such a detailed coupling between a radiation field and the local gas/dust mixture in a time dependent hydrodynamical situation, which would also have to include a detailed frequency dependent calculation of atomic, molecular and size

dependent dust opacities, combined with a dust description far more detailed than the moment method presented in Sect. 2.1, is still beyond our numerical capacities and far beyond the scope of this work.

6. **Chemical equilibrium:** The exact knowledge of the molecular abundances is important i) for the calculation of the opacity that enters the radiative transfer, ii) for the calculation of the nucleation and growth rates of the dust grains, and iii) for the calculation of the state and cooling functions. Since we are applying a grey radiative transfer calculation which uses a constant gas opacity, the first requirement can be dropped. For the determination of the state and cooling functions we either use the ideal monoatomic gas-model, that neglects all chemical processes by assuming a constant molecular weight, or tabulated functions gained by the solution of a system of rate equations in statistical equilibrium. In the latter case, a detailed chemistry was calculated during the calculation of the tables for p, e and $\dot{Q}_{\rm rad}$, and then discarded. Therefore, the only remaining need for a chemical calculation in the frame of the time-dependent hydrodynamical models, is the need for the particle densities of the growth species for the dust calculations. Thus, for the sake of simplicity, only the abundances of H, H_2, C, C_2, C_2H and C_2H_2 are calculated under the assumption of i) chemical equilibrium and ii) that all oxygen is blocked in CO.

Chapter 3

Numerical Realisation

3.1 Evaluation of the deterministic dust equations

The equation system (2.5) needs to be evaluated i) for the deterministic calculations required for the boundary paths of the Fokker-Planck system (2.66), ii) for the calculation of the last two terms on the r.h.s. of Eq. (2.66), that contain the transition probabilities of the dust component $\mathcal{K}_t$ of the stochastical process $(\Theta, \mathcal{K}_t)$, and finally iii) for the calculation of the Monte-Carlo models presented in Sect. 4.3.

For the case of dust nucleation and growth, the numerical evaluation of Eq. (2.5) is straight forward. The nucleation rate J and the growth rate τ^{-1} are calculated as described in Sect. 2.1. However, the calculation of J requires the parameter S_{crit}, which corresponds to the minimum supersaturation ratio required for dust nucleation from the gas phase.

The treatment of the dust evaporation and destruction as described in Sect. (2.1.6) is more challenging, because it requires the storage of the dust moment history in the form $K_{\mathrm{i}}(a_{\mathrm{max}})$. In case of evaporation, the new value of $a_{\mathrm{max,new}}$ ($< a_{\mathrm{max,old}}$) is calculated, and the values of the K_{i} are then restored to the value they had, when the maximum particle radius a_{max} last had the value $a_{\mathrm{max,new}}$. Since it is impossible to store $K_{\mathrm{i}}(a_{\mathrm{max}})$ for every discrete value of a, the a axis is binned and the K_{i} stored into arrays of a-bins. When the maximum particle radius a_{max} exceeds the edge of these arrays $a_{\mathrm{storage,max}}$, the value $a_{\mathrm{storage,max}}$ is doubled and the storage arrays $K_{\mathrm{i}}(a_{\mathrm{max}})$ need to be remapped onto the newly dimensioned arrays. This procedure is repeated, if necessary, until the maximum particle radius $a_{\mathrm{max}}(t)$ "fits" again into the array. In the reverse case, when evaporation has gone so far, that the remaining a_{max} lies rather close to the lower edge of the a-axis, *no* remapping

Symbol	Value	Description
a_ℓ	10	minimum grain size in units of the dimensionless particle radius a, for which a cluster is regarded as a macroscopic grain. This parameter corresponds to the minimum grain size N_ℓ for which the grain size distribution function is defined.
$a_{\mathrm{storage,max}}$	> 100	a-value at the upper boundary of the storage arrays $K_{\mathrm{i}}(a_{\mathrm{max}})$. When the size of the biggest particle $a_{\mathrm{max}}(t)$ exceeds $a_{\mathrm{storage,max}}$, the value of $a_{\mathrm{storage,max}}$ is doubled and the functions $K_{\mathrm{i}}(a_{\mathrm{max}})$ need to be remapped
N_a	100	Array length for the storage of the dust moment $K_{\mathrm{i}}(a_{\mathrm{max}})$.
S_{crit}	3	In the deterministic case the nucleation rate J is only calculated, when the supersaturation ratio S exceeds the value of S_{crit}

Table 3.1: Numerical parameters for the deterministic dust calculation.

is implemented, because once the information is lost at the compression of the $K_{\mathrm{i}}(a_{\mathrm{max}})$ during the growth, it cannot be restored, by filling a resized array with interpolated values. If however, the evaporation process in a volume element is complete $a_{\mathrm{storage,max}}$ is restored to its initial value.

An overview over the numerical parameters required for the evaluation of Eq. (2.5) is given in Table 3.1.

3.2 Evaluation of the Fokker-Planck-System

We need to evaluate the system of coupled Fokker-Planck-Equations given by (Eq. 2.66)

$$\frac{\partial}{\partial t} q_\rho = -\frac{1}{\lambda} T \frac{\partial}{\partial T} q_\rho + \frac{\sigma^2}{\lambda} \frac{\partial^2}{\partial T^2} q_\rho + A_{\rho\nu} q_\nu + b_\rho, \quad \rho = 0, 1, 2, 3. \tag{3.1}$$

Formally, this equation system is identical[1] to Eq. (4.13) from Dirks (2000). Therefore, in this work, the same numerical scheme is adapted, which will be sketched in the rest of this section.

[1]Note, however, that Dirks uses a different time variable and functions $\tilde{q_\rho}$, that take into account the spherical structure of his wind.

3.2.1 Discretization

Eq. 2.66 is evaluated on a (t,T)-grid, where t stands for the time in seconds and T for the deviation of the gas temperature from a given mean value $\overline{T}(t)$ in Kelvin, i.e. the actual gas temperature at a given grid point is

$$\begin{aligned} T_{\text{gas}}(t,T) &= \overline{T}(t) + T, \\ T_{\text{gas}}(t,0) &= \overline{T}(t). \end{aligned} \tag{3.2}$$

The time derivative is approximated by a first order forward difference, while the T-derivatives are approximated by second order Taylor approximations (see Dirks 2000). The temperature spacing doesn't necessary need to be equidistant, however throughout this work an equidistant spacing for the temperature deviation is used.

3.2.2 Crank-Nicolson Scheme

The time integration of the Fokker-Planck system (2.66) is then performed using a Crank-Nicolson-Scheme, which is a special case of a *weighted average method,* (see Morton & Mayers 1994, Section 2.10). The idea of the weighted average methods is that they allow a continuous "switching" between explicit and implicit integration via a parameter θ which specifies the degree of "explicitness":

$$\begin{aligned} \frac{\partial}{\partial t} q_\rho(k,j) &\approx \theta f_k + (1-\theta) f_{k+1}, \\ f_k &= -\frac{1}{\lambda} T(k,j) \frac{\partial}{\partial T} q_\rho(k,j) + \frac{\sigma^2}{\lambda} \frac{\partial^2}{\partial T^2} q_\rho(k,j) + A_{\rho\nu}(k,j) q_\nu(k,j) + b_\rho(k,j), \end{aligned} \tag{3.3}$$

where k is the discretized time variable and j the discretized variable for the temperature deviation T. For $\theta = 1$, Eq. (3.3) yields the expression for an explicit time step, whereas $\theta = 0$ corresponds to a fully implicit time step. If θ is chosen as 0.5 the scheme is called a Crank-Nicolson-Scheme.

When inserting the discretization into the Crank-Nicolson-Scheme, one obtains a set of linearly coupled algebraic equations, which can be represented by a tridiagonal matrix, and solved by standard numerical methods. In this work, *Crout's algorithm* has been used (see Burden & Faires 2001, p.408).

3.2.3 Initial and boundary values, and the deterministic mean path

The temporal forward integration of the Fokker-Planck system (2.66) on a (t,T) plane-requires

1. initial values $q_\rho(t, T)$,

2. boundary values $q_\rho(t, -\Delta T_{\max})$, and $q_\rho(t, +\Delta T_{\max})$, and

3. the deterministic thermodynamical mean path $\overline{T}(t)$, $\overline{\rho}(t)$.

In principle, any arbitrary combination of $\overline{T}(t)$, and $\overline{\rho}(t)$ can be chosen as deterministic path. In this work, a simple model of a stationary AGB-wind was used (see Table 4.1). In this case, it is sufficient to start the integration close enough to the star, to ensure a dust free initial situation and the initial condition becomes trivial:

$$q_\rho(t, T) := 0. \tag{3.4}$$

A physically reasonable choice of the boundary conditions is more difficult, but test runs have revealed, that if the $\Delta T_{\max}$ is chosen large enough, the choice of the boundary values is uncritical for the solution $q_\rho(t, T)$ in the T-domain, which will later contribute to the calculation of the expectation values. For the calculations presented in Sect. 4, the boundary paths have been set to the corresponding deterministic paths:

$$q_\rho(t, \Delta T_{\max}) = K_\rho(t, T_{\text{gas}} + \Delta T_{\max}) = K_\rho(t, T_{\max}) \tag{3.5}$$

$$q_\rho(t, -\Delta T_{\max}) = K_\rho(t, T_{\text{gas}} - \Delta T_{\max}) = K_\rho(t, T_{\min}), \tag{3.6}$$

where the $K_\rho(t, \pm\Delta T_{\max})$ have been calculated along a wind structure with a constant temperature offset of $\pm\Delta T_{\max}$. The cut-off of the temperature deviation at $\pm\Delta T_{\max}$ is necessary, because in integration from $-\infty$ to $+\infty$ is numerically impossible and physically senseless. The value of $\Delta T_{\max}$ is parametrised introducing the numerical parameter γ

$$\Delta T_{\max} = \gamma\sigma. \tag{3.7}$$

Typical values for the parameter γ are $5, \ldots, 10$; usually a value of $\gamma = 8$ has been adopted. If γ is chosen too small, the influence of the boundaries can become overwhelming, which results in an apparent solution q_ρ, which actually turns out to be only the arithmetic mean of the boundary-paths. If γ is chosen to big, it is possible – in particular for large values of σ, that large parts of the (t,T)-plane lie in thermodynamical regions below $T_{\text{gas}} = 500K$, where the chemical model for the dust-growing species begins to lose sense. In extreme situations, an inconsiderate choice of γ can lead to the (numerical) appearance of negative gas temperatures, which obviously has to be strictly avoided.

3.2.4 Numerical resolution

After having provided the fluctuation parameters σ and λ, the deterministic mean structure, and the parameters needed for the dust calculation (see Sect. 3.1), only the grid spacings of the (t, T) grids remain to be provided:

- **Time steps (t-grid):** in order to achieve a reasonable numerical resolution, the time step Δt must be smaller than the correlation time λ. Furthermore, it is desirable that the relative changes of the q_ρ do not become to large. Typical values for Δt were $10^2 \ldots 10^3$ s in order to get a proper spatial resolution of the stationary wind, but during the actual condensation phase time steps were allowed to go down as far as 10^{-2} s.
- **T-Grid:** The number of grid points along the T-axis was varied from 100 to 200. When this number is too small negative q_ρ might result during the solution of the tridiagonal system, when chosen too large, the influence of the boundaries was sometimes growing undesirably high.

3.3 Direct modeling of the fluctuations

As described in Sect. 2.2.3, it is possible to model the fluctuations directly. Instead of the expectation values for the K_i, one obtains a particular thermodynamical structure representing a possible realisation of the stochastic process $(\Theta, \mathcal{K})_t$, (see e.g. Fig. 4.9).

Numerically, these structures are obtained, by constructing a representant of the stochastical process Θ_t as suggested by Eq. (2.44). Each time step, a random temperature fluctuation corresponding to the second term on the r.h.s. of Eq. (2.44) is added to the mean temperature $\overline{T}$. Due to their randomness, in this work, theses models will be referred to as *Monte Carlo*-models. The correlation is assured by a relaxation term, similar to the first term on the r.h.s. of Eq. (2.44), i.e. each time step, the difference between the last T_gas and $\overline{T}$ is reduced by the factor $\exp(-\Delta t/\lambda)$ (see Eq. 2.47), and then a new gauss weighted random term acc. to Eq. (2.46) is added.

The density ρ is then coupled adiabatically to the temperature deviation T according to

$$\rho(T) = \left(\frac{\overline{T} + T}{\overline{T}}\right)^{\frac{1}{\gamma_\mathrm{ad}-1}}, \text{with}\, \gamma_\mathrm{ad} = \frac{f+2}{2}, \tag{3.8}$$

with γ_ad denoting the adiabatic exponent, and f the number of degrees of freedom of the gas. In this work, f was chosen as $f = 3$, corresponding to a

one atomic ideal gas. However, the influence of the density on dust nucleation and growth is linear, i.e. when normalised to the number density of hydrogen cores $n_{\hat{\mathrm{H}}}$, the nucleation rate J is nearly independent on the density (see e.g. Fig. 6.1, top left).

Problems occurring during the direct modeling

Due to the explicit usage of random numbers during the direct modeling of the fluctuations, in principle, arbitrarily high fluctuations are possible, even though improbable. Whereas these "exotic" representants are included implicitly in the ensemble of stochastic pathways, whose behaviour is described by the equation system (2.66), they can cause trouble when they randomly turn up during the construction of a particular representant of that ensemble $T_{\mathrm{gas}}(t)$. Typical problematic situations are, e.g. , strong negative fluctuations that might lead to negative temperatures. These are mathematically that improbable, that their effect will hardly influence the solutions of the Fokker-Planck system (2.66), however, when randomly generating the representants these improbable solutions can show up. Another example for a numerically problematic situation is, when a particular random fluctuation becomes so big, that its application would require a shorter time step.

In this work, the Monte-Carlo calculations are only presented to give another point of view with respect to the interpretation of the nature of the stochastic process $(\Theta, \mathcal{K})_t$. Models that were numerically problematic were just not chosen for representation. If, however, it is desired to use these Monte-Carlo models for the calculation of expectation values, these problems would need to be tackled, because the biased neglection of the problematic models could have a significant influence on the resulting expectation values, because they are calculated by averaging over a large number of models.

3.4 Selfconsistent, dynamical wind models

For the numerical evaluation of the equation system described in Sect. 2.3, the CHILD-Code is used, which was originally developed by Fleischer et al. (1992), (see also Fleischer 1994; Winters et al. 1997). The CHILD-code is a one-dimensional hydro-code, which solves the hydrodynamical equations (2.3.1) together with the equations for thermodynamics (2.3.2), radiative transfer (2.3.3), a CE-chemistry and the time dependent dust moment equations (2.3.4, and 2.1) by an explicit forward integration in a comoving Lagrangean frame with an adaptive grid. The stellar pulsation is modelled by a sinusoidal variation of the velocity of the inner boundary.

Two families of models were calculated (see Sect. 2.3.2 and Table 2.3). The models using the ideal gas model and analytical T^4-cooling rates were calculated using the original CHILD-code in the version of Winters et al. (1997), whereas the models with non-LTE cooling functions and a more sophisticated modeling of the gas according to Woitke (1997) were calculated using the CHILD-code in the version described by Schirrmacher et al. (2003).

3.4.1 Model parameters

A particular wind model is described by the following parameters (see also Table 3.2): stellar mass $M_\star$, stellar luminosity $L_\star$, photospheric temperature $T_\star$, pulsational period P, and carbon-to-oxygen ratio $[C/O]$. Furthermore, two parameters for the description of the stellar pulsation are needed: the initial velocity amplitude $v_{\rm amp,0}$ and the final velocity amplitude $v_{\rm amp}$ of the piston at the inner boundary. By the implementation of the microturbulent nucleation rate (see Sect. 6), an additional parameter describing the temperature fluctuation, the rms temperature deviation σ, is added.

In addition to the above described primary model parameters, a set of numerical parameters is needed. An overview and descriptions are given in Table 3.2.

3.4.2 The start model

The dynamical calculations are started on a dust-free hydrostatic start model, which was constructed using the same spatial discretization. When switching on the piston, the first waves steepen up dramatically and reach unphysically high velocities. Therefore the piston is not started with its final velocity $v_{\rm amp}$, but with a lower value $v_{\rm amp,0}$ and increased to its final value within the time $t_{\rm pis}$. Furthermore, $R_{\rm out}$ is increased slowly from $2R_\star$ to $25R_\star$, and, in regular intervals $t_{\rm rezone}$, any grid points above the current $R_{\rm out}$ are discarded and new ones inserted in the inner integration domain. This way, the first unrealistic shock front is quickly cut off, which saves a good deal of calculation time. However, due to these starting procedures, it is necessary to wait until the model has relaxed towards a periodical or pseudo-stationary state, before the result can be evaluated. This will take at least until the shock front, that was induced by the last pulsation with a reduced amplitude has reached $R_{\rm out}$. For $R_{\rm out} = 25R_\star$ and $t_{\rm pis} = 15P$, this will surely be the case after $40P$. The results presented in Chapter. 7 were evaluated not earlier than after $90P$, so that any perturbations by the starting procedure have had enough time to leave the integration domain.

Model Parameters		
Symbol	Values	Description
$[C/O]$	1.8	carbon to oxygen ratio
$L_\star$	$6000 \ldots 10000 L_\odot$	stellar luminosity
$M_\star$	$0.8 \ldots 1.0 M_\odot$	stellar mass
P	650 days	pulsational period
$T_\star$	$2400 \ldots 3000$ K	photospheric temperature
$v_{\rm amp}$	2×10^5 cm/s	final piston amplitude
Other parameters and material constants		
Symbol	Value	Description
$N_{\rm start}$	512	initial value of grid points
$N_{\rm final}$	$1024 \ldots 1924$	final number of grid points
$Q'(T_{\rm dust})$	$(4.4 \ldots 5.9) \times T_{\rm dust}[K]$	extinction efficiency of the dust(see Gail & Sedlmayr 1985; Helling 1999)
$R_{\rm in}$	$0.91 R_\star$	position of the inner boundary
$R_{\rm out}$	$2 \ldots 25 R_\star$	position of the outer boundary
$t_{\rm pis}$	$15P$	Time for the initial acceleration of the piston
$t_{\rm rezone}$	$0.5P$	Time interval between two rezoning procedures
$v_{\rm amp,0}$	5×10^4 cm/s	initial piston amplitude
$\epsilon_{\rm P}$	200	fraction of the period P for maximum time step : $\Delta t_{\rm max} = P/\epsilon_{\rm P}$
$\epsilon_{\rm CFL}$	$8 \times 10^{-3} \ldots 5 \times 10^{-2}$	*Courant-Friedrichs-Levy*-factor $\Delta t \overset{!}{<} \epsilon_{\rm CFL} \Delta x / v$
$\epsilon_{a_{\rm max}}$	0.1	maximum relative change of the particle sizes per time step
$\epsilon_{\kappa_{\rm d}}$	0.05	maximum relative change of the dust extinction $\kappa_{\rm d}$ per time step
$\epsilon_{\rm K_0}$	0.02	maximum relative change of the number of dust particles per time step
$\epsilon_{\rm K_3}$	0.01	maximum relative change of the $3^{\rm rd}$ dust moment per time step
ϵ_T	0.1	maximum relative change of $T_{\rm gas}$ per time step
$\kappa_{\rm gas}$	2×10^{-4} cm^2 g^{-1}	gas opacity (assumed constant)

Table 3.2: Parameters for the dynamical wind calculation.

3.4.3 Boundary Values

The hydrodynamical calculation requires an inner and an outer boundary condition. As inner boundary condition, the piston approximation (see Wood 1979) is chosen

$$v(R_{\rm in}, t) = v_{\rm amp}(t) cos\left(\frac{2\pi t}{P}\right). \tag{3.9}$$

As outer boundary, a constant pressure gradient is assumed (see Fleischer et al. 1992).

For the radiative transfer, two additional boundary conditions are required. At the inner boundary, the separation angle is set zero $\mu(R_{\rm in}) = 0$, and the stellar flux $F(R_{\rm in})$ is assumed to be constant, which results in a stellar luminosity that varies with the stellar radius

$$L_\star(t) = 4\pi {R_{\rm in}}^2(t) F(R_{\rm in}), \tag{3.10}$$

where F denotes the frequency integrated radiation flux, which relates to the frequency integrated Eddington flux H as $F = 4\pi H$. At the outer boundary, the optical depth is forced to vanish, and no external irradiation is assumed to exist.

3.4.4 Discretization

The spatial discretization follows the approach from Richtmyer & Morton (1967). Quantities that depend on a volume are defined between two grid points, all other quantities are defined at the position of the grid points.

In regular time intervals $t_{\rm rezone}$, the grid is *rezoned*, i.e. all grid points, that have wandered beyond the current outer boundary $R_{\rm out}(t)$ are discarded and reinserted into the grid. This reinsertion is not realized by simply inserting single grid points, but by splitting two zones into three, a procedure which allows for the conservation of all physical quantities (for details, see Fleischer 1994). With increasing integration time, the number of grid points is stepwise increased from $N_{\rm start}$ to $N_{\rm final}$.

The time steps are adapted dynamically. The corresponding parameters $\epsilon_{\rm criterion}$ in Table 3.2 give an overview over the various criteria used for the determination of the time step. Generally speaking, the maximum time step is the desired temporal resolution $\Delta t_{\rm max} = P/\epsilon_{\rm P}$, when determining the length of the next time step this value is checked against the various criteria (see Table 3.2) and the corresponding minimum time step is used.

3.4.5 The dynamical calculation

At first the hydrostatic dust-free start model is constructed. Then, the dynamical calculations are started "on top" of the start model. The piston amplitude $v_{\rm amp}$, the position of the outer boundary $R_{\rm out}$ and the number of grid points are slowly increased until the desired values are reached. The calculation is usually stopped after an integration time of $120P$.

Every single time step is calculated according to the following scheme:

1. Determination of the new velocity at the inner boundary
2. Calculation of the new position of the inner boundary
3. Calculation of the new velocity structure
4. Calculation of the new radial structure of the Lagrangean elements. At this time it is checked, whether the time step is alright, and – if not – jumped back to (1) with a shorter time step.
5. Calculation of the new density structure
6. Calculation of the artificial viscosity structure
7. Evaluation of the dust moment equations
8. Iterative semi-implicit evaluation of the energy equation, state equations and cooling functions
9. Evaluation of the radiative transfer
10. Calculation of the radiative accelerations for the next time step
11. Determination of the length of the next time step

Chapter 4

Gas box models

This chapter is divided into three parts. In the first two parts, the Fokker-Planck system Eq (2.66) is solved on top of the thermodynamic structure of a simple stationary wind for the LTE-case ($T_{\rm dust} = T_{\rm gas}$, Sect. 4.1) and one NLTE-case ($T_{\rm dust} = \overline{T}$, Sect. 4.2). The basic wind parameters of this stationary model are adopted from Dirks (2000) and given in Table 4.1. The Fokker-Planck system (2.66) is solved as described in Sect 3.2 using the wind structure from Table (4.1) as input for the calculation of the nucleation and growth rates. The time variable required for the solution of Eq. (2.66) is obtained via $t = (R - R_\star)/v_{\rm wind}$, where R is the distance from the centre of the star and $v_{\rm wind}$ the wind velocity, which is assumed constant (see discussion in Chapter 5).

In Sect. 4.3, some Monte-Carlo calculations are presented, where the deterministic dust equations (2.5) are solved on a random thermodynamical structure generated on the basis of the same wind model.

$\overline{T}(R)$	=	$T_\star\sqrt{R_\star/R}$
$R_\star$	=	$3.7 \cdot 10^{13}$cm
$T_\star$	=	2500K
$v_{\rm wind}$	=	20 km/s
$M_\star$	=	$1 M_\odot$
$\dot{M}$	=	$2 \cdot 10^{-5} M_\odot$/yr
$\bar{\rho}(r)$	=	$\dot{M}/(4\pi r^2 v)$
ϵ_C/ϵ_O	=	3

Table 4.1: Parameters of the stationary wind

4.1 LTE

In this section, calculations are presented, where the dust temperature $T_{\rm dust}$ is set equal to the gas temperature $T_{\rm gas}$. This corresponds to the approach used by Dirks (2000), who assumes the dust grains to be in thermal equilibrium with the gas phase at every moment in time, i.e. if the gas is heated by the temperature fluctuation, the dust is assumed to be also heated without delay.

After presenting an overview of the behaviour of the Fokker-Planck system (2.66) solved on top a stationary wind structure, some parameter studies are presented, in order to investigate the influence of the parameters describing the fluctuation σ and λ. Finally, a comparison between the results of this work and the model calculations from Dirks (2000) is presented.

4.1.1 The general picture

Figs. 4.1, and 4.2 show the results of an exemplary model calculation. The parameters of the fluctuation are $\sigma = 60$ K and $\lambda = 10^8$ s (Fig. 4.1) and $\lambda = 10^3$ s (Fig. 4.2). The integration width in temperature space was chosen as $\Delta T_{\rm max} = \gamma\sigma$ using $\gamma = 8$, i.e. $\Delta T_{\rm max} = \pm 480$ K in this model.

The right hand sides of each figure show the results for a grid of a purely deterministic calculation, i.e. a calculation where the deterministic dust equations (2.5) are solved as described in Sect. 3.1 on top of a temperature structure $T_{\rm gas}(r, T) = \overline{T} + T$ and a density structure which is adiabatically coupled according to Eq. (3.8) to the corresponding $\bar{\rho}(r)$. Note that in the deterministic calculation, there is no interaction between different temperature channels.

The left hand sides of Figs. 4.1, and 4.2 show the results of the stochastic calculation, i.e. the solution of the coupled set of Fokker-Planck equations (2.66) for the degree of condensation $f_{\rm c} = q_3/\epsilon_{\rm C}$ (top panel) and the dust particle density $n_{\rm d}/n_{\hat{\rm H}} = q_0$ ($2^{\rm nd}$ panel), and the nucleation rate J ($3^{\rm rd}$ panel) and the net growth rate τ^{-1} (bottom panel) calculated using the corresponding q_3 for the carbon consumption. The boundary paths ($T = \pm\Delta T_{\rm max}$) for the stochastic models are set to the corresponding deterministic paths, i.e. they are identical on the left and right sides from Figs. 4.1, and 4.2.

By looking at the deterministic plot for the $n_{\rm d}$ ($2^{\rm nd}$ panel at the right), one can clearly see, that in the channel with the lowest temperature, the dust formation starts at about 1.5 $R_\star$, whereas in the hottest channel it only starts at about 4 $R_\star$. In contrast, the model including temperature fluctuations (top left panel) shows quite uniform dust formation setting in at 1.5 $R_\star$, i.e. as soon as the dust formation starts in the coolest channel. This behaviour can be understood as the result of two effects: i) the direct transport of

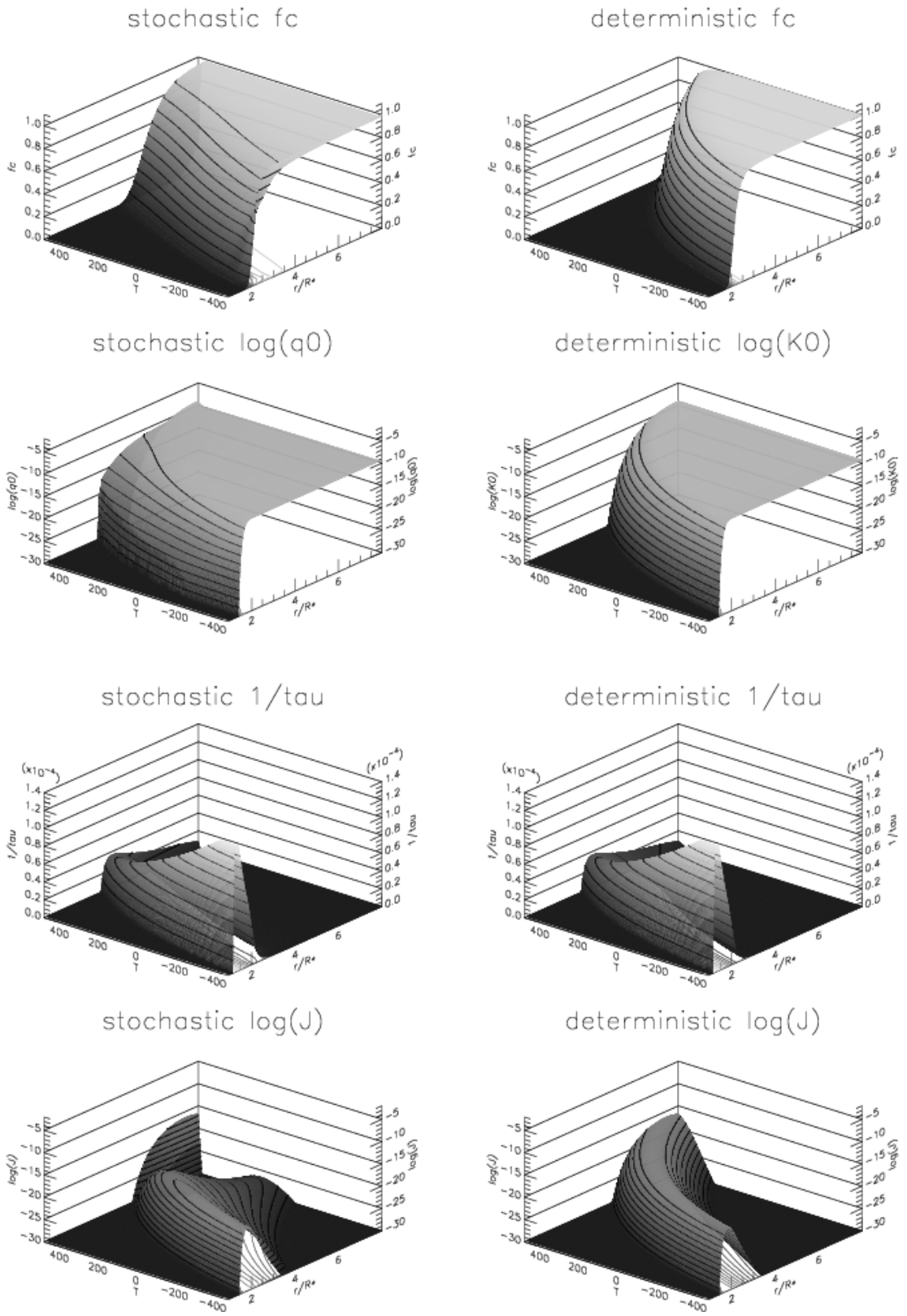

Figure 4.1: Comparison between the deterministic and the stochastic model. $\sigma = 60$ K, $\lambda = 10^8$ s

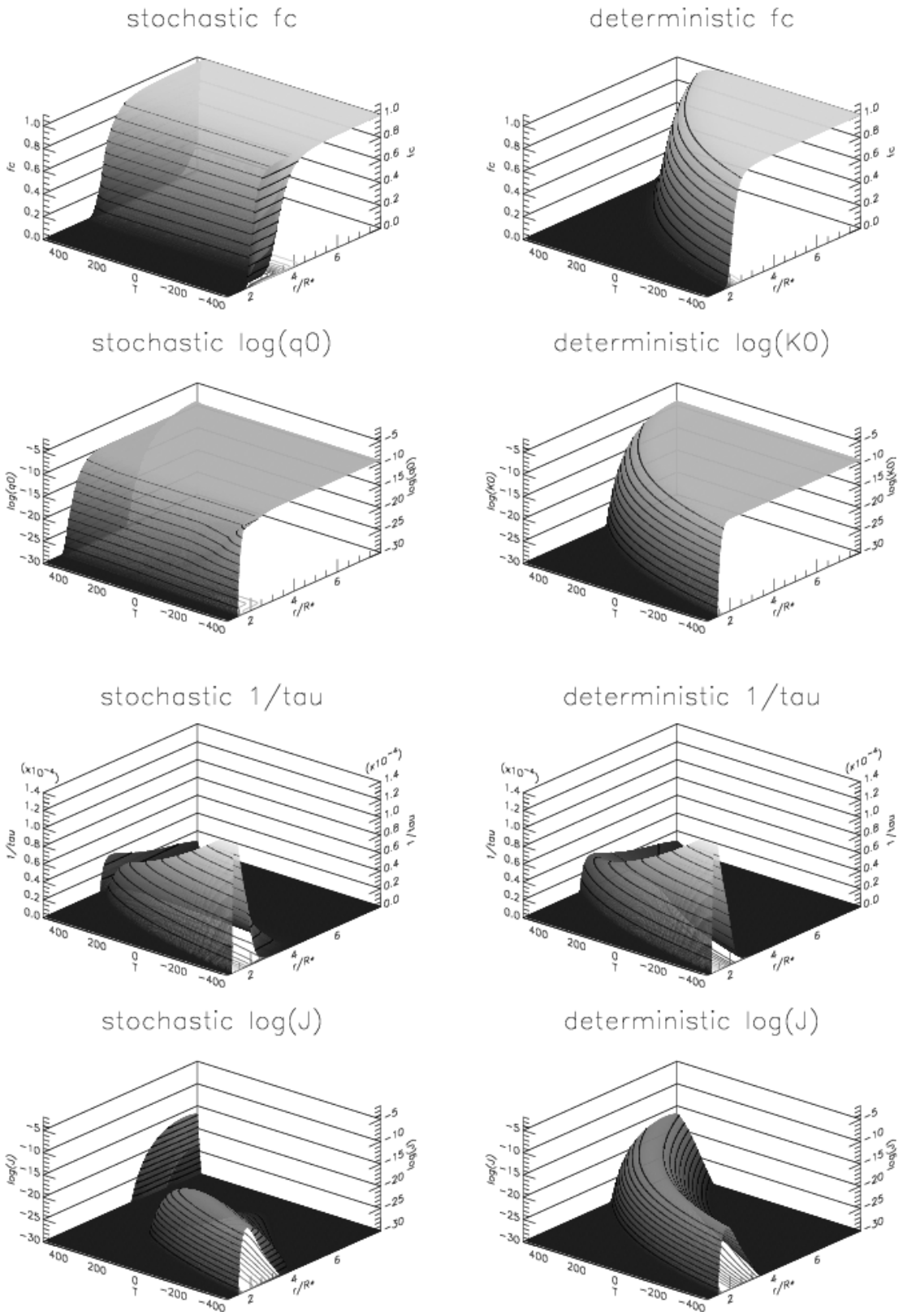

Figure 4.2: Comparison between the deterministic and the stochastic model in the microturbulent limit case. $\sigma = 60$ K, $\lambda = 10^3$ s

the q_ρ through the T-space via the drift and diffusion terms in the Fokker-Plank equation (2.66) and ii) the fact that under the given circumstances (i.e. the given $\overline{T}(r)/\overline{\rho}(r)$-structure) the conditions for dust *growth* are favourable earlier (i.e. at smaller distances from the star), than they become favourable for dust *nucleation* (see panel 3 and 4). Thus, the dust seeds which nucleate in the cool channels are transported[1] into the hot channels, where they meet conditions favourable for subsequent growth.

Figs. 4.2 shows the microturbulent limit case, which can be identified by the fact, that the q_ρ (here f_c and n_d) show no remarkable variation along the T-axis. Nucleation and growth rate still show their T-dependence, because they are not "mixed" directly by the Fokker-Planck equations, but only weakly coupled via the carbon consumption q_3.

The top panels of Figs. 4.1 and 4.2 show the degree of condensation f_c. In the microturbulent limit (Fig. 4.2), the model shows a nearly uniform degree of condensation for nearly all temperature channels except for the boundary channels. For the longer correlation time (Fig. 4.1) this behaviour is far less pronounced.

The vanishing influence of the boundaries can be seen very good at the plot of the stochastical nucleation rate in Fig. 4.1, bottom panel, where the nucleation rate of the deterministic boundary path looks nearly like a wall at the high temperature boundary, just like at the plot of the stochastical degree of condensation for the low boundary. In general, the influence of the boundary depends on the the correlation time λ of the fluctuation, on the width of the temperature channel $\sigma\gamma$, and on the number of grid points along the T-axis. These parameters have to be chosen in such a way that the influence of the boundary vanishes in the later calculation of the expectation values (see remarks in Sect. 3.2).

Fig. (4.3) shows the mean thermodynamic structure $\overline{T}(r)$ (red) and $\overline{\rho}(r)$ (blue) of the the wind (top panel) and (in panel 2 to 5) the comparison between the dust quantities calculated deterministically along the mean path (black) and the corresponding expectation values according to the solution of the system of Fokker-Planck equations (red). A look onto the nucleation rate (J_{N_ℓ}, panel 2), the dust particle density (n_d, panel 4) and the degree of condensation (f_c, panel 5) shows that dust formation is favoured by the temperature fluctuation: for the given parameters, nucleation sets in about $0.5R_\star$ earlier than in the deterministic case. For the degree of condensation (f_c, panel 5) the effect is weaker, but still obvious.

[1] "Transported" in this context means: a given gas element, which is subject to a temperature fluctuation, will keep the dust formed during this fluctuation, as long as it is not explicitly evaporated. In the 3D-representation of Figs. 4.1, and 4.2 this process can be understood as a transport between the different temperature channels.

Fig. 4.3 shows that, in general, the conditions for dust growth (panel 3) are most favourable shortly before they become favourable for nucleation. The injection of dust nuclei from a cooler channel can therefore be understood as an additional source of nucleation, inserting seed particles at a moment in time, where they will very effectively grow.

4.1.2 Some parameter studies

Fig. 4.4 shows a parameter study for variations of σ at $\lambda = 10^4$ s. In the second panel the logarithm of the expectation value of the stochastical nucleation rate is shown, i.e. the expectation value $\langle J \rangle (R)$ of the nucleation rate $J(R, T, q_3(R, T))$, which has been calculated using the carbon abundance $\epsilon_{\rm C}(R, T) = \epsilon_{\rm C,0} - q_3(R, T)$

$$\langle J \rangle (R) = \int_{-\Delta T_{\max}}^{+\Delta T_{\max}} J(R, T, q_3(R, T)) p(T) {\rm d}T. \tag{4.1}$$

Panel 3 shows the corresponding expectation value for the net growth rate $\tau^{-1}(R)$, which was calculated analogously. Panel 4 shows the expectation value for the dust particle density (in units of $n_{\hat{\rm H}}$) calculated as

$$\langle n_{\rm d} \rangle (R) = \int_{-\Delta T_{\max}}^{+\Delta T_{\max}} q_0(R, T) p(T) {\rm d}T. \tag{4.2}$$

Panel 5 shows the expectation value for the degree of condensation $\langle f_{\rm c} \rangle$ which is given by

$$\langle f_{\rm c} \rangle (R) = \int_{-\Delta T_{\max}}^{+\Delta T_{\max}} \frac{q_3(R, T)}{\epsilon_{\rm C,0}} p(T) {\rm d}T. \tag{4.3}$$

The most important trend for an increasing rms temperature deviation σ is that the nucleation (panel 2) starts closer to the star, resulting in a faster increase of the dust particle density $n_{\rm d}$ (panel 4), and the degree of condensation $f_{\rm c}$ (panel 5). A closer inspection of panel 2 reveals, that the peak value of the nucleation rate decreases with increasing σ, which results in a slightly lower final dust particle density, as can be seen by a very close look to panel 4. The peak of the net growth rate τ^{-1} (panel 3) wanders slightly outwards with increasing σ and decreases in height. Note, however, that τ^{-1} is plotted on a linear scale in panel 3, while J and $n_{\rm d}$ are plotted on logarithmic scales in panel 2 and 4.

An interesting feature of the σ-study is the fact that, for small values of σ, the stochastic model approaches[2] the deterministic one. This behaviour was

[2]Indeed, for $\sigma = 1$ K the on plots like shown in Fig. 4.4 there is really no more difference perceivable, which is why such a plot is *not* shown in this work

expected (see discussion in Dirks 2000), because the limit case of arbitrarily small fluctuations leads back to the deterministic structure.

Fig. 4.5 shows a set of models for a varying correlation time λ. The represented quantities are the same as in Fig. 4.4. The deterministic hydrodynamical structure $\overline{T}(R)$ (red), $\overline{\rho}(R)$ (blue), shown in the top panel is identical for both plots.

The main feature is, that there is an overall difference between the ensemble of the stochastic models and the deterministic model, while the differences between the various stochastic plots are small. In particular, during the important phase of the onset of nucleation and growth (panel 2 and 3, at $R = 2 - 3$), one can hardly perceive a difference between the various correlation times. The development of the grain number density (panel 4) reveals some differences at very low densities, where, for longer correlation times, n_d seems to increase a bit faster. However, when the condensation is complete, the final values for n_d are all off the same order of magnitude. An interesting feature can be seen when looking at the degree of condensation f_c in panel 5. It looks like the models are switching between two limit cases. The microturbulent case, where the plot for f_c seems to be shifted by $\approx 0.4 R_\star$ towards the star (blue and green line, for $\lambda = 10^4 \ldots 10^7$ s) and the macroturbulent limit (cyan and red line), where the condensation sets in earlier but increases slower than in the microturbulent or deterministic case. All in all, the parameter study for λ shows, that the influence of this parameter is weak.

Unlike for the variation of the rms temperature deviation σ, the variation of λ never leads back to a (pseudo)-deterministic behaviour. The microturbulent limit case (blue lines) corresponds to an immediate mixing of the q_ρ of the various temperature channels (along the T-axis in Figs. 4.1, and 4.2), whereas the structure of the macroturbulent limits case can be obtained by averaging the isolated deterministic paths weighted with $p(T)$.

$$q_{\rho_\mathrm{macroturbulent}}(R) = \int_0^\infty K_\rho p(T) \mathrm{d}T. \tag{4.4}$$

4.1.3 Comparison to earlier work

In this section the gas box models described in the previous two sections are compared with the results from Dirks (2000) who performed similar model calculations. From a mathematical point of view, both model families are identical, despite the fact that Dirks (2000) arrived at a set of Fokker-Planck equations similar to Eq. (2.66) by first assuming spherical symmetry and then performing a set of transformations, while in this work Eq. (2.66) is

interpreted as a gas box model subject to the external wind structure given in Table (4.1). However, the resulting equation system is identical. Numerically, Dirks (2000) has programmed a FORTRAN code for the solution of the Fokker-Planck equations, where the routines for calculating the time development of the dust moments were taken from the CHILD-code (described in Sect. 2.3), whereas for this work the entire code was written completely from the scratch in C.

Figs. (4.6) and Fig. (4.7) show a comparison between the models resulting from this work (bottom) and between some results from Dirks (2000) (top). The top[3] pictures are screenshots taken from Dirks (2000), while the bottom pictures are plots from models calculated with the same model parameters. The colour coding in all plots is alike, however in the bottom plots the deterministic model was omitted. The general appearance of both model families is nearly identical, except for slight differences in Fig. (4.7) for large values of λ. The difference between these plots and the corresponding parameter studies presented in the previous section results from the fact, that the parameter $\gamma = 3.29$ was chosen too small by Dirks (2000), which leads in most cases to a behaviour, where, instead of representing the intended solution from Eq. 2.66, the q_ρ contain only the arithmetic mean between the two boundary paths. This explains, for example, the plateaus of the degree of condensation in panel 5 of all plots, which lie exactly at $f_c = 0.5$, i.e. the first step results from the increase of $f_c(-\Delta T)$ from 0 to 1 in the lower boundary path, and the second step results from the increase of $f_c(+\Delta T)$ from 0 to 1 in the upper boundary path.

However, the fact that the models look identical for the same parameters, even in this numerically problematic region, can be regarded as a good hint, that both codes solve the problem, in principle, in a correct way.

[3]resp. the ones on the r.h.s. when turning the page in way that the labels are upwards

Figure 4.3: Comparison between the deterministic model along the mean path and the expectation values of the stochastical model. $\sigma = 60$ K, $\lambda = 10^4$ s, $\gamma = 5$.

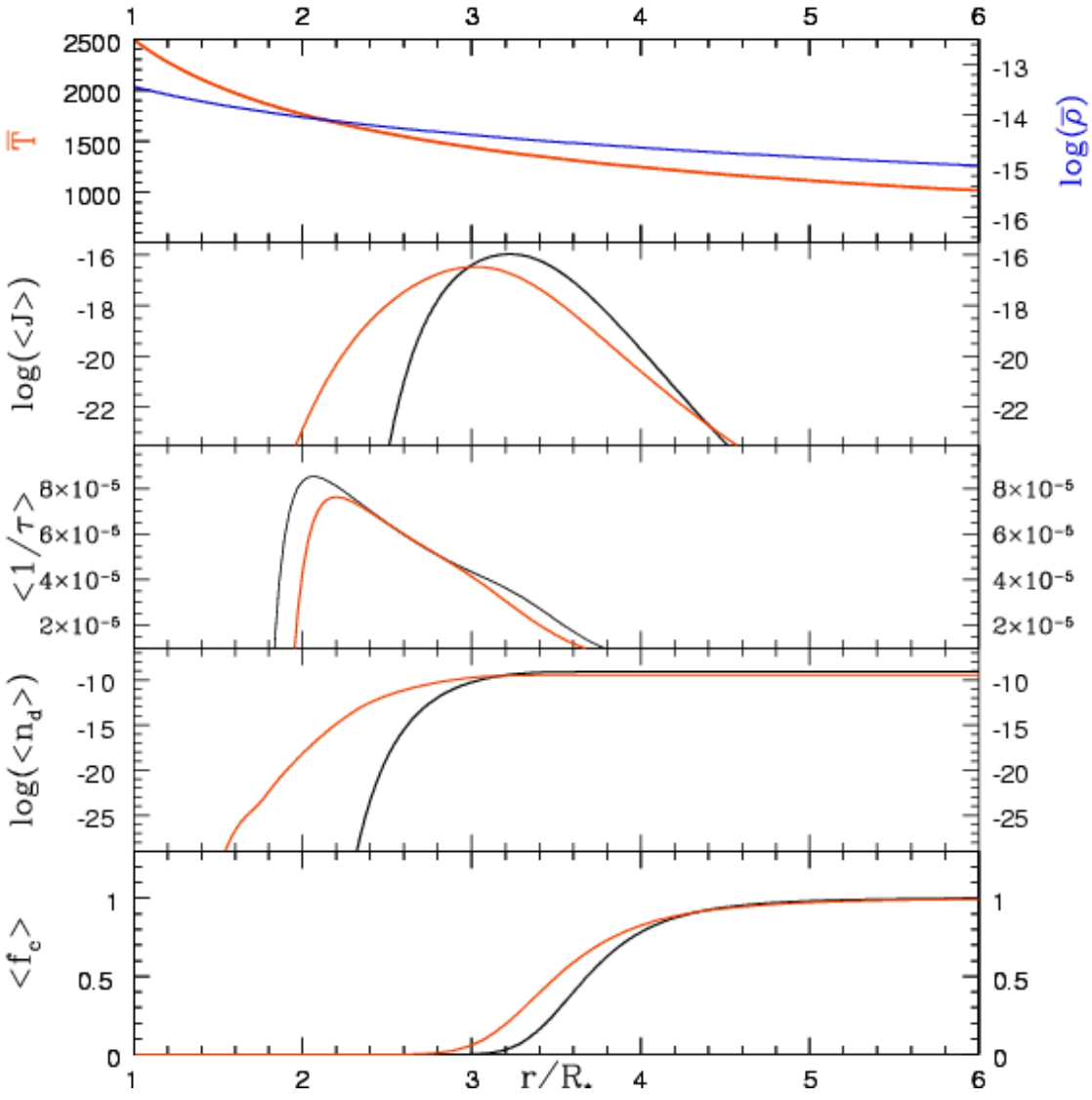

Figure 4.4: Parameter study for $\sigma = 20$K (blue), 40K (green), 60K (red). For comparison, the deterministic model is also plotted (black line). $\lambda = 10^4$ s, $\gamma = 8$.

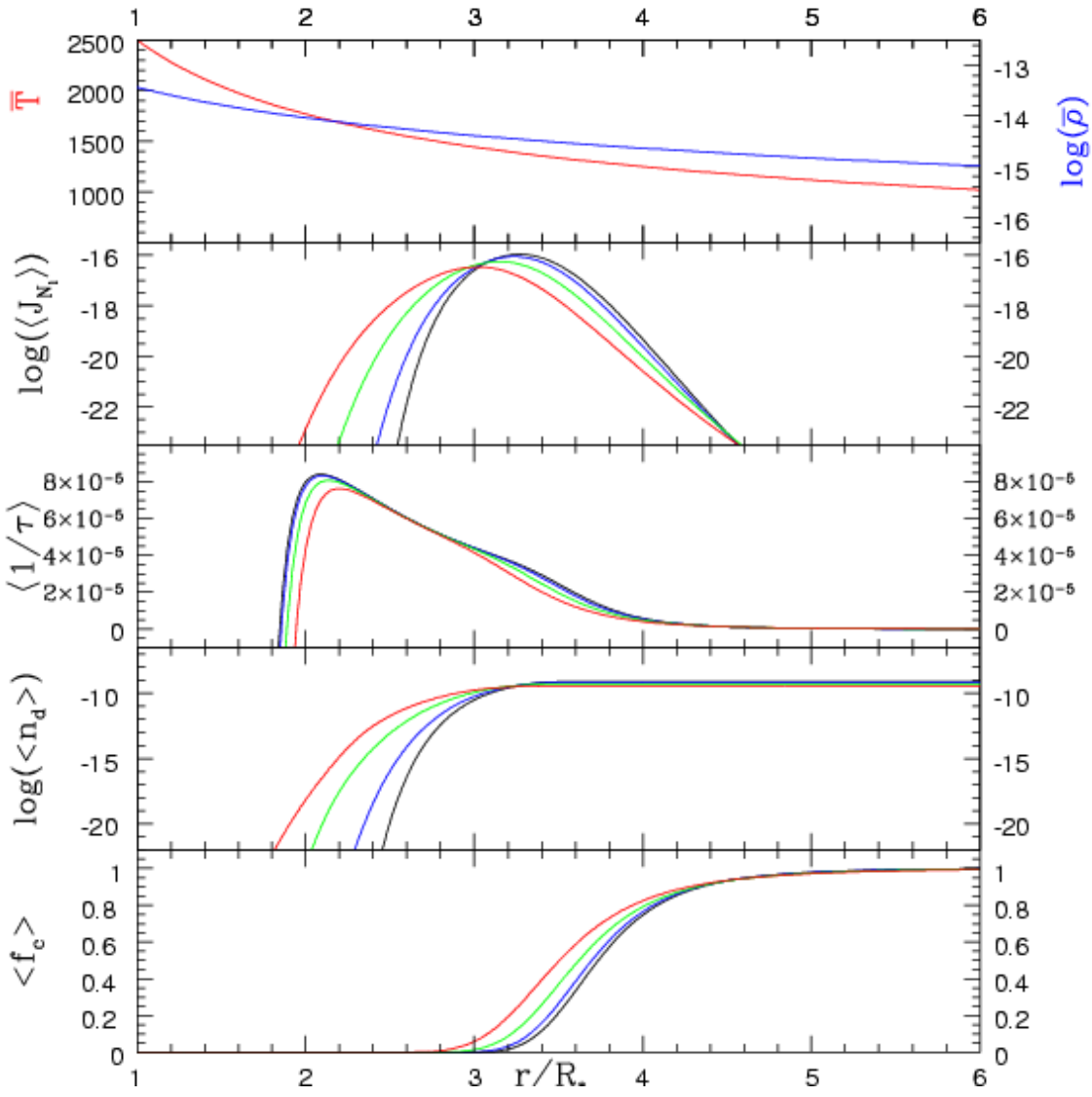

Figure 4.5: Parameter study for $\lambda = 10^4$ s (blue), 10^7 s (green), 10^8 s (cyan), 10^9 s (red). For comparison, the deterministic model is also plotted (black line). $\sigma = 60$ K (top), $\gamma = 8$.

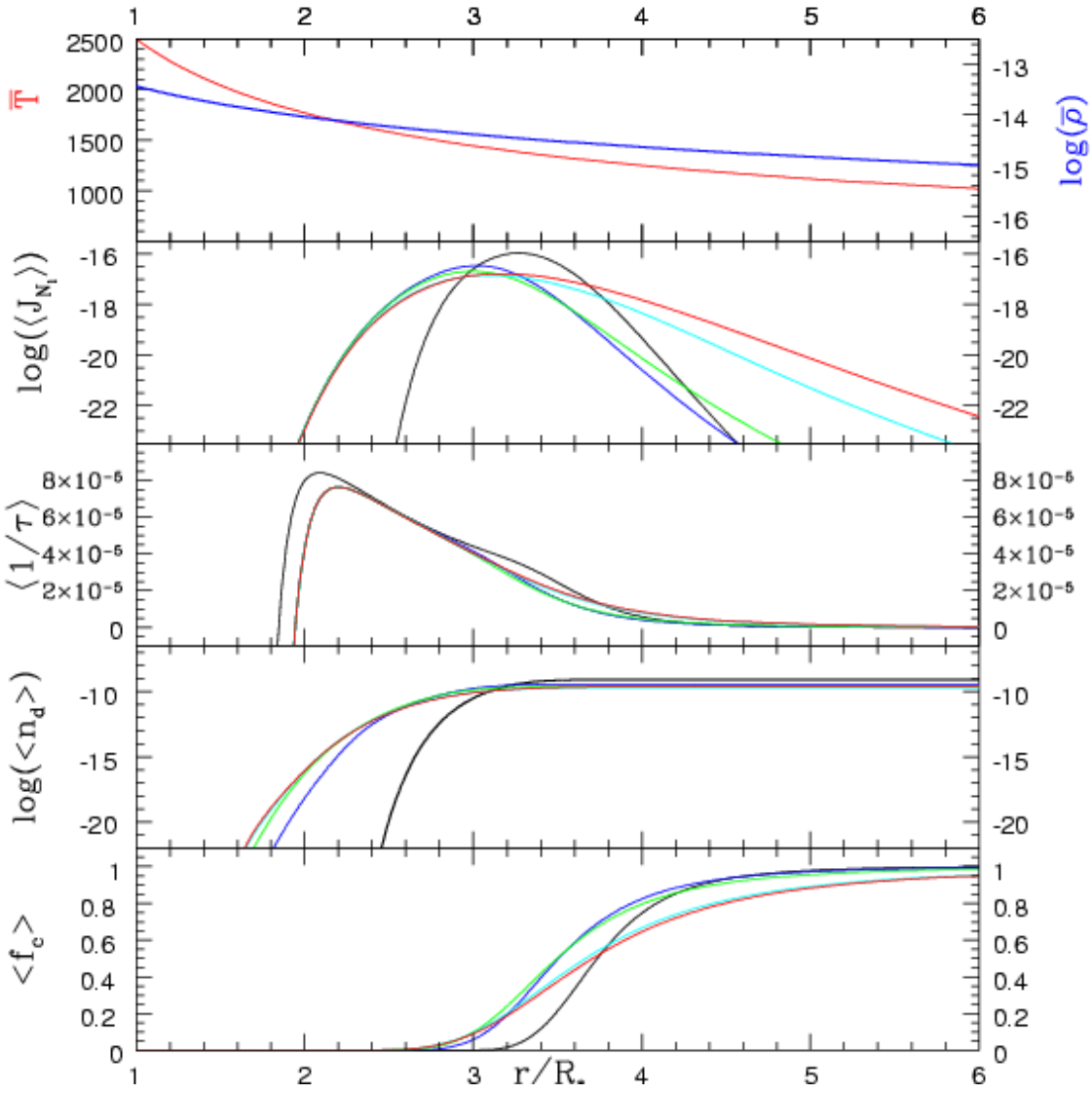

Figure 4.6: Dust nucleation and growth under the influence of temperature fluctuations with $\lambda = 10^3$s, $\gamma = 3.29$ and $\sigma = 20$K (dark blue), 40K (pink), 60K (yellow), 80K (cyan). Top: results from Dirks (2000) (the black curves correspond to the deterministic model), Bottom: Results from this work.

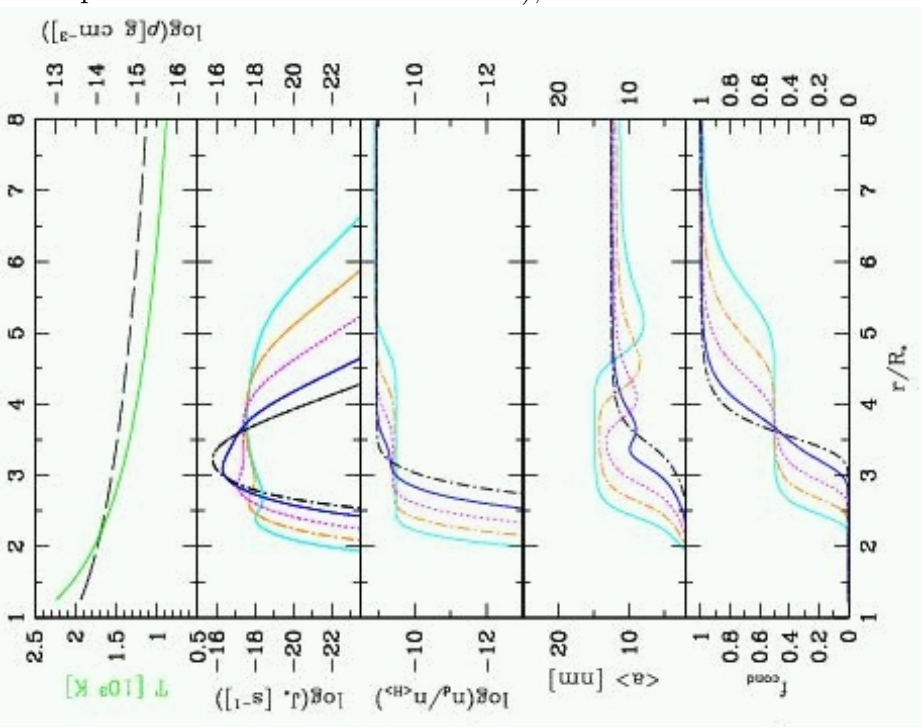

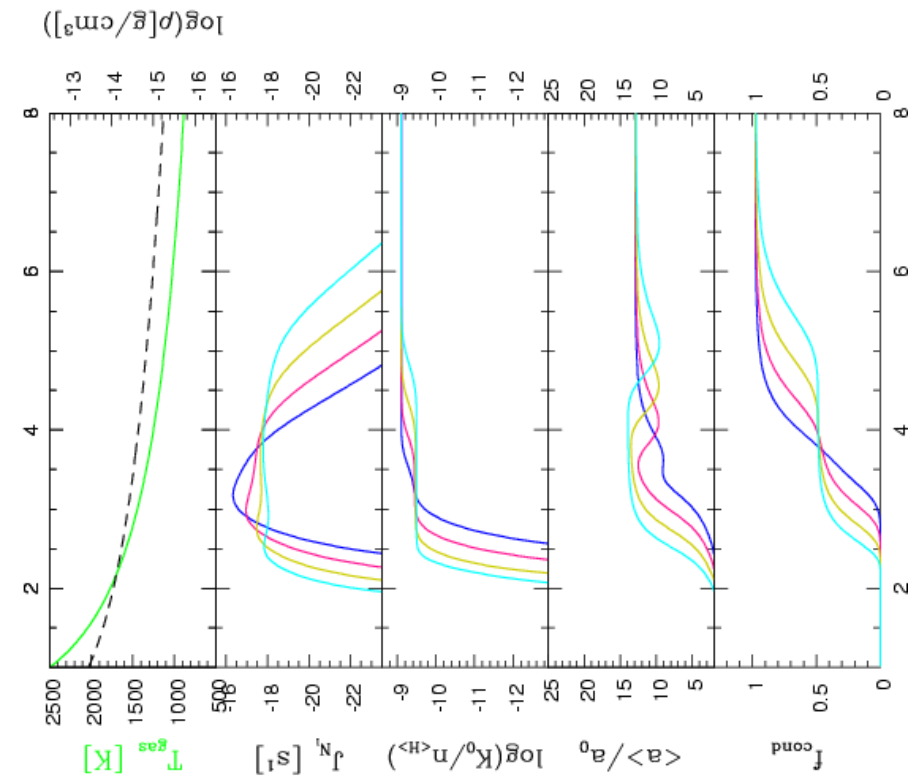

Figure 4.7: Dust nucleation and growth under the influence of temperature fluctuations with $\sigma = 60$K, $\gamma = 3.29$ and $\lambda = 10^3$s (black), 10^4s (dark blue), 10^5s (pink), 10^6s (yellow), 10^8s (cyan). Top: results from Dirks (2000) (p.61 ,Fig. 6.1), Bottom: Results from this work.

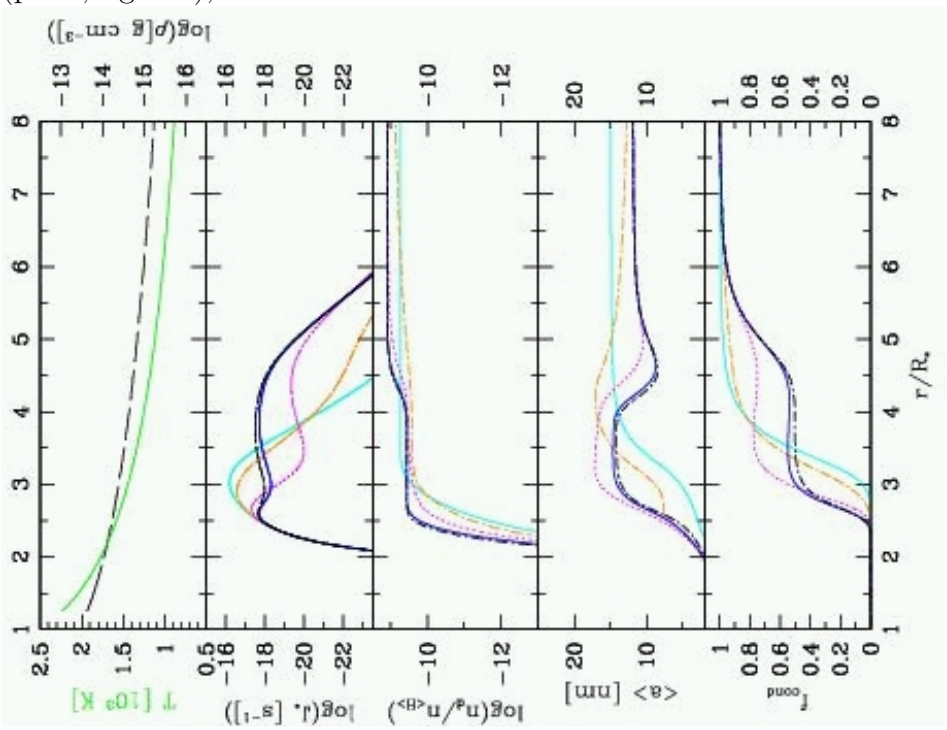

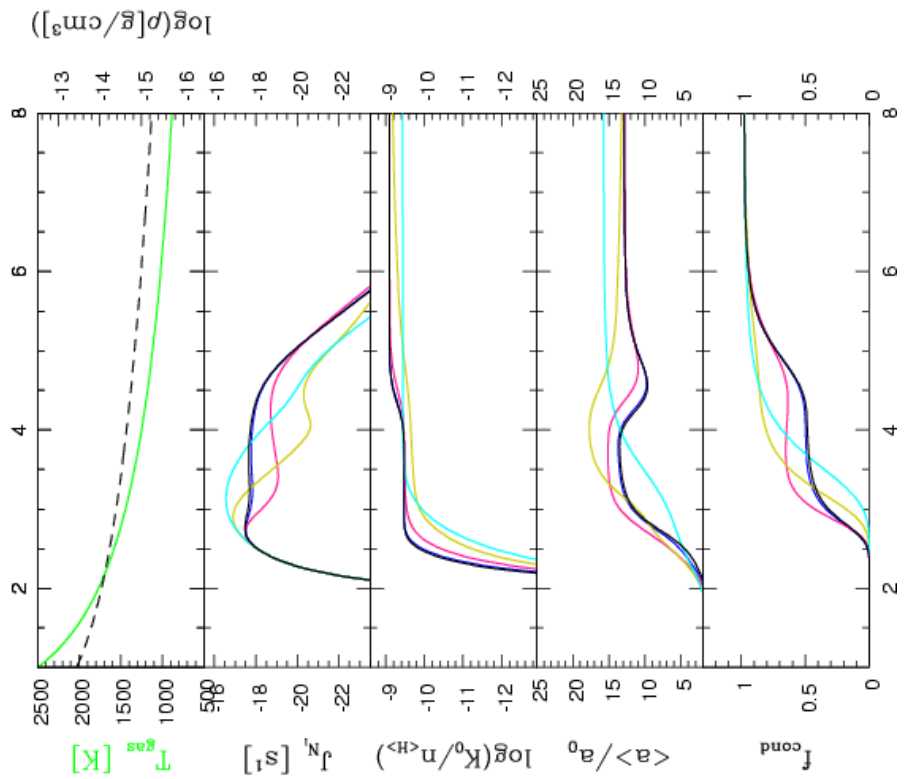

4.2 NLTE

In order to study the influence of possible deviations between the gas temperature $T_{\rm gas}$ and the dust temperature $T_{\rm dust}$, some models were calculated, where the dust temperature $T_{\rm dust}$ is assumed to remain at the mean temperature during a fluctuation of the gas temperature $T_{\rm gas}$. This approach could, for example, describe a situation, where i) the dust is coupled energetically to the radiation field rather than to the gas phase and ii) the stellar radiation field is not expected to be considerably altered by a local temperature fluctuation.

Fig. 4.8 shows the results of this set of calculations for different values of σ in the microturbulent limit case ($\lambda = 10^3$ s). Note that – in contrast to Fig 4.6 – σ is only varied from 1 K to 15 K.

The difference between these models and the LTE is drastic. The onset of nucleation (panel 2) does not just occur at higher temperatures, but the peak value of the nucleation rate is also increased by about two orders of magnitude for $\sigma = 15$ K (red line) compared to the deterministic reference model (black line). This early onset of very efficient nucleation leads to a much faster condensation of all available material, $f_{\rm c}$ (panel 5) reaches the value of 1 (complete condensation) at about $2.6R_\star$ for $\sigma = 15$ K compared to the value of about $5.3R_\star$ for the deterministic case. This fast consumption of all material available for condensation leads to an abrupt breakdown of the growth rates τ^{-1} (panel 3) at the moment where the degree of condensation $f_{\rm c}$ (panel 5) begins to rise. The final dust particle densities $n_{\rm d}$ (panel 4) are about one order of magnitude higher than in the LTE-case, probably due to the higher peak values of the nucleation rates, which produce more nuclei before the available carbon is exhausted.

The drastic increase of the nucleation rate results from an increase of the supersaturation ratio S, when the gas temperature $T_{\rm gas}$ exceeds the dust temperature $T_{\rm dust}$, (see Eqs. 2.17 and 2.18, and the related discussion in Sect. 2.1.3). All in all, the deviation between $T_{\rm dust}$ and $T_{\rm gas}$ has a very large impact on the condensation process. In particular, if $T_{\rm dust}$ is below $T_{\rm gas}$, the nucleation rate can be raised by orders of magnitude even for moderate deviations. In these models, the condensation sets in earlier in the hot paths, where $T_{\rm gas} > T_{\rm dust}$ unlike during the LTE situation with $T_{\rm dust} = T_{\rm gas}$, where the condensation sets in earlier in the cool paths (see Figs. 4.1, and 4.2). Thus, within the thermodynamical dust-forming window, the local influence of the difference between $T_{\rm gas}$ and $T_{\rm dust}$ is stronger, than the influence of the (joint gas- and dust-)temperature in the case of LTE.

The possible implications of this result are discussed in Chapter 5. The influence of the correlation time on these models is as weak as in the LTE-

case, which is why a corresponding plot with a parameter study for the correlation times was omitted for this model family.

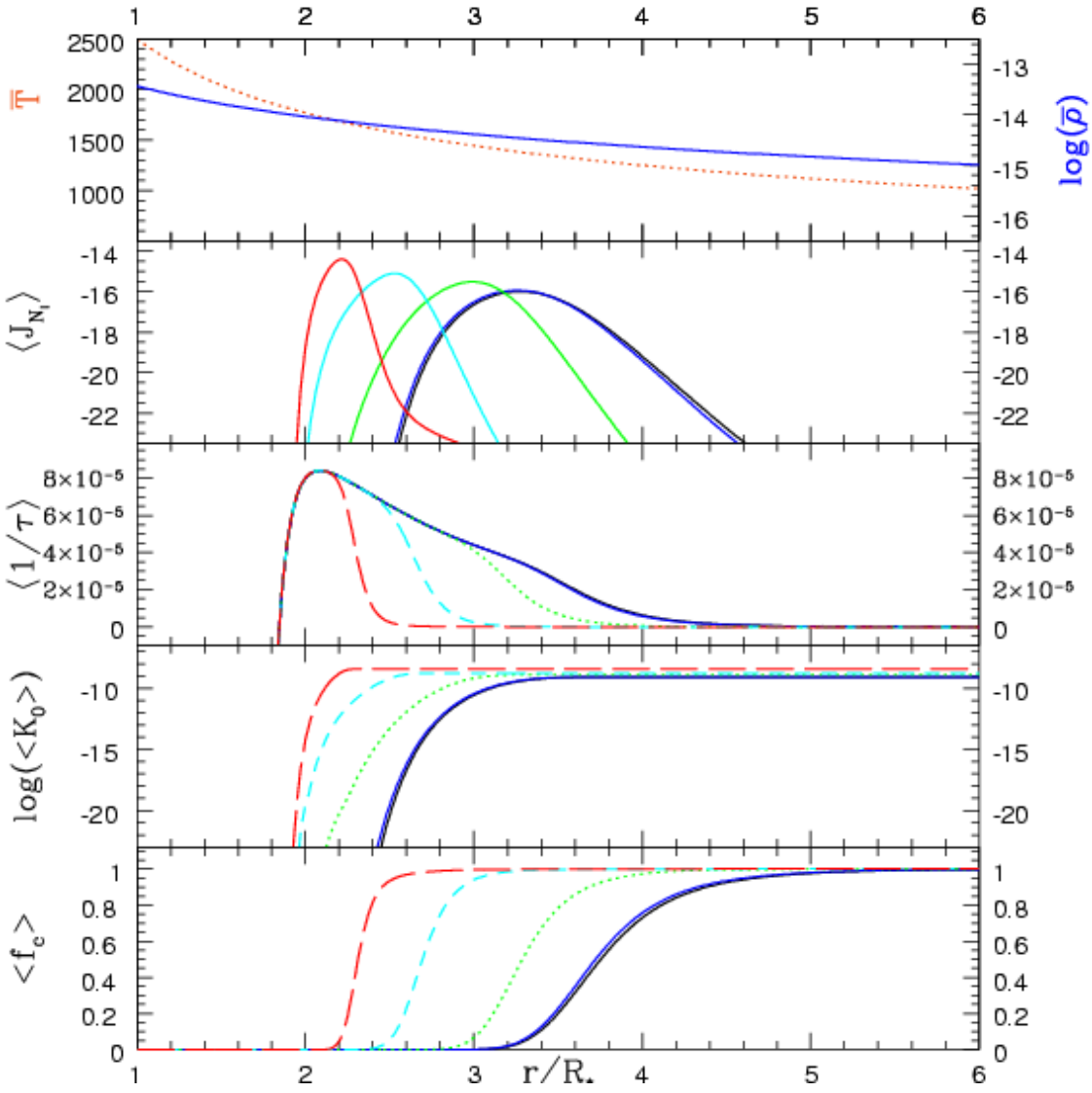

Figure 4.8: Parameter study for $\sigma = 1$K (blue), 5K (green), 10K (cyan), 15K (red). For comparison the deterministic model is also plotted (black line). $\lambda = 10^3$ s, $\gamma = 8$.

4.3 Monte-Carlo calculations

Fig. 4.9 shows some results from the Monte-Carlo calculations, which were performed according to the description in Sect. 3.3. In contrast to the calculations presented in the previous sections of this chapter, the models presented in Fig. 4.9 are not expectation values resulting from the solutions of the Fokker-Planck equations (2.66), but they represent particular random representants of the stochastic process $(\Theta, \mathcal{K})_t$, described in Section 2.2.

The hydrodynamical structures $T_{\rm gas}(R)$, $\rho(R)$ depicted in the top panels off all 6 plots in Fig. 4.9 are obtained from the wind model acc. to Table (4.1) by adding a correlated random temperature deviation to the mean temperature $\overline{T}(R)$, which was parametrised by the same parameters σ and λ, that occur in the Fokker-Planck equations (2.66). All models have been calculated under the assumption $T_{\rm dust} = T_{\rm gas}$.

The quantities presented in the 5 panels of each plot are, in principle, the same as in the corresponding plots in the previous sections, except for the fact, that in this section they have no statistical character, as do the expectation values from the previous sections. In this Section, the quantities presented correspond to the deterministic quantities if one assumes, that the hydrodynamical structure in each top panel represents an actual development of gas temperature $T_{\rm gas}$ and density ρ for that particular gas box.

The aim of these calculations is mainly to gain an insight on the particular representants of the stochastic process $(\Theta, \mathcal{K})_t$ and their dependence on the parameters σ and λ, because these single representants are the members of the ensemble, the expectation values of which were presented in the previous sections. For a later interpretation it seems therefore very useful to gain an idea of what the particular wind elements do look like, before being subjected to the statistical treatment that results in the Fokker-Planck equations (2.66). The problems, that occur during the attempt of subjecting a *stationary* wind model to a *particular* fluctuation are discussed in Chapter 5.

The results shown in Fig. 4.9 correspond to three exemplary combinations for λ and σ (top: $\lambda = 10^7$ s, $\sigma = 60$ K, middle: $\lambda = 10^4$ s, $\sigma = 60$ K, bottom: $\lambda = 10^4$ s, $\sigma = 20$ K), each showing two different representants (left and right) for the same pair of parameters, which differ by a different initialisation of the random number generator.

The top two models for $\lambda = 10^7$ s are close to the macroturbulent limit case. (The macroturbulent limit case itself, for e.g. $\lambda = 10^9$ s, would correspond to a structure, where the entire $T_{\rm gas}$-structure is shifted by a random value, and the corresponding plot looks like a randomly shifted deterministic plot.) For the first representant (left) the nucleation process reaches its peak later than the deterministic reference model (black line), which results in

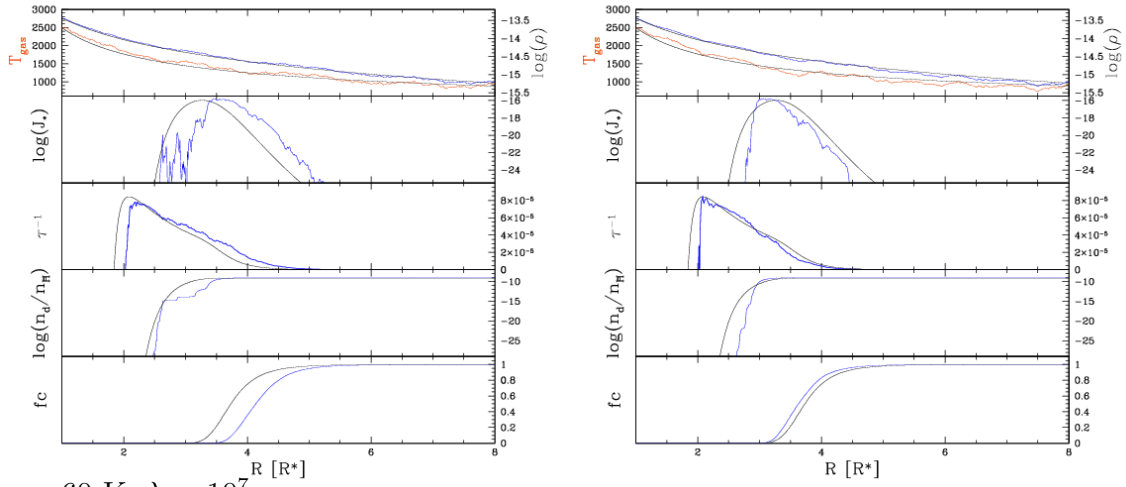

$\sigma = 60$ K, $\lambda = 10^7$ s

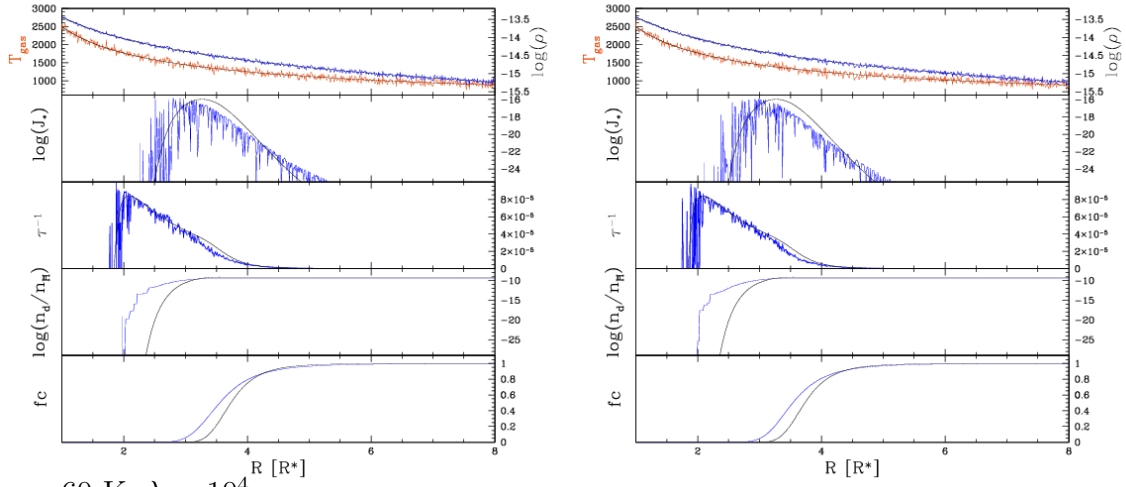

$\sigma = 60$ K, $\lambda = 10^4$ s

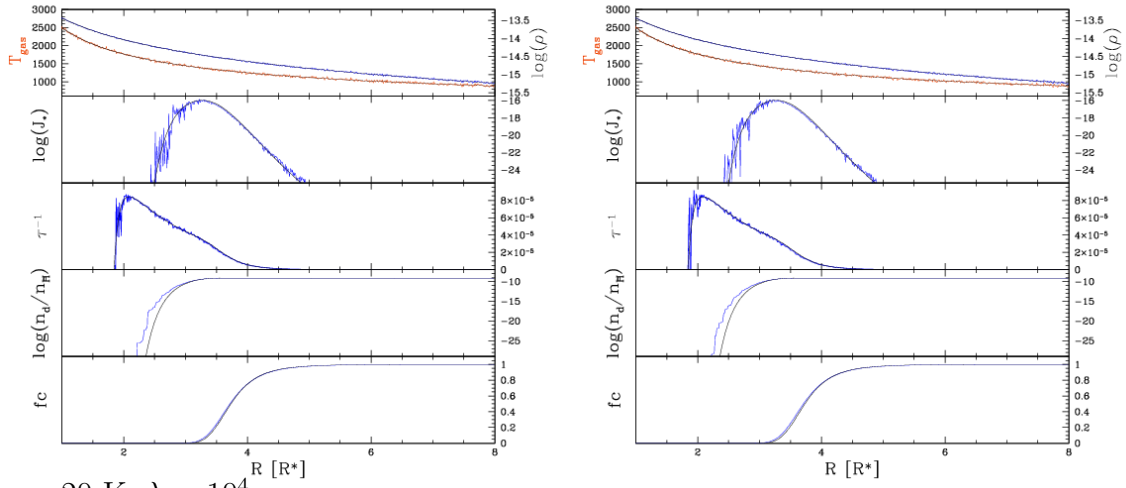

$\sigma = 20$ K, $\lambda = 10^4$ s

Figure 4.9: Selection of representants of the Monte Carlo calculations.

a an outward shift of the runaway condensation (see f_c, panel 5) by about 0.5 $R_\star$. For the second model (right), the nucleation peaks earlier and higher than in the deterministic reference model, resulting in a slight inward shift of the main condensation region. Note, however, that in both cases the nucleation seems to start later than in the deterministic case. This is a random feature which, nevertheless, gives two interesting insights: i) the position of the peak of the nucleation rate is more important for the subsequent condensation than the first appearance in the logarithmic plots presented in this chapter, and ii) the random nature of these models considerably reduces the significance of a single model for a quantitative interpretation.

The middle of Fig. 4.9 shows two representants for the same σ but in the microturbulent limit ($\lambda = 10^4$ s, for lower values of λ the calculation time increases significantly, because shorter time steps are needed. Furthermore, due to the higher number of random numbers required for the generation of the temperature structure, the numerical problems described in Sect. 3.3 become significant.) In this case, it can be seen, that the overall condensation process, which is best indicated by the development of the degree of condensation f_c (panel 5), is alike for both models, despite the fact, that the details (panels 1 to 4) vary remarkably. These plots look alike for all representants of the microturbulent limit case, i.e. there are no models, where the plot for f_c is shifted by a considerably different amount, or even in the other direction.

Finally, in order to give an impression of a variation of the parameter σ in this context, in the bottom panel, two more representants of the microturbulent limit case for $\sigma = 20$ K are presented. As expected, the temperature deviations (top panel) are smaller, an so are their effects on all other quantities.

Chapter 5

Discussion of the gas box models

5.1 General remarks

In order to properly discuss the results of the gas box models presented in the previous chapter, it is useful to resume the mathematical nature of the calculated quantities. The $q_\rho(t,T)$ that result from the Fokker-Planck system Eq. (2.66) can be interpreted as conditional expectation values of the random variables $\hat{K}_\rho$ of the stochastic process $(\Theta,\mathcal{K})_t$ under the condition that the deviation from the mean temperature $\overline{T}$ has the value T at the moment t. Since the mean temperature $\overline{T}$ in the models presented in chapter 4 is a function of time, the resulting q_ρ depend on the applied wind model (Table 4.1). A solution $q_\rho(t,T)$ is thus determined by the underlying deterministic wind model, i.e. the functions $\overline{T}(t)$, and $\overline{\rho}(t)$, the initial and boundary values, and the choice of the parameters σ and λ describing the nature of the assumed temperature fluctuations.

In contrast to the conditional expectation values q_ρ resulting from the Fokker-Planck system, the Monte-Carlo models presented in Sect. 4.3 deliver deterministic solutions K_ρ of particular random wind-structures, which are obtained by a random variation of the same mean temperature structure that was used for the solution of the Fokker-Planck system, using a consistent choice for the fluctuation parameters σ and λ.

It is important to point out that neither of the two approaches can be interpreted as a consistent model for a stationary wind. The most obvious reason for this circumstance is, that – strictly speaking – a stationary wind cannot be subject to a temporal fluctuation, whereas on the other hand any *temporally stable* inhomogeneous spatial structure, which could look some-

what like the Monte-Carlo models in Fig. 4.9, should be a solution of a stationary wind equation, and such solutions have never been found.

Unfortunately, the idea of a stationary wind would be the natural association for a stochastic process of the type $(\Theta, \mathcal{K})_t$, because that process depends on one parameter only, namely the time t. In a stationary situation, this parameter can be mapped to the radial position r of a wind element via $r = \int_0^t v(t')\mathrm{d}t'$ without problems, and the stochastical process $(\Theta, \mathcal{K})_t$ would be a wonderful model for a such a stationary wind.

However, when looking at the microphysics of a wind element subject to a temperature fluctuation, the physical and chemical processes will always depend on the time t via the fluctuation itself and other time dependent chemical and physical processes and on the material surrounding the wind element, to which it is coupled via the non-local equations of radiative transfer. Any wind element would therefore depend not only on its own history, but is also coupled to its environment at each moment in time. This spatio/temporal coupling cannot be described by a Markov process like $(\Theta, \mathcal{K})_t$.

For this reason, the model calculations presented in the last chapter can only be interpreted as gas box models, i.e. as models for the temporal evolution of the conditional expectation values q_ρ of the random variables $\hat{K}_\rho$ in a volume element that was subject the the temporal variation of $\overline{T}$ and $\overline{\rho}$ as given by the wind model acc. to Table 4.1. No feedback of the modified dust condensation to the wind model is included, because it cannot be included within the framework of the stochastical fluctuation model used in this work. Under this point of view, the Monte-Carlo models have to be interpreted accordingly, despite for the fact, that they do not deliver conditional expectation values, but deterministic solutions for a random situation.

For the interpretation of the significance of the models for the appearance of real singular objects, this circumstance leads to two important conclusions:

- In the microturbulent limit, it can be assumed that the fluctuations are fast enough to have an immediate influence on the system on time scales short compared to the variation of the mean temperature $\overline{T}$. In this case, the deterministic quantities K_ρ and all resulting quantities, like the opacity and the resulting acceleration of the gas, can in principle be substituted by corresponding microturbulent quantities. All equation systems – no matter whether they describe stationary or time dependent situations – can then be solved exactly like in the deterministic case. Under the numerical point of view, this would constitute a one-parametric (σ) sub-grid modelling of the fluctuations.

- In all other cases, it is not admissible to exchange the deterministic quantities K_ρ by any stochastical equivalents. All expectation values

gained by the resulting q_ρ of the Fokker-Planck equations can only be interpreted as ensemble averages over different gas boxes, and no information about the feedback on the wind via acceleration or radiative transport can be gained by the presented model calculations. For numerical model calculations describing a particular wind, this means, that in meso- or macroturbulent situations the fluctuations have to be resolved numerically so that their non-local influence on the wind are properly included. If the correlation time λ is short compared to the typical time steps of the numerical wind model under consideration, a two-parametric (σ and λ) sub-grid model could in principle be implemented, however, in this situation, the resulting wind structures would again represent ensemble averages over a family of wind situations and could not be interpreted straight forward as representation of a particular object.

5.2 The wind model

5.2.1 The choice of the turbulence parameters

Since no observational details about temperature fluctuations in the circumstellar envelopes of AGB-stars are available, the values for the rms temperature deviation σ and the correlation time of the fluctuations λ have been chosen according to the following considerations.

Mathematically, σ could have any positive value. $\sigma = 0$ K corresponds to the deterministic limit case. For a value of $\sigma = 1$ K, some models have been calculated for test purposes, and the results have indeed shown structures, that looked identical to the deterministic reference model.

In the LTE-case, σ was then increased by steps of 20 K until the calculations for the lower boundary ran into numerical problems. Using a value of $\gamma = 8$, this was usually the case for a value of about 80 K, which means that the lower boundary lies 640 K below the deterministic structure, where in the outer parts of the atmosphere the temperature of the lower boundary drops below 500 K, which is the value onto which the chemical data used in this work are reliable.

Considering the fact, that e.g. in the solar granulation, which is a result of the solar convection, temperature deviation of more than ± 100 K are observed, this choice of σ does on the other hand not seem completely exaggerated. Higher values for σ might be imaginable in the inner part of the envelope, where the temperature is still high. However, since our formalism requires a unique value of σ for the entire structure, a restriction for σ to

values of about $60 \ldots 80$ K seemed preferable to an arbitrary cut-off, of the stochastic treatment of the model at some radial distance from the star.

The values chosen for λ range from $10^3 \ldots 10^9$ seconds, where the resulting structures are close to the microturbulent ($\lambda = 10^3$ s) and the macroturbulent ($\lambda = 10^9$ s) limit cases. The macro- and microturbulent limit cases can be identified by 3D-plots, like Fig. 4.1, and 4.2.

5.2.2 Approximations of the wind model

The underlying wind model for all calculations of Chapter 4 (given by the parameters in Table 4.1) is certainly a very simple one and needs some further discussion.

As was pointed out in the beginning of this chapter, it is principally impossible to consistently solve an equation describing a stationary wind using the stochastical formalism presented in Sect. 2.2. It is therefore necessary to solve the Fokker-Planck equations (2.66) on top of a deterministic input structure for $\overline{T}(t)$, and $\overline{\rho}(t)$.

The two most unrealistic features of the chosen structure seem to be i) the constant wind velocity and ii) the rather high value of the carbon to oxygen ratio $[C/O] = 3$. However, both these assumptions result from the same problem.

Obviously, every stellar wind starts with a slow velocity at the "surface" of the star, and is then accelerated to its final value v_∞. However, since for the dust driven winds, that are investigated in this work, this acceleration is a result of the details of the dust condensation process, any input structure that already yields the acceleration in a velocity structure $v(r)$, also implies a particular evolution of the dust formation in the wind. Therefore, the use of such a structure would only suggest a higher degree of realism, without actually having it. Furthermore, when using a $v(r)$-structure (see e.g. Dirks 2000, p. 70) the problem occurs, that if the gas box runs through the thermodynamical dust-formation window at a point, where the wind velocity is still small, it stays there unrealistically long, because of the lack of acceleration. This leads to numerical problems, because in principle, the time steps would now have to be chosen so small, that the chemical balance between evaporation and growth in the nearly fully condensed material can be resolved. If the time steps are not adapted, the models become numerically unstable, leading to senseless results, and if adapted, the calculation time increases to unrealistic orders of magnitude. Thus, a constant wind close to the typical final velocities is assumed, which corresponds to a physical model, where the volume elements are "thrown" through the dust formation window. As a consequence, the resulting predictions for the location of the dust formation

zone, have nothing to say about possible locations of dust formation zones in real stellar winds, but they are however comparable to each other, and adequate for answering such rough questions as

1. For what orders of magnitude of λ can the dust condensation process be treated in the micro/macro-turbulent limit case?

2. For what values of σ do the temperature fluctuations have a relevant impact on the dust condensation?

The high value of $[C/O] = 3$ was then chosen to obtain wind models, which are completely condensed at the outer boundary of the models.

5.2.3 The LTE-models

The model calculations presented in Sect. 4.1 reveal that the most important effect of the temperature fluctuations is the circumstance, that additional seed particles are "transported" from channels, where nucleation is already possible into channels, where nucleation is still impossible, but where the thermodynamic conditions are already favourable for grain growth. This results in an onset of nucleation at higher temperatures compared to the deterministic reference models. In contrast, the influence of the fluctuations on the growth process itself is comparably small.

The quantitative shift of the condensation zone in units of $R_\star$ can, however, not be regarded as relevant for realistic wind models, because of the shortcomings of the applied wind model, that was used as input for the thermodynamical structure of the wind. Nevertheless, the models give some insight about what "amplitude" the fluctuations should have, in order to have relevant influence on the dust condensation, and for which correlation times λ the problem can be treated in the micro- or macroturbulent limit case:

1. In the LTE-case, an rms temperature deviation of $\sigma \approx 20$ K is required to remarkably influence the condensation process.

2. The microturbulent limit case is reached at correlation times of $\lambda \approx 10^3 \ldots 10^4$ s, whereas the macroturbulent limit is reached at $\lambda \approx 10^7 \ldots 10^9$ s.

5.2.4 The NLTE-models

The models presented in Sect. 4.2 can be regarded as an upper limit case for the possible influence of temperature fluctuations on dust condensation, because inside the thermodynamic dust-forming window, the supersaturation

ratio depends a lot stronger on deviations between gas and dust temperature than on the temperature itself. Indeed, a strong influence on the dust condensation can be observed already for values of σ as small as $\sigma = 5$ K. However, the approximation $T_{\rm dust} = \overline{T}$, might be reasonable for macroscopic dust grains, that tend to be energetically coupled to the radiation field[1] in situations typical for AGB-winds, but is probably unrealistic for the small critical clusters, that are important for the calculation of the nucleation rate.

In principle, in a situation with a given gas and radiation temperature, one would expect a size dependent temperature distribution for the dust grains $T_{\rm dust}(N)$, which starts at $T_{\rm dust}(1) = T_{\rm gas}$ for the monomer and ends at $T_{\rm dust} \approx T_{\rm rad}$ for macroscopic grains. However, such a detailed treatment of the grain energy would also lead to size dependent growth rates $\tau^{-1}(N)$, which cannot be reconciled with a treatment of the dust complex using moments K_ρ of the distribution function $f(N,t)$. The determination of $T_{\rm dust}(N)$ is particularly difficult for the small critical clusters, because they are often of a size, where they cannot be treated as macroscopic particles and detailed absorption coefficients κ_ν would be required to calculate the exact energy balance with the surrounding radiation field. This would require furthermore a frequency dependent treatment of the radiative transfer, which might (by now) be possible, when directly resolving the fluctuations in a hydrodynamical code, which in turn would only make sense, when the correlation time of fluctuations is shorter than the numerical time steps of the corresponding code.

In that sense, the main results of the presented NLTE-models is, that the temperature of the critical cluster might have a relevant impact for the nucleation process already in a deterministic situation, but in particular under the influence of independent fluctuations of the gas temperature or the radiation field. However, no approach to obtain a more realistic model of the temperature of the critical cluster, which would allow an inclusion into the present numerical wind models is at sight.

5.3 Resume

The results from the gas box models presented in Section. 4 have shown that:

1. Fluctuations with correlation times $\lambda < 10^3 \ldots 10^4$ seconds can be treated in the microturbulent limit, and

2. the main impact of the fluctuations is that of an enhanced nucleation

[1] In this case the additional assumption $\overline{T} = T_{\rm rad}$ is applied.

at high temperatures, while the net growth rates do not react sensibly to the fluctuations.

The aim of this work was to find a method of including the effects of possible temperature fluctuations in the frame of existing time dependent model calculations of dust driven winds of AGB-stars. The longest time steps in these calculations are of the order of 10^3 seconds. Any fluctuations with a correlation time $> 10^3$ can therefore be resolved numerically and hydrodynamically within the framework of the existing numerical models and need no special treatment. Fluctuations which cannot be resolved numerically by the code, require a subgrid modelling, which can now be developed, guided by the results from Section. 4.

All fluctuations which are too fast for a numerical resolution in the time dependent calculation turn out to be definitely in the microturbulent regime with respect to the dust physics. A microturbulent treatment of the fluctuations in the framework of dynamical model calculations is therefore admissible. The fact that the main impact of the temperature fluctuations consists in a higher nucleation rate at higher temperatures, leaving the net growth rate relatively unchanged, suggests an approach that consists in the implementation of a microturbulent nucleation rate into the dynamical code, leaving the description of the growth rate unchanged. The advantages of this approach are:

- The necessary changes of the dynamical code are very restricted. Only a new routine for the calculation of the microturbulent nucleation rate has to be provided.

- The problems of calculating proper stochastic dust destruction rates, as described in Sect. 2.2.2, are evaded. Evaporation and growth are treated in the traditional way, which ensures a proper treatment of the dust destruction.

Chapter 6

The microturbulent nucleation rate

The required microturbulent nucleation rate J_{micro} is calculated by solving the Fokker-Planck equation (2.66) for q_0 in a gas box of constant T_{gas}, ρ and ϵ_{C} and subsequent evaluation of the results:

$$\begin{aligned} J_{\mathrm{micro}} &= E\left(\frac{\Delta q_0}{\Delta t}\right) \\ &= \int_{-\Delta T_{\max}}^{\Delta T_{\max}} p^T \left(\frac{q_{0,\mathrm{new}} - q_{0,\mathrm{old}}}{t_{\mathrm{step}}}\right) \mathrm{d}T. \end{aligned} \tag{6.1}$$

A value of 200 grid points along the T-axis has turned out to be a good choice. The number of time steps was chosen as twice the number of temperature grid points, which ensures that every "signal" from the boundary can comfortably reach every part of the grid during the calculation. The calculation must be carried out at least until the nucleation rate reaches a stationary value, which is satisfied without any problems with this choice of parameters. The correlation length was set to $\lambda = 10^{-1}$ seconds, which lies well within the microturbulent regime and the time step was set to $\lambda/100$. The microturbulent nucleation rate J_{micro}, was evaluated according to Eq. (6.1) on a 3D-grid for T_{gas}, ρ and ϵ_{C}, range and spacings are given in Table 6.1. A sequence of 2D-T_{gas}/ρ-slices for different values of σ is shown in Fig. 6.1. It can clearly be seen, that the dependence of J_{micro} on the density is by orders of magnitude weaker than the dependence on the temperature. Consequently, the number of table-points for the temperature was chosen larger than for the density. The influence of ϵ_{C} on J_{micro} is approximately linear (not shown), i.e. considerably weaker than the temperature dependence, but

Figure 6.1: The microturbulent nucleation rate $\log(J)$ in a $T_{\rm gas}/\log(\rho)$ plane for $\epsilon_{\rm C} \approx 5.3 \times 10^{-4}$, i.e. C/O ≈ 1.8. The temperature is given in Kelvin and the density in $[g/cm^3]$. The dashed lines correspond to nucleation rates of $\log(J) = -19$ and -25. Top left: deterministic rate, top right: $\sigma = 1$ K, middle left: $\sigma = 10$ K, middle right: $\sigma = 20$ K, bottom left: $\sigma = 40$ K, bottom right: $\sigma = 60$ K.

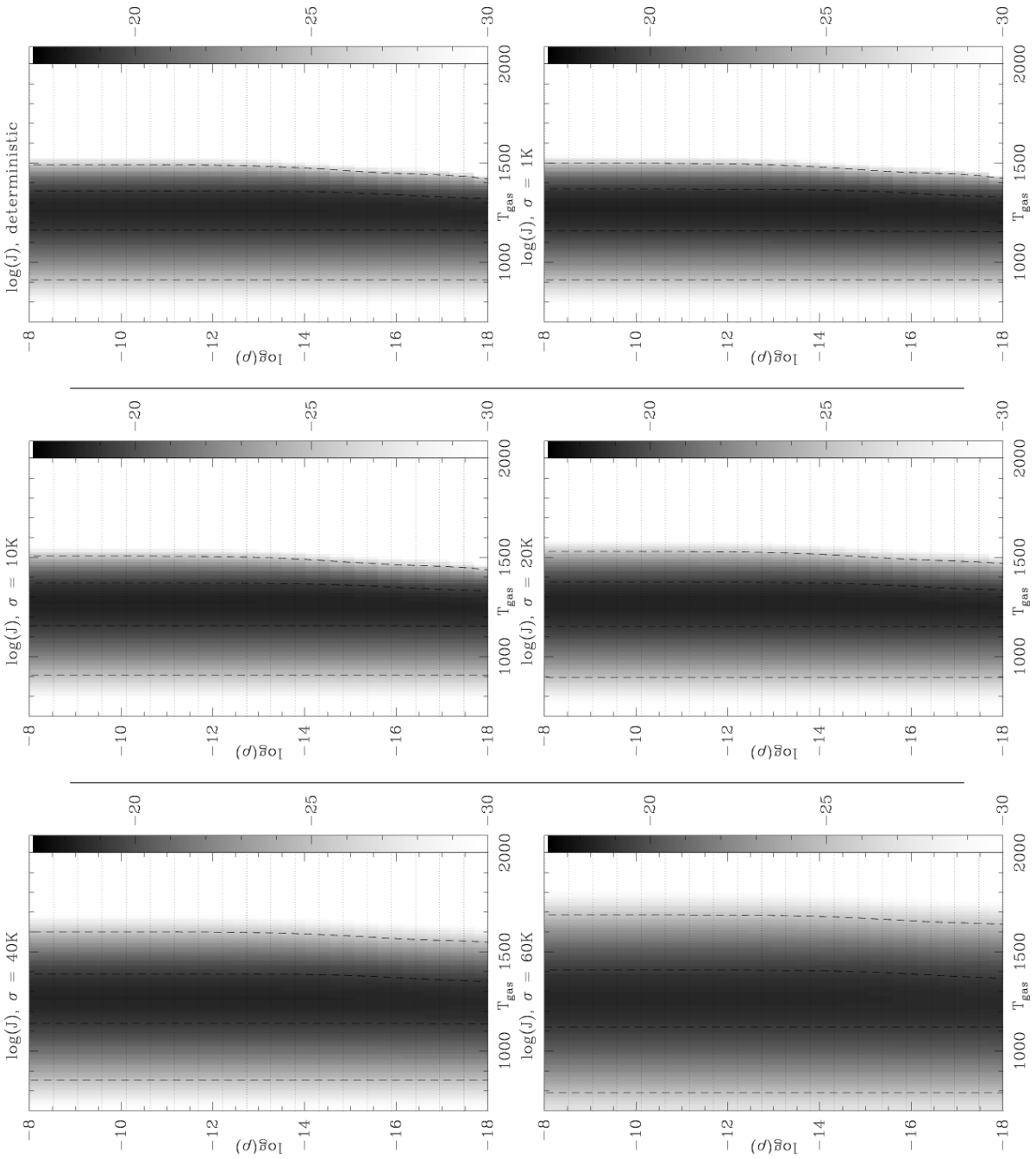

	lower edge	upper edge	No. of grid points	type of spacing
$T_{\rm gas}$	700 K	2000 K	100	linear
ρ	10^{-18} g/cm^{-3}	10^{-8} g/cm^{-3}	20	logarithmic
$\epsilon_{\rm C}$	0	5.3×10^{-4}	50	linear

Table 6.1: Range and spacing of the 3D-tables containing the microturbulent nucleation rates $J_{\rm micro}$

stronger than the density-dependence[1]. In Fig. 6.2 $J_{\rm micro}(T_{\rm gas})$ is represented for various values of σ and $\epsilon_{\rm C} = 5.3 \times 10^{-4}$, which corresponds to a dust free situation in a gas with a C/O-ratio of 1.8 for a solar oxygen abundance, and a density $\rho = 10^{-14}$ g/cm^{-3}. It can be seen, that the influence of the fluctuations results in overall higher values for the nucleation rates for most temperatures, but also in a slight decrease of the peak values. However, these peak values do not correspond to the nucleation peaks in a wind situation, because is by no means assured, that the thermodynamical structure of the wind will lead a volume element through the range of optimal nucleation, which corresponds to the peaks in Fig. (6.2). It is well possible, that in a wind situation depletion effects become important, before the optimum temperature for nucleation is reached.

[1]Note that $J_{\rm micro}$ is given in units of the particle density of hydrogen cores $n_{\hat{\rm H}}$. Therefore the dependence of this nucleation rate on the partial pressure of monomers manifests itself only in the dependence on the chemical abundance $\epsilon_{\rm C}$ and not in the dependence on the density ρ.

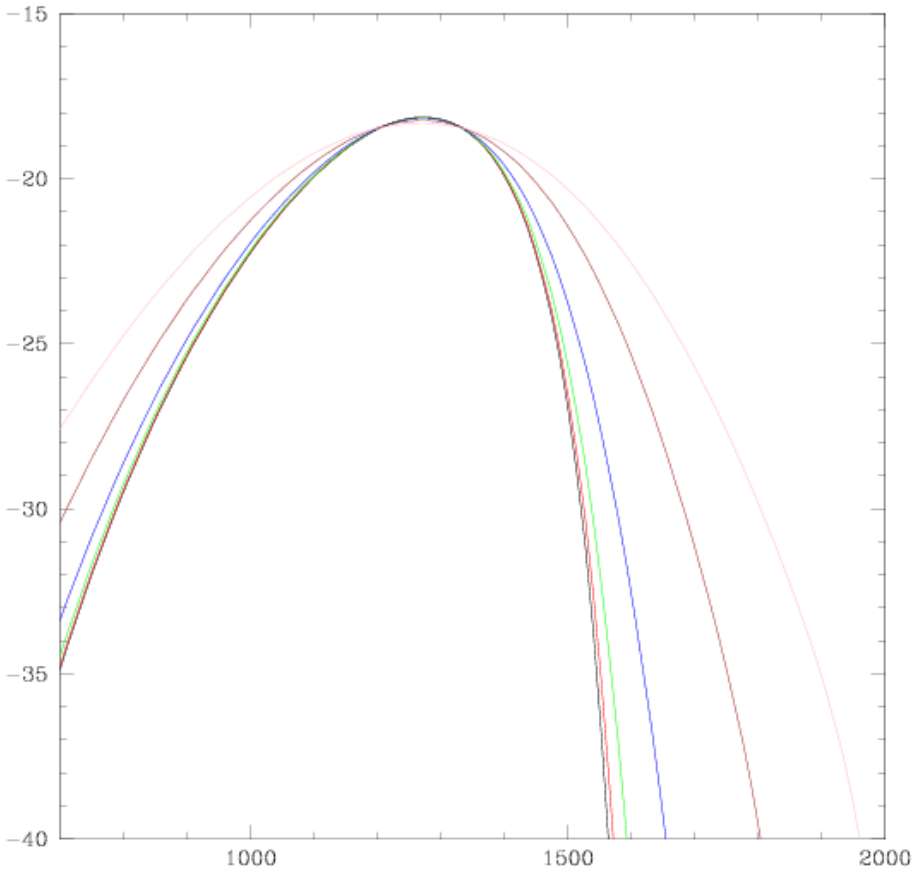

Figure 6.2: σ-study for J_{micro} for $\rho = 10^{-14}$ g/cm^{-3} and $\epsilon_{\text{C}} = 5.3 \times 10^{-4}$. $\sigma =$ 5K (red), 10K (green), 20K (blue), 40K (brown) and 60K (pink).

Chapter 7

Dynamical models of AGB-star winds

The tabulated microturbulent nucleation rate, calculated as described in Chapter 6, was included into the the CHILD-code, a code for the dynamical modeling of AGB-star winds, including a time dependent treatment of the dust complex. The CHILD-code was originally developed by Fleischer et al. (1992). The input physics of the code was described in Section 2.3, and the numerics in Section 3.4.

Some snapshots of the resulting wind structures are shown in Figs. 7.1, 7.2, 7.3, and 7.4. In each figure, four snapshots are represented for the deterministic reference model and for the same model calculated with a microturbulent nucleation rate for σ = 20 K, 40 K, and 60 K. Figs. 7.1, and 7.2 show models including tabulated NLTE-cooling and state functions (see Table 2.3, right column), while Figs. 7.3, and 7.4 show results for the same model parameters, but calculated using an analytical T^4-cooling and an ideal gas (see Table 2.3, left column). Figs. 7.1, and 7.3 were calculated with $\eta_{\rm opt} = 4.4\ {\rm K}^{-1}$, while Figs. 7.2, and 7.4 show the same models with $\eta_{\rm opt} = 5.9\ {\rm K}^{-1}$. The physical details of these figures will be discussed in Sect. 8.1. However, due to the complex dynamical structure of these objects, combined with some random behaviour due to the details of the particular numerical history, the analysis of particular snapshots can only be used to understand the overall physical behaviour of the models. For a quantitative analysis, quantities that are averaged over a large number of periods must be considered. Therefore, the final velocity v_∞ and the massloss rate $\dot{M}$ were calculated by averaging the corresponding values at $R = 20R_\star$ from $t = 90P$ to $t = 120P$; the results are given in Table 7.1, and Table 7.2. A quantitative analysis of these results is given and discussed in Sect. 8.2

In Table 7.1, a set of model calculations is presented for the analytical

T^4-cooling and the ideal gas model (see Table 2.3, left column). These models were calculated using a code in the version of Winters et al. (1997). A model is described by the following set of varying input parameters: T_* (effective temperature), $M_\star$ (stellar mass), $L_\star$ (stellar luminosity in the rest position of the piston), and σ (rms temperature deviation of the microturbulent fluctuation). Furthermore, the following additional input parameters have been set constant for all dynamical model calculations presented in this work: $[C/O] = 1.8$ (carbon to oxygen ratio), $P = 650$ days (stellar pulsational period), and $v_{\rm amp} = 2$ km/s (velocity amplitude of the piston at the inner boundary). For each set of parameters, two calculations (A and B) with a different value for $\eta_{\rm opt}$ have been performed, in order to investigate, whether the importance of the fluctuations varies with the coupling between dust and radiation field (A: $\eta_{\rm opt} = 4.4$ K^{-1}, Planck mean acc. to Winters et al. (1994a), B: $\eta_{\rm opt} = 5.9$ K^{-1}, Rosseland mean acc. to Gail & Sedlmayr (1985)).

In Table 7.2 a set of model calculations for the same set of parameters is presented for models with tabulated NLTE-cooling and state functions (see Table 2.3, right column). These models were calculated using a code in the version of Schirrmacher et al. (2003).

All numerical parameters were kept constant for all calculations presented in this work, i.e. no "fine-tuning" of the time step criteria was carried out. This has the advantage of making quantitative comparisons between the models of each set more reliable, but it also has the disadvantage, that quite a number of model calculations have failed during the starting phase, when the first few artificially high shock waves often create numerical problems. For these models, v_∞ and $\dot{M}$ have been marked by '(–)' in the tables.

Figure 7.1: Snapshots from the dynamical model calculations at $t = 90P$, model 12, NLTE-cooling, $\eta_{\rm opt} = 4.4$ K^{-1}. Top left: deterministic, top right: $\sigma = 20$ K, bottom left: $\sigma = 40$ K, bottom right: $\sigma = 60$ K. Represented quantities: top panel: velocity v (red), particle density of hydrogen cores $n_{\hat{\rm H}}$ (blue), panel 2: gas temperature $T_{\rm gas}$ (orange), radiation temperature $T_{\rm rad}$ (grey dashed), panel 3: nucleation rate J (light green), net growth rate τ^{-1} (dark green), panel 4: degree of condensation $f_{\rm c}$ (black), radiative acceleration α (blue).

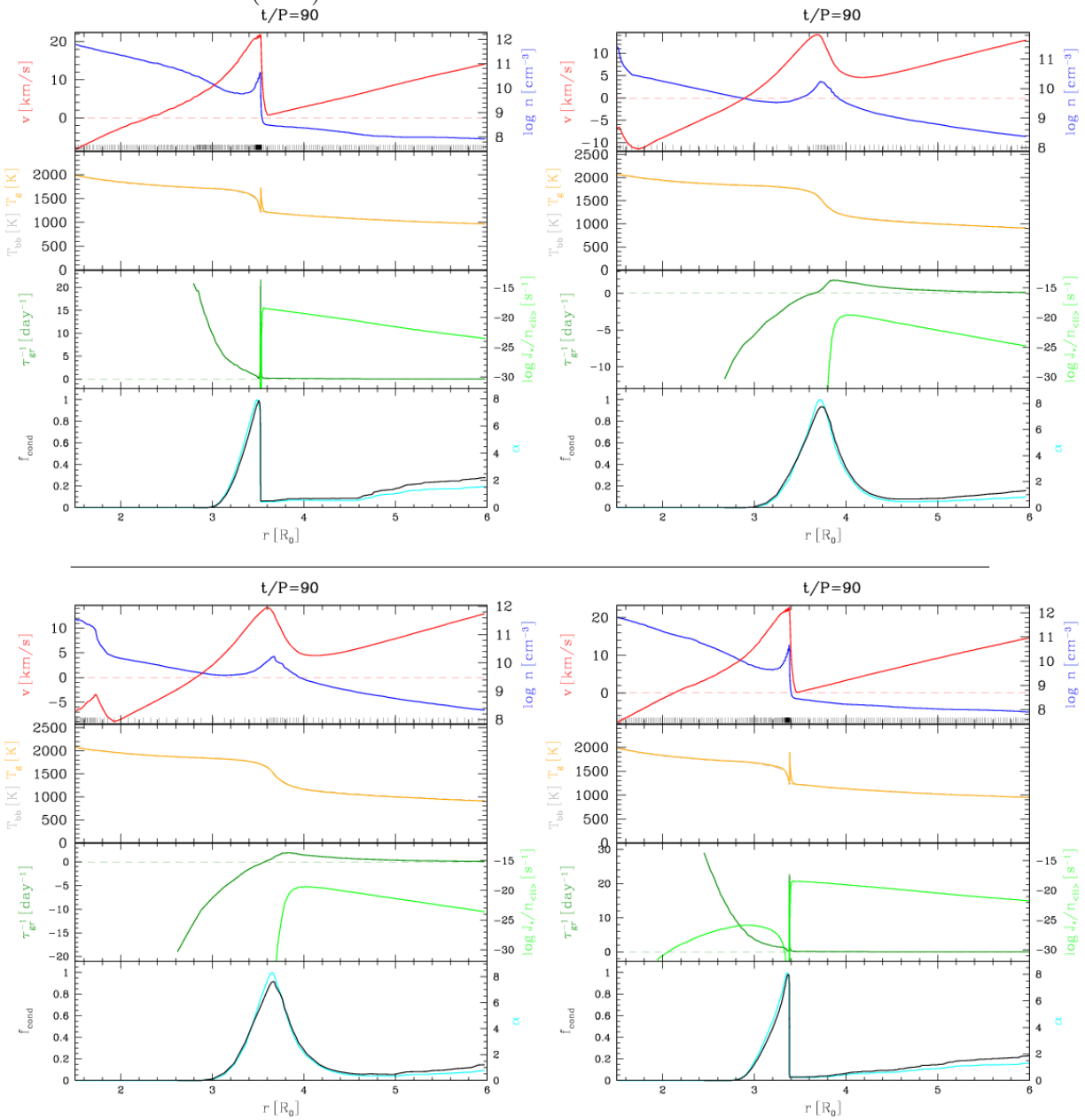

Figure 7.2: Snapshots from the dynamical model calculations at $t = 90P$, model 12, NLTE-cooling, $\eta_{\rm opt} = 5.9$ K^{-1}. Top left: deterministic, top right: $\sigma = 20$ K, bottom left: $\sigma = 40$ K, bottom right: $\sigma = 60$ K. Represented quantities: top panel: velocity v (red), particle density of hydrogen cores $n_{\hat{\rm H}}$ (blue), panel 2: gas temperature $T_{\rm gas}$ (orange), radiation temperature $T_{\rm rad}$ (grey dashed), panel 3: nucleation rate J (light green), net growth rate τ^{-1} (dark green), panel 4: degree of condensation $f_{\rm c}$ (black), radiative acceleration α (blue).

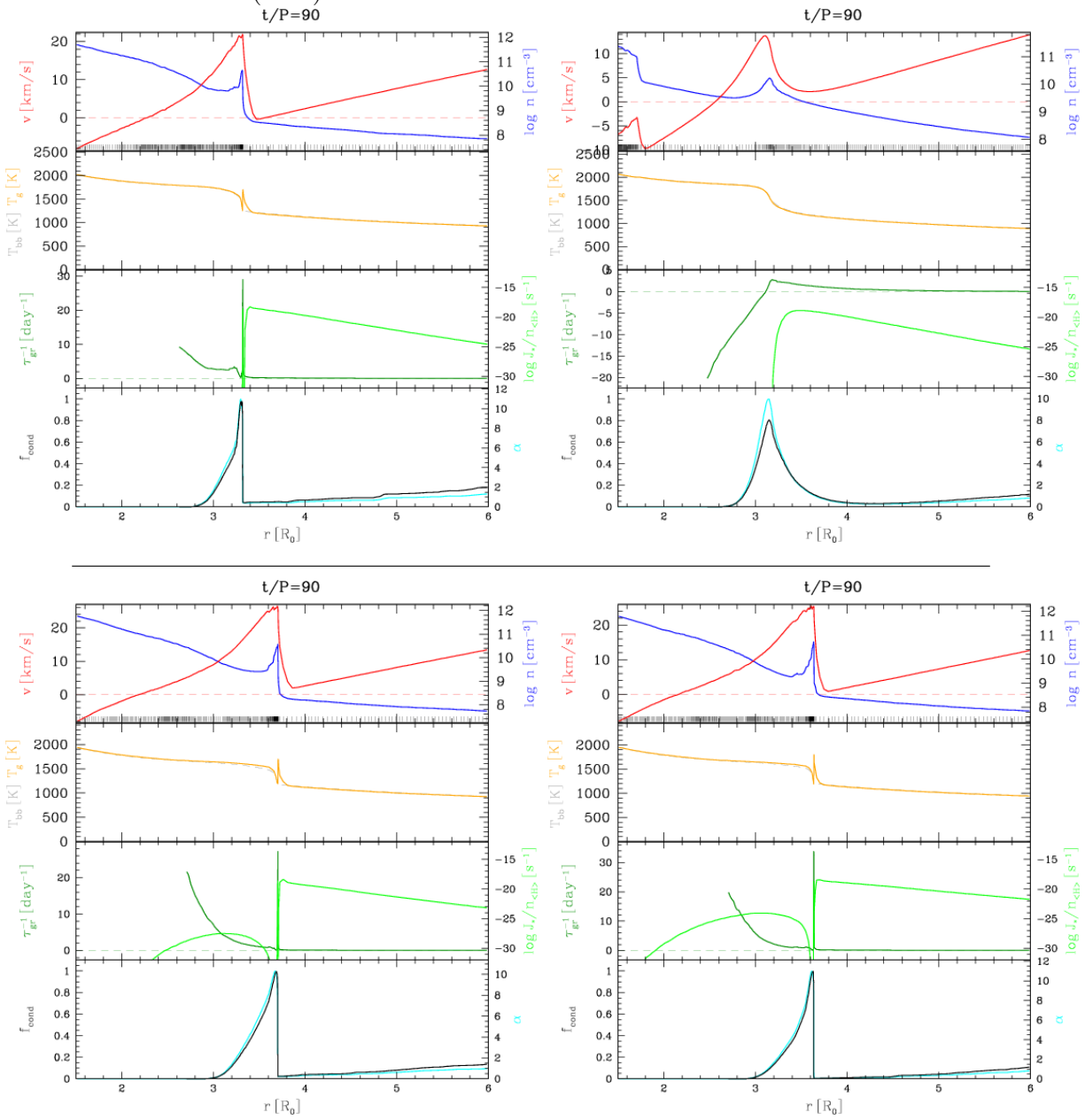

Figure 7.3: Snapshots from the dynamical model calculations at $t = 90P$, model 12, ideal gas, T^4-cooling, $\eta_{\rm opt} = 4.4$ K^{-1}. Top left: deterministic, top right: $\sigma = 20$ K, bottom left: $\sigma = 40$ K, bottom right: $\sigma = 60$ K. Represented quantities: top panel: velocity v (red), particle density of hydrogen cores $n_{\hat{\rm H}}$ (blue), panel 2: gas temperature $T_{\rm gas}$ (orange), panel 3: nucleation rate J (light green), net growth rate τ^{-1} (dark green), panel 4: degree of condensation $f_{\rm c}$ (black), radiative acceleration α (blue).

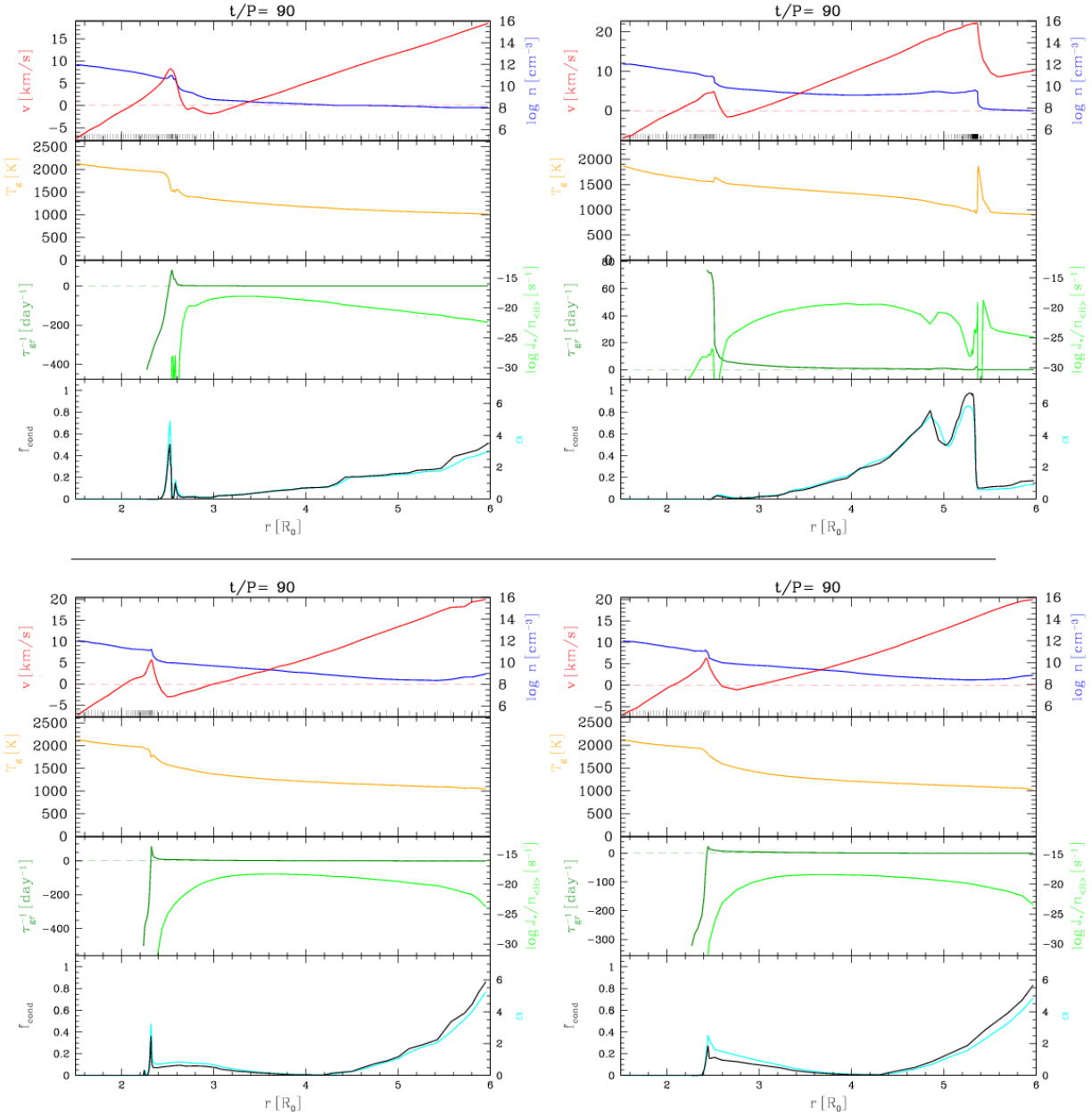

Figure 7.4: Snapshots from the dynamical model calculations at $t = 90P$, model 12, ideal gas, T^4-cooling, $\eta_{\rm opt} = 5.9$ K^{-1}. Top left: deterministic, top right: $\sigma = 20$ K, bottom left: $\sigma = 40$ K, bottom right: $\sigma = 60$ K. Represented quantities: top panel: velocity v (red), particle density of hydrogen cores $n_{\hat{\rm H}}$ (blue), panel 2: gas temperature $T_{\rm gas}$ (orange), panel 3: nucleation rate J (light green), net growth rate τ^{-1} (dark green), panel 4: degree of condensation $f_{\rm c}$ (black), radiative acceleration α (blue).

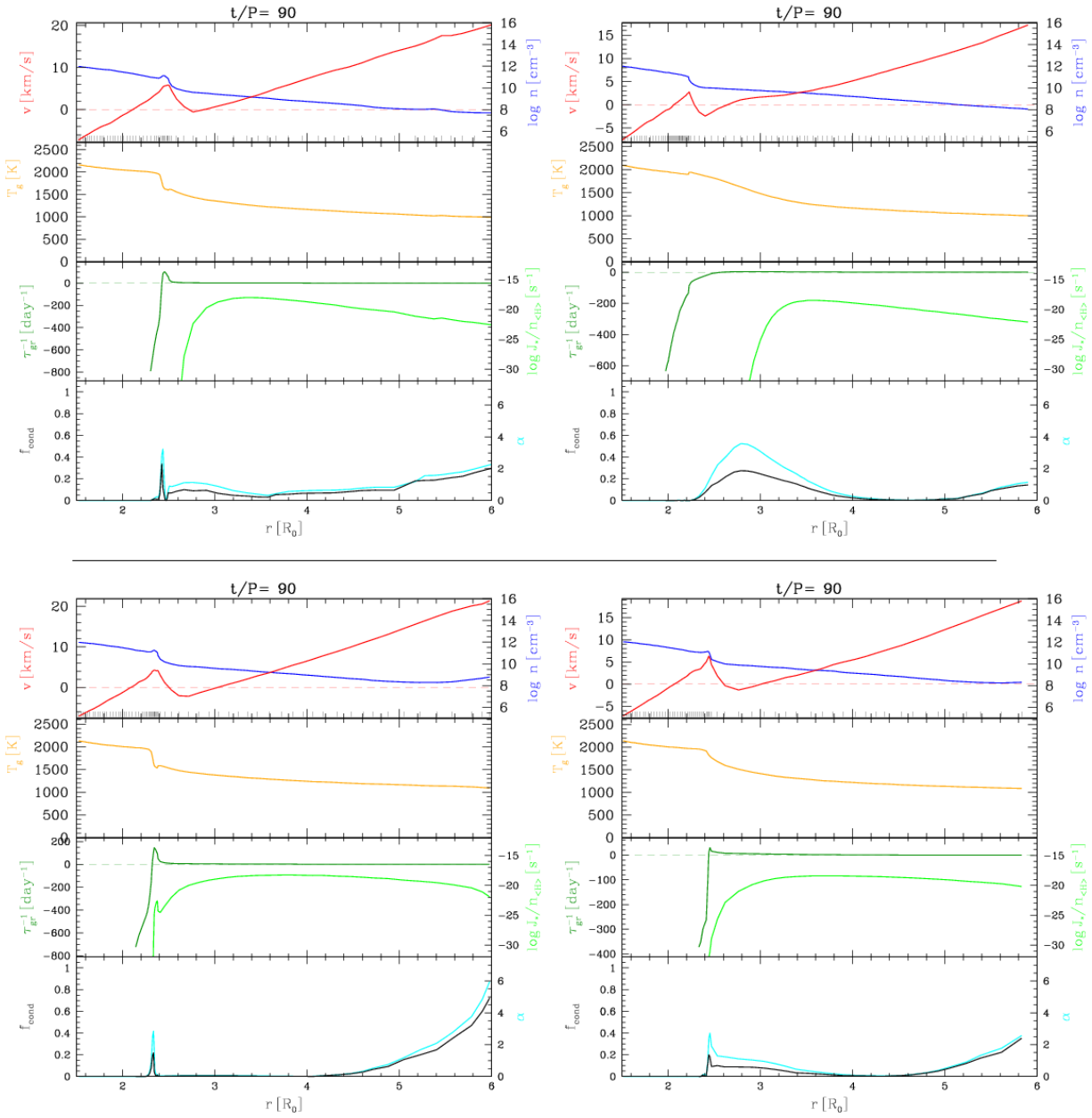

Table 7.1: Massloss-rates and final velocities for models with T^4-cooling, ideal gas

Model	$T_\star$[K]	$M_*/M_\odot$	$L_*/L_\odot$	σ[K]	v_∞[km/s]	$\dot{M}[M_\odot/\mathrm{yr}]$
0/E	2600	1.0	10^4	-	26.52	1.08×10^{-5}
				20	26.28	1.14×10^{-5}
A				40	26.08	1.21×10^{-5}
				60	(–)	(–)
				-	29.94	9.37×10^{-6}
B				20	28.87	9.84×10^{-6}
				40	29.71	1.08×10^{-5}
				60	(–)	(–)
1	2800	1.0	10^4	-	24.45	8.83×10^{-6}
				20	24.66	7.80×10^{-6}
A				40	25.02	8.68×10^{-6}
				60	(–)	(–)
				-	29.50	7.40×10^{-6}
B				20	28.50	8.11×10^{-6}
				40	28.44	8.34×10^{-6}
				60	(–)	(–)
2	3000	1.0	10^4	-	21.31	4.74×10^{-6}
				20	22.57	4.94×10^{-6}
A				40	25.43	5.29×10^{-6}
				60	(–)	(–)
				-	26.26	4.75×10^{-6}
B				20	25.30	5.20×10^{-6}
				40	28.11	5.56×10^{-6}
				60	(–)	(–)
3	2400	1.0	10^4	-	23.52	3.01×10^{-5}
				20	(–)	(–)
A				40	21.25	3.64×10^{-5}
				60	(–)	(–)
				-	24.89	2.91×10^{-5}
B				20	24.19	3.39×10^{-5}
				40	24.32	3.17×10^{-5}
				60	(–)	(–)

All models in this table have been calculated with a C/O-ratio of 1.8, a pulsation period of 650 days and a piston velocity of 2 km/s. A: $\eta_{opt} = 4.4$, B: $\eta_{opt} = 5.9$.

Massloss-rates and final velocities for models with T^4-cooling, ideal gas

Model	$T_\star$[K]	$M_*/M_\odot$	$L_*/L_\odot$	σ[K]	v_∞[km/s]	$\dot{M}[M_\odot/\mathrm{yr}]$
4	2600	1.0	8×10^3	-	23.05	9.52×10^{-6}
				20	22.66	1.06×10^{-5}
A				40	22.69	1.08×10^{-5}
				60	(–)	(–)
				-	26.35	9.29×10^{-6}
B				20	25.88	9.80×10^{-6}
				40	25.83	1.06×10^{-5}
				60	(–)	(–)
5	2600	1.0	6×10^3	-	19.39	1.04×10^{-5}
				20	19.75	7.87×10^{-6}
A				40	(–)	(–)
				60	(–)	(–)
				-	23.58	8.00×10^{-6}
B				20	22.97	8.58×10^{-6}
				40	23.23	7.70×10^{-6}
				60	(–)	(–)
6	2400	1.0	8×10^3	-	(–)	(–)
				20	21.83	2.10×10^{-5}
A				40	21.69	2.05×10^{-5}
				60	(–)	(–)
				-	(–)	(–)
B				20	24.19	1.91×10^{-5}
				40	24.81	2.08×10^{-5}
				60	(–)	(–)
7	2800	1.0	8×10^3	-	22.53	7.88×10^{-6}
				20	21.58	8.74×10^{-6}
A				40	22.84	6.62×10^{-6}
				60	(–)	(–)
				-	26.86	6.24×10^{-6}
B				20	25.02	6.37×10^{-6}
				40	25.61	7.42×10^{-6}
				60	(–)	(–)

All models in this table have been calculated with a C/O-ratio of 1.8, a pulsation period of 650 days and a piston velocity of 2 km/s. A: $\eta_{opt} = 4.4$, B: $\eta_{opt} = 5.9$.

Massloss-rates and final velocities for models with T^4-cooling, ideal gas

Model	$T_\star$[K]	$M_*/M_\odot$	$L_*/L_\odot$	σ[K]	v_∞[km/s]	$\dot{M}[M_\odot/\mathrm{yr}]$
8	3000	1.0	8×10^3	-	(–)	(–)
				20	(–)	(–)
A				40	(–)	(–)
				60	(–)	(–)
				-	(–)	(–)
B				20	(–)	(–)
				40	(–)	(–)
				60	(–)	(–)
9	3000	1.0	6×10^3	-	(–)	(–)
				20	(–)	(–)
A				40	(–)	(–)
				60	(–)	(–)
				-	(–)	(–)
B				20	(–)	(–)
				40	(–)	(–)
				60	(–)	(–)
10	2600	0.8	10^4	-	(–)	(–)
				20	(–)	(–)
A				40	23.96	2.79×10^{-5}
				60	24.00	2.82×10^{-5}
				-	(–)	(–)
B				20	26.93	2.43×10^{-5}
				40	26.63	2.56×10^{-5}
				60	26.64	2.72×10^{-5}
11	2800	0.8	10^4	-	27.41	9.81×10^{-6}
				20	26.62	1.07×10^{-5}
A				40	26.40	1.11×10^{-5}
				60	26.19	1.22×10^{-5}
				-	(–)	(–)
B				20	30.08	9.41×10^{-6}
				40	29.81	1.04×10^{-5}
				60	29.27	1.21×10^{-5}

All models in this table have been calculated with a C/O-ratio of 1.8, a pulsation period of 650 days and a piston velocity of 2 km/s. A: $\eta_{opt} = 4.4$, B: $\eta_{opt} = 5.9$.

Massloss-rates and final velocities for models with T^4-cooling, ideal gas

Model	$T_\star$[K]	$M_*/M_\odot$	$L_*/L_\odot$	σ[K]	v_∞[km/s]	$\dot{M}[M_\odot/\mathrm{yr}]$
12	3000	0.8	10^4	-	24.61	8.27×10^{-6}
				20	23.92	8.68×10^{-6}
A				40	24.86	8.88×10^{-6}
				60	24.97	1.01×10^{-5}
				-	28.28	7.35×10^{-6}
B				20	28.11	8.40×10^{-6}
				40	27.46	8.72×10^{-6}
				60	27.40	9.91×10^{-6}
13	2400	0.8	10^4	-	(–)	(–)
				20	(–)	(–)
A				40	(–)	(–)
				60	23.04	4.92×10^{-5}
				-	(–)	(–)
B				20	(–)	(–)
				40	23.48	4.92×10^{-5}
				60	25.55	4.87×10^{-5}
14	2600	0.8	8×10^3	-	23.92	1.52×10^{-5}
				20	23.63	1.64×10^{-5}
A				40	24.48	1.39×10^{-5}
				60	24.41	1.52×10^{-5}
				-	(–)	(–)
B				20	27.11	1.23×10^{-5}
				40	26.89	1.29×10^{-5}
				60	26.80	1.47×10^{-5}
15	2600	0.8	6×10^3	-	(–)	(–)
				20	20.76	1.21×10^{-5}
A				40	20.74	1.23×10^{-5}
				60	(–)	(–)
				-	24.12	9.76×10^{-6}
B				20	23.84	1.05×10^{-5}
				40	23.68	1.09×10^{-5}
				60	(–)	(–)

All models in this table have been calculated with a C/O-ratio of 1.8, a pulsation period of 650 days and a piston velocity of 2 km/s. A: $\eta_{opt} = 4.4$, B: $\eta_{opt} = 5.9$.

Massloss-rates and final velocities for models with T^4-cooling, ideal gas

Model	$T_\star$[K]	$M_*/M_\odot$	$L_*/L_\odot$	σ[K]	v_∞[km/s]	$\dot{M}[M_\odot/\mathrm{yr}]$
16	2400	0.8	8×10^3	-	(–)	(–)
				20	(–)	(–)
A				40	(–)	(–)
				60	(–)	(–)
				-	(–)	(–)
B				20	22.62	3.53×10^{-5}
				40	23.01	3.34×10^{-5}
				60	(–)	(–)
17	2800	0.8	8×10^3	-	23.16	9.22×10^{-6}
				20	22.87	9.86×10^{-6}
A				40	22.79	1.10×10^{-5}
				60	22.68	1.14×10^{-5}
				-	27.26	8.49×10^{-6}
B				20	26.74	9.59×10^{-6}
				40	26.88	1.02×10^{-5}
				60	26.70	1.00×10^{-5}
18	3000	0.8	8×10^3	-	24.38	4.87×10^{-6}
				20	23.27	7.57×10^{-6}
A				40	23.21	8.15×10^{-6}
				60	23.93	5.88×10^{-6}
				-	26.69	4.26×10^{-6}
B				20	25.98	4.95×10^{-6}
				40	26.08	7.26×10^{-6}
				60	26.65	5.87×10^{-6}
19	3000	0.8	6×10^3	-	19.63	8.37×10^{-7}
				20	19.36	8.67×10^{-7}
A				40	20.70	7.61×10^{-7}
				60	(–)	(–)
				-	23.65	7.47×10^{-7}
B				20	22.79	8.33×10^{-7}
				40	23.20	7.27×10^{-7}
				60	(–)	(–)

All models in this table have been calculated with a C/O-ratio of 1.8, a pulsation period of 650 days and a piston velocity of 2 km/s. A: $\eta_{opt} = 4.4$, B: $\eta_{opt} = 5.9$.

Table 7.2: Massloss-rates and final velocities, models with tabulated NLTE-cooling and state functions.

Model	$T_\star$[K]	$M_*/M_\odot$	$L_*/L_\odot$	σ[K]	v_∞[km/s]	$\dot{M}[M_\odot/\mathrm{yr}]$
0/E	2600	1.0	10^4	-	24.35	1.87×10^{-5}
				20	25.04	1.82×10^{-5}
A				40	24.55	1.69×10^{-5}
				60	24.52	1.63×10^{-5}
				–	27.50	1.73×10^{-5}
B				20	27.35	1.68×10^{-5}
				40	27.62	1.78×10^{-5}
				60	27.47	1.89×10^{-5}
1	2800	1.0	10^4	-	23.76	6.86×10^{-6}
				20	24.11	6.17×10^{-6}
A				40	24.34	8.94×10^{-6}
				60	24.45	1.01×10^{-5}
				–	26.76	1.01×10^{-5}
B				20	27.06	7.01×10^{-6}
				40	28.27	7.48×10^{-6}
				60	29.99	4.68×10^{-6}
2	3000	1.0	10^4	-	21.91	2.67×10^{-6}
				20	23.97	2.46×10^{-6}
A				40	26.36	3.83×10^{-6}
				60	26.12	4.05×10^{-6}
				–	26.01	2.02×10^{-6}
B				20	29.05	2.78×10^{-6}
				40	28.83	2.93×10^{-6}
				60	29.09	4.37×10^{-6}
3	2400	1.0	10^4	-	22.64	2.89×10^{-5}
				20	22.91	2.70×10^{-5}
A				40	23.31	2.71×10^{-5}
				60	(–)	(–)
				–	26.14	3.29×10^{-5}
B				20	27.00	2.30×10^{-5}
				40	26.92	2.06×10^{-5}
				60	(–)	(–)

All models in this table have been calculated with a C/O-ratio of 1.8, a pulsation period of 650 days and a piston velocity of 2 km/s. A: $\eta_{opt} = 4.4$, B: $\eta_{opt} = 5.9$.

Massloss-rates and final velocities, models with tabulated NLTE-cooling and state functions.

Model	$T_\star$[K]	$M_*/M_\odot$	$L_*/L_\odot$	σ[K]	v_∞[km/s]	$\dot{M}[M_\odot/\mathrm{yr}]$
4	2600	1.0	8×10^3	-	23.54	4.86×10^{-6}
				20	23.30	5.47×10^{-6}
A				40	24.90	3.87×10^{-6}
				60	(–)	(–)
				–	28.28	3.95×10^{-6}
B				20	28.71	4.00×10^{-6}
				40	28.67	3.07×10^{-6}
				60	(–)	(–)
5	2600	1.0	6×10^3	-	20.53	3.20×10^{-6}
				20	19.86	2.76×10^{-6}
A				40	20.89	4.47×10^{-6}
				60	(–)	(–)
				–	23.85	3.45×10^{-6}
B				20	24.22	3.45×10^{-6}
				40	23.30	3.54×10^{-6}
				60	(–)	(–)
6	2400	1.0	8×10^3	-	22.41	2.16×10^{-5}
				20	22.29	2.21×10^{-5}
A				40	22.15	2.32×10^{-5}
				60	(–)	(–)
				–	25.36	1.93×10^{-5}
B				20	25.65	1.89×10^{-5}
				40	25.18	2.22×10^{-5}
				60	(–)	(–)
7	2800	1.0	8×10^3	-	22.61	4.00×10^{-6}
				20	23.73	3.50×10^{-6}
A				40	23.51	5.30×10^{-6}
				60	(–)	(–)
				–	25.93	4.79×10^{-6}
B				20	26.00	4.79×10^{-6}
				40	25.30	3.67×10^{-6}
				60	(–)	(–)

All models in this table have been calculated with a C/O-ratio of 1.8, a pulsation period of 650 days and a piston velocity of 2 km/s. A: $\eta_{opt} = 4.4$, B: $\eta_{opt} = 5.9$.

Massloss-rates and final velocities, models with tabulated NLTE-cooling and state functions.

Model	$T_\star$[K]	$M_*/M_\odot$	$L_*/L_\odot$	σ[K]	v_∞[km/s]	$\dot{M}[M_\odot/\mathrm{yr}]$
8	3000	1.0	8×10^3	-	19.16	$2,72 \times 10^{-7}$
				20	18.32	2.84×10^{-7}
A				40	17.41	4.34×10^{-7}
				60	(–)	(–)
				–	21.05	3.07×10^{-7}
B				20	19.16	3.17×10^{-7}
				40	20.71	4.99×10^{-7}
				60	(–)	(–)
9	3000	1.0	6×10^3	-	13.00	8.24×10^{-8}
				20	12.99	8.30×10^{-8}
A				40	13.03	8.20×10^{-8}
				60	(–)	(–)
				–	(–)	(–)
B				20	15.04	6.78×10^{-8}
				40	15.09	6.77×10^{-8}
				60	(–)	(–)
10	2600	0.8	10^4	-	26.32	1.19×10^{-5}
				20	26.89	1.07×10^{-5}
A				40	24.30	1.78×10^{-5}
				60	24.65	1.85×10^{-5}
				–	28.89	1.15×10^{-5}
B				20	29.54	1.04×10^{-5}
				40	27.10	1.77×10^{-5}
				60	27.73	1.76×10^{-5}
11	2800	0.8	10^4	-	24.02	8.40×10^{-6}
				20	25.31	1.05×10^{-5}
A				40	25.78	7.06×10^{-6}
				60	26.52	7.22×10^{-6}
				–	28.51	6.99×10^{-6}
B				20	28.19	4.93×10^{-6}
				40	28.53	9.06×10^{-6}
				60	29.64	5.05×10^{-6}

All models in this table have been calculated with a C/O-ratio of 1.8, a pulsation period of 650 days and a piston velocity of 2 km/s. A: $\eta_{opt} = 4.4$, B: $\eta_{opt} = 5.9$.

Massloss-rates and final velocities, models with tabulated NLTE-cooling and state functions.

Model	$T_\star$[K]	$M_*/M_\odot$	$L_*/L_\odot$	σ[K]	v_∞[km/s]	$\dot{M}[M_\odot/\mathrm{yr}]$
12	3000	0.8	10^4	-	25.53	9.22×10^{-6}
				20	25.41	8.90×10^{-6}
A				40	25.73	9.88×10^{-6}
				60	25.90	8.62×10^{-6}
				–	27.55	8.54×10^{-6}
B				20	27.77	8.23×10^{-6}
				40	29.04	7.50×10^{-6}
				60	28.76	6.62×10^{-6}
13	2400	0.8	10^4	-	22.48	3.98×10^{-5}
				20	23.92	2.97×10^{-5}
A				40	22.19	4.60×10^{-5}
				60	23.70	3.26×10^{-5}
				–	24.68	5.27×10^{-5}
B				20	25.79	3.41×10^{-5}
				40	(–)	(–)
				60	25.75	3.27×10^{-5}
14	2600	0.8	8×10^3	-	22.73	1.27×10^{-5}
				20	22.71	1.35×10^{-5}
A				40	23.49	9.85×10^{-6}
				60	23.08	1.39×10^{-5}
				–	26.70	1.12×10^{-5}
B				20	26.47	1.08×10^{-5}
				40	26.53	1.00×10^{-5}
				60	26.32	8.58×10^{-6}
15	2600	0.8	6×10^3	-	20.49	9.94×10^{-6}
				20	20.56	9.46×10^{-6}
A				40	20.46	8.13×10^{-6}
				60	(–)	(–)
				–	23.61	9.35×10^{-6}
B				20	23.32	9.84×10^{-6}
				40	24.74	4.38×10^{-6}
				60	(–)	(–)

All models in this table have been calculated with a C/O-ratio of 1.8, a pulsation period of 650 days and a piston velocity of 2 km/s. A: $\eta_{opt} = 4.4$, B: $\eta_{opt} = 5.9$.

Massloss-rates and final velocities, models with tabulated NLTE-cooling and state functions.

Model	$T_\star$[K]	$M_*/M_\odot$	$L_*/L_\odot$	σ[K]	v_∞[km/s]	$\dot{M}[M_\odot/\mathrm{yr}]$
16	2400	0.8	8×10^3	-	(–)	(–)
				20	22.72	2.14×10^{-5}
A				40	22.27	2.25×10^{-5}
				60	22.71	2.09×10^{-5}
				–	25.58	2.15×10^{-5}
B				20	25.43	1.96×10^{-5}
				40	25.65	2.09×10^{-5}
				60	25.20	2.40×10^{-5}
17	2800	0.8	8×10^3	-	22.50	9.26×10^{-6}
				20	22.93	8.67×10^{-6}
A				40	22.80	8.78×10^{-6}
				60	23.86	7.40×10^{-6}
				–	25.90	7.49×10^{-6}
B				20	25.84	7.10×10^{-6}
				40	26.87	7.13×10^{-6}
				60	27.03	6.91×10^{-6}
18	3000	0.8	8×10^3	-	22.52	4.05×10^{-6}
				20	24.57	3.76×10^{-6}
A				40	24.63	3.94×10^{-6}
				60	23.80	3.60×10^{-6}
				–	25.52	3.80×10^{-6}
B				20	26.61	2.74×10^{-6}
				40	26.74	3.73×10^{-6}
				60	25.80	4.16×10^{-6}
19	3000	0.8	6×10^3	-	19.94	5.40×10^{-7}
				20	20.18	5.03×10^{-7}
A				40	22.10	4.87×10^{-7}
				60	(–)	(–)
				–	25.69	1.72×10^{-6}
B				20	25.87	1.71×10^{-6}
				40	23.74	5.21×10^{-7}
				60	(–)	(–)

All models in this table have been calculated with a C/O-ratio of 1.8, a pulsation period of 650 days and a piston velocity of 2 km/s. A: $\eta_{opt} = 4.4$, B: $\eta_{opt} = 5.9$.

Chapter 8

Discussion of the dynamical wind models

An overview over the basic physical processes dominating the overall appearance of the wind models presented in Chapter 7 is given in Sect. 8.1. A quantitative analysis of the resulting mean massloss rates is presented in Sect. 8.2.

8.1 General overview

At first, it should be remarked, that nearly all models that did not run through the entire integration period of 120 P "died" at a very early stage of the integration – usually within the very first period – because the first shock front that evolves when the piston is applied to the hydrostatic start model reaches unphysically high velocities. This is a well known behaviour, and can in principle be tackled by some "fine-tuning" of the numerical parameters. For the code version using the NLTE-cooling and state functions, this fine-tuning was made some years ago, when it was optimised for the analysis of strong shock waves presented in Schirrmacher et al. (2003). However, this "fine-tuning" is a very time consuming process, and at the moment, when it turned out that quite a number of models calculated using the ideal gas model with the analytical T^4-cooling rate failed to run, most models were already calculated. Since all models within the same set of calculations should be carried out with the same numerical parameters, for the models with T^4-cooling no numerical fine-tuning was carried out, and each model family was calculated with the same executable program-file. Most models that did not run, had either i) a comparably high effective temperature combined with a comparably low luminosity and a high stellar mass (e.g. models 8, and 9), a

situation which results in a hot compact star with a strong density decrease in the start model, which, in turn, leads to high shock fronts, or ii) comparably low effective temperatures combined with a low stellar mass and high luminosity (e.g. model 13), a situation where effective dust condensation already sets in in the starting model, which again results in a steep dust driven shock wave developing at the very beginning of the calculation. Furthermore, it turned out, that the models with $\sigma = 60$ K and $M_\star = 1 M_\odot$ did not run, which again can be interpreted as a combination of early onset of nucleation in a compact starting model.

As a general trend, it can be seen, that – as expected – models with low temperatures tend to higher massloss rates compared to "hot" models, as do models with high luminosity when compared to models with low luminosities. The influence of the mass can also be seen when comparing the corresponding models in Tables 7.1, and 7.2 (the models 10–19 correspond to the models 0–9 with a mass of $0.8 M_\odot$.) The models with a low mass have always higher massloss rates than the corresponding models with a higher mass.

In the following, the structures presented in Figs. 7.1, 7.2, 7.3, and 7.4 shall be discussed. For a more detailed discussion of the structures resulting from dynamical model calculations using the CHILD-code, see e.g. . Fleischer et al. (1992), Fleischer (1994), or Schirrmacher et al. (2003).

In the top panel of each plot, the velocity (red) and the particle density of hydrogen cores (blue) is plotted. The red dashed line represents $v = 0$, i.e. in regions where the velocity structure lies below the dashed line, the material is falling back to the star. The high peaks in the velocity structure correspond to shock waves, which result from pressure waves that were induced by the stellar pulsation and have steepened up in the decreasing density structure above the star. These shock waves accumulate the circumstellar material, which can be seen by the density peaks (blue) that coincide with the shock fronts.

Behind these shock fronts, high densities often coincide with temperatures favourable for dust condensation. Correspondingly, the peaks of the net growth rate τ^{-1} (dark green, panel 3) also coincide with the shock fronts. Dust is formed behind these fronts, which is then accelerated by radiation pressure on dust, as can be seen in the plot for the radiative acceleration α (light blue, panel 4), which is strongly coupled to the degree of condensation f_c (black, panel 4). Thus, the shock fronts are additionally accelerated by the radiation pressure on the newly formed dust grains. The energy dissipation of these shocks heats the gas (orange line, panel 2).

The next important feature is the backwarming effect, which means, that the material inside a newly formed dust shell is heated by the inward directed radiation emitted from that shell. This heating through backwarm-

ing inhibits the dust formation behind a dust shell and leads to the typical onion-like structures of several separated outward moving dust shells. The backwarming effect manifests itself as a step in the gas temperature (orange, panel 2) which usually follows the shock front.

The nucleation rate J (light green, panel 3) is plotted on a logarithmic scale, because of the very dynamical behaviour of this quantity with respect to the thermodynamical properties of the environment. Usually, the final dust particle density (not shown) of a dust shell is determined only by the a short time period around the moment, where the nucleation reaches its peak value. The plots of J in Figs. 7.1, 7.2, 7.3, and 7.4 can therefore only help answering such questions as whether relevant nucleation takes place at all, and in what situation the corresponding peak value is reached. However, since both, the coupling of the dust complex to the hydrodynamics (Eq. 2.86), and to the chemistry via depletion of condensable carbon (Eq. 2.6) depend only on the total amount of condensed carbon, and not on the number density of carbon grains, an exact quantitative evaluation of the interplay between nucleation and growth on the dust moments K_0, K_1 and K_2 yields no important insights on the overall structure of the wind.

Due to the sensitive dependence of the nucleation rate on the details of the dynamical situation, no obvious trend for the influence of the rms temperature deviation of the microturbulent fluctuations σ can be seen in any of the figures, because the singular structures at a particular moment in time are of a much too individual nature.

With respect to the influence of the dust extinction, parametrised by η_{opt}, the comparison between the shock waves in Figs. 7.1, and 7.2, which are all approximately at a similar distance from the star, reveals that – as expected – the radiative acceleration α (blue, panel 4) reaches higher values for a higher dust extinction. The same trend is valid for the models in Figs. 7.3, and 7.4, even if not visible in the presented snapshots, because no comparable dust shells can be seen at the particular represented moment.

When comparing the two different approaches for gas model and cooling functions, the model in Fig. 7.1 (tabulated NLTE-cooling and state functions) corresponds to the model in Fig. 7.3 (T^4-cooling function, ideal monoatomic gas) and the model in Fig. 7.2 to the one in Fig. 7.4. Apparently, both model families show a different phase shift between the stellar pulsation and the details of the dust condensation, which makes a detailed comparison of the presented snapshots difficult (a detailed analysis of the influence of the NLTE-cooling and state functions is given in Schirrmacher et al. (2003)).

8.2 Quantitative analysis

Due to the complex nonlinear coupling of the processes in an AGB-wind a comparative quantitative analysis of "snapshots" (like those presented in Section. 8.1) from different model calculations is very hard to interpret, because the details of every hydro- and thermodynamical structure cannot be described by a manageable amount of variables. In order to gain some insights on the overall influence of the temperature fluctuations, in this section an analysis of the averaged massloss rates will be presented. The mean massloss rate is an adequate quantity for such an analysis, because it is a physically meaningful quantity describing the entire model calculation. Furthermore, the massloss rate is the important resulting quantity of these dynamical wind models with respect to a subsequent implementation to stellar evolution calculations (see Wachter 2007), and – in contrast to the detailed hydrodynamical structure – the massloss rate is an observable quantity.

For the quantitative evaluation, the ratios between the stochastic and deterministic mass loss rates have been calculated according to

$$\chi_{20} = \frac{\dot{M}_{\sigma=20\mathrm{K}}}{\dot{M}_{\mathrm{det}}}, \tag{8.1}$$

$$\chi_{40} = \frac{\dot{M}_{\sigma=40\mathrm{K}}}{\dot{M}_{\mathrm{det}}}, \tag{8.2}$$

$$\chi_{60} = \frac{\dot{M}_{\sigma=60\mathrm{K}}}{\dot{M}_{\mathrm{det}}}. \tag{8.3}$$

These ratios were averaged over the models for which they could be calculated. The results are presented in Table 8.1, the models using the tabulated NLTE-cooling rates and state functions calculated in statistical equilibrium are referred to as "NLTE-cooling and state functions" (see Table 2.3, right column). N_{sample} denotes the number of different χ_σ, that were used for the averaging process. The quantity $\sigma_{n-1}(\chi_\sigma)$ stands for the standard deviation of χ_σ.

The results reveal that for the models calculated using the ideal gas model and T^4-cooling, a clear trend of increasing massloss rates with an increasing σ establishes, while for the models with the NLTE-cooling rates and state functions such a trend can not really be seen. For some samples of these models, the inclusion of the microturbulent nucleation rate even seems to reduce the massloss rates. This is not a selection effect, because of the models that did not run for the T^4-cooling models. For the models using NLTE-cooling and state functions, the nonlinear coupling of the equation system describing the wind is a lot stronger, because pressure p and internal

Table 8.1: Relative changes of the massloss rates under the influence of the temperature fluctuations.

T^4-cooling, ideal gas, $\eta_{\rm opt} = 4.4$ K^{-1}			
σ	$\bar{\chi_\sigma}$	$N_{\rm sample}$	$\sigma_{n-1}(\chi_\sigma)$
20	1.07	12	0.18
40	1.11	12	0.21
60	1.18	5	0.10
T^4-cooling, ideal gas, $\eta_{\rm opt} = 5.9$ K^{-1}			
σ	$\bar{\chi_\sigma}$	$N_{\rm sample}$	$\sigma_{n-1}(\chi_\sigma)$
20	1.08	13	0.04
40	1.16	12	0.19
60	1.30	3	0.11
NLTE-cooling and state functions, $\eta_{\rm opt} = 4.4$ K^{-1}			
σ	$\bar{\chi_\sigma}$	$N_{\rm sample}$	$\sigma_{n-1}(\chi_\sigma)$
20	0.97	19	0.11
40	1.09	19	0.26
60	1.05	12	0.31
NLTE-cooling and state functions, $\eta_{\rm opt} = 5.9$ K^{-1}			
σ	$\bar{\chi_\sigma}$	$N_{\rm sample}$	$\sigma_{n-1}(\chi_\sigma)$
20	0.92	19	0.17
40	0.97	18	0.35
60	1.03	12	0.48

energy e depend not only on $T_{\rm gas}$ and ρ, but also directly on $T_{\rm rad}$ and and the mean velocity gradient $\left\langle \frac{{\rm d}v}{{\rm d}l} \right\rangle$, which makes the physical interpretation of the singular structures very difficult, especially if the general appearance as shown in Figs. 7.1, 7.2, 7.3, and 7.4 shows no striking differences neither at first nor at second sight. Therefore – unfortunately – the origin of the discrepancies between the values for χ_σ of the two model families remains unknown.

Chapter 9

Summary and Outlook

9.1 Summary

The influence of temperature fluctuations on the dust formation in AGB-winds has been investigated in order to find a way of implementing fluctuation effects into dynamical numerical model calculations.

As a first step, the temperature fluctuations were modelled as a stochastic Markovian process using the formalism developed by Dirks (2000), which allows the parametrisation of the fluctuation by the two parameters σ (rms temperature deviation) and λ (correlation time). This approach leads to a set of coupled Fokker-Planck equations for the conditional probabilities of the moments of the grainsize distribution function.

This set of Fokker-Planck equations was solved for a set of gas-box models, which roughly represent the hydro- and thermodynamic environment of an outward moving wind element in a cool, dust driven AGB-star wind. The results of these calculations were compared to Monte-Carlo calculations, which modelled particular representants of the stochastical process. The main impact of the temperature fluctuations turned out to be an increase of the effective nucleation rate caused by the "stochastic" injection of seed particles into the thermodynamical domain of moderate supersaturation, where no seeds would nucleate in the deterministic case. Furthermore the parameter space for σ and λ was investigated with the result, that

1. for temperature deviations with $\sigma > 20$ K, the fluctuations can remarkably influence the dust condensation,

2. for $\sigma > 60$ K, the numerical treatment by means of the Fokker-Planck equations becomes difficult, due to the large integration width along the T-axis, which is required to obtain reliable results,

3. for correlation times $\lambda < 10^4$ s, the fluctuation can be regarded as microturbulent within the frame of the thermodynamical situation in an AGB-star wind.

The last point of the above mentioned results from the gasbox calculations suggested that a microturbulent stochastical nucleation rate could serve as a subgrid model for a dynamical code, since all fluctuations that occur on time scales shorter than the longest time steps usually used in dynamical model calculations ($\approx 10^3$ s) turned out to be microturbulent. This has the advantage, that the microturbulent fluctuations can be described by one parameter only: the rms temperature deviation of the fluctuation σ.

Consequently, microturbulent nucleation rates were calculated and tabulated for various values of σ, and implemented into the CHILD-code developed by Fleischer et al. (1992), a code for the selfconsistent modelling of dynamical AGB-winds including hydrodynamics, thermodynamics, a grey radiative transfer, an equilibrium chemistry and a time dependent treatment of dust formation and destruction.

Dynamical model calculations have been performed for a sample of 20 sets of stellar parameters and $\sigma = 20, 40, 60$ K, and a deterministic reference for each model. Furthermore, all models have been calculated for two values of the dust extinction and for two different gas models: one model using the approach of an ideal monoatomic gas, combined with an analytical cooling rate, and another model using a more sophisticated approach, that consisted basically in the determination of all particle densities and energy exchange rates in statistical equilibrium (see Woitke 1997).

The resulting time-dependent wind models revealed, that for the first set of models, using the ideal gas model, an increase of the mean massloss rates of the order of about 5 to 30 per cent depending on the rms temperature deviation σ could be observed. For the second set of models, using the more sophisticated gas model, such an increase could not be deduced from the results of the model calculations.

9.2 Outlook

The concept of a microturbulent description of dust nucleation as presented in Chapter 6 can be applied to other numerical model calculations, that are used to model circumstellar envelopes of AGB-stars, as long as a deterministic dust description based on the moments of the grainsize distribution function by Gail et al. (1984) as described in Sect. 2.1 is already applied.

An application to other astrophysical situations, where dust formation takes place – e.g. the atmospheres of gas planets or Brown Dwarfs – would

require an investigation on whether the microturbulent formulation is admissible in the particular environment or not. Such an investigation could be performed on the basis of the stochastic formalism by Dirks (2000) as described in Sect. 2.2, if the following conditions are fulfilled:

1. A deterministic formulation of the thermo- and hydrodynamical environment is needed as input to gasbox calculations similar to those presented in Chapter 4 of this work.

2. A set of initial conditions for the (conditional) dust moments is required, in order to integrate both, the deterministic dust moment equations (2.5) as well as the set of Fokker-Planck equations (2.66) for the stochastic evolution of the dust moments.

For atmospheres that are in principle in hydrostatic[1] equilibrium, the first point includes the important problem of finding a time scale for the dust formation. In the case of a convective atmosphere of a Brown Dwarf, this time scale might be given by the convective motion of the gas elements. However, in this case, the problem arises, whether further turbulence can be expected *within* a given convection element or not. If this is the case, a subgrid formulation might be found, which allows to interpret the results of a subsequent application of the stochastic formalism as model for a concrete convection cell. If it cannot be assumed, that fluctuations occur within the particular convection element, the results would have to be interpreted as ensemble averages. Such ensemble averages will probably represent reasonable values for the mean density or temperature of the atmosphere, with respect to the details of the chemistry of a particular marker molecule, a hydro- and thermodynamical structure that results from an averaging process over an ensemble of possible situations might very well lead to completely wrong results.

The second point also yields some problems in the framework a hydrostatic atmosphere. Whereas in a wind situation, the start of the integration can easily be set so close to the star that a dust-free starting value can be expected, the choice of reasonable starting values can be very problematic within the context of a convective hydrostatic atmosphere. Again, if looking at particular convection elements, this problem could be solved by starting the integration sufficiently deep in the atmosphere, where the gas is hot enough to assure a dust-free situation, but whether this assumption is justified or not could be difficult to judge, because this would depend on the details of the applied convection theory. Another effect that might complicate

[1] "Hydrostatic" in this context means, that the object develops no stellar wind.

the situation in hydrostatic atmospheres are processes like the sedimentation of large dust grains which would not only complicate the treatment of the problem using moments of the grainsize distribution function, but could also lead to an additional injection of grains in deep, dust-free regions that would constitute an extra contribution to nucleation, which i) delivers seed particles that are larger than the critical cluster, and ii) could not be calculated by the thermodynamical properties of the "receiving" gas element alone, but would depend on the details of the dust-formation taking place in higher parts of the atmosphere, outside the convection element under consideration.

Danksagung

Mein Dank gilt zunächst Herrn Prof. Dr. Erwin Sedlmayr, der mir die Möglichkeit gegeben hat, diese Arbeit am Zentrum für Astronomie und Astrophysik der TU Berlin durchzuführen und sie durch viele hilfreiche Anregungen und Tips auch nach Kräften unterstützt hat. Weiterhin möchte ich Frau Prof. Dr. Heike Rauer dafür danken, dass sie sich als Berichterin zur Verfügung gestellt hat, sowie Herrn Prof. Dr. Harald Engel dafür, dass er sich bereit erklärt hat, den Vorsitz über den Promotionsausschuß zu übernehmen.

Ohne die Kollegen am ZAA Berlin, die diese Arbeit durch zahllose Gespräche, Tips und Diskussionen unterstützt haben haben, wäre diese Arbeit gewiß auch kaum denkbar gewesen. Darum, in alphabetischer Reihenfolge, Vielen Dank an Thorsten Arndt, Uwe Bolick, Christian Chang, Claudia Dreyer, Michael Hegmann, Christiane Helling, Kyung Sook Jeong, Marcus John, Jens Kaufmann, Claudia Kieschke, Marcus Lüttke, Beate Patzer, Sime Pervan, Heike Richter, Akemi Tamanai, Uwe Theil, Astrid Wachter, Jan-Martin Winters und Peter Woitke. Auch Herrn Prof. Dr. Kegel möchte ich für alle Tips, Gespräche und Anregungen herzlich danken und natürlich Uli Dirks, der mit seiner Arbeit nicht nur die Grundlagen geschaffen hat, auf denen ich aufbauen konnte, sondern sich auch immer wieder Zeit genommen hat, diese mit mir zu diskutieren.

Ganz besonderer Dank geht natürlich an meine Mutter Brigitte, ohne die hier gar nix gelaufen wäre, und an Tanja, die mich während der letzten Monate tapfer ertragen und motiviert hat.

Bibliography

Alexander, D. R., Johnson, H. R., & Rypma, R. L. 1983, ApJ, 272, 773

Allen, C. W. 1973, Astrophysical Quantities (London: The Athlone Press)

Arndt, T. U., Fleischer, A. J., & Sedlmayr, E. 1997, A&A, 327, 614

Böger, R., Kegel, W., & Hegmann, M. 2003, A&A, 406, 23

Bowen, G. H. 1988, ApJ, 329, 299

Burden, R. & Faires, J.-D. 2001, Numerical analysis, 7th edn. (Pacific Grove, CA, USA: BROOKS/COLE)

Chase Jr., M. W., Davies, C. A., Downey Jr., J. R., et al. 1985, JANAF Thermochemical Tables (National Bureau of Standards)

Dirks, U. 2000, PhD thesis, Technische Universität Berlin, Germany

Dorfi, E. A. & Höfner, S. 1991, A&A, 248, 105

Feder, J., Russell, K. C., Lothe, J., & Pound, G. M. 1966, Adv. Phys., 15, 111

Feuchtinger, M. U., Dorfi, E. A., & Höfner, S. 1993, A&A, 273, 513

Fleischer, A. J. 1994, PhD thesis, Technische Universität, Berlin, Germany

Fleischer, A. J., Gauger, A., & Sedlmayr, E. 1992, A&A, 266, 321

—. 1995, A&A, 297, 543

Gail, H.-P., Kegel, W. H., & Sedlmayr, E. 1975a, A&A, 42, 81

Gail, H.-P., Keller, R., & Sedlmayr, E. 1984, A&A, 133, 320

Gail, H.-P. & Sedlmayr, E. 1974, A&A, 36, 17

—. 1984, A&A, 132, 163

—. 1985, A&A, 148, 183

—. 1987a, A&A, 171, 197

—. 1987b, A&A, 177, 186

—. 1988, A&A, 206, 153

Gail, H.-P., Sedlmayr, E., & Traving, G. 1975b, A&A, 44, 421

—. 1976, A&A, 46, 441

—. 1980, JQSRT, 23, 267

Gauger, A., Gail, H.-P., & Sedlmayr, E. 1990, A&A, 235, 345

Gautschy-Loidl, R., Höfner, S., Jørgensen, U. G., & Hron, J. 2004, A&A, 422, 289

Goeres, A. 1993, Rev. Mod. Astron., 6, 165

Goeres, A. & Sedlmayr, E. 1992, A&A, 265, 216

Hashimoto, O. 1995, ApJ, 442, 286

Helling, C. 1999, PhD thesis, Technische Universität Berlin, Germany

Helling, C., Klein, R., Woitke, P., & Nowak, U. Sedlmayr, E. 2003, A&A, submitted

Helling, C., Oevermann, M., Lüttke, M., Klein, R., & Sedlmayr, E. 2001, A&A, 376, 194

Höfner, S. & Dorfi, E. A. 1992, A&A, 265, 207

Höfner, S., Fleischer, A. J., Gauger, A., et al. 1996, A&A, 314, 204

Höfner, S., Gautschy-Loidl, R., Aringer, B., & Jørgensen, U. G. 2003, A&A, 399, 589

Hölzel, Knacke, & Parthey. 1968, Landolt-Börnstein: Zahlenwerte und Funktionen, Vol. Vb (Berlin, Heidelberg, New York: Springer-Verlag)

Jeong, K., Winters, J., Le Bertre, T., & Sedlmayr, E. 2003, A&A, 407, 191

Lucy, L. B. 1971, ApJ, 163, 95

—. 1976, ApJ, 205, 482

Morton, K. & Mayers, D. 1994, Numerical Solution of Partial Differential Equations (Cambridge University Press)

Patzer, A. B. C., Gauger, A., & Sedlmayr, E. 1998, A&A, 337, 847

Richtmyer, R. D. & Morton, K. W. 1967, Difference methods for initial-value problems, 2nd edn. (New York: John Wiley & Sons)

Schirrmacher, V., Woitke, P., & Sedlmayr, E. 2003, A&A, 404, 267

Sedlmayr, E. & Winters, J. M. 1997, Lecture Notes in Physics, Vol. 497, Stellar Atmospheres: Theory and Observations, ed. J.-P. De Greve, R. Blomme, & H. Hensberge (EADN Astrophysics School IX, Brussels, Belgium 1996: Springer), 89–131

Tscharnuter, W. M. & Winkler, K.-H. 1979, Comp.Phys.Comm., 18, 171

Unno, W. & Kondo, M. 1976, PASJ, 28, 347

Wachter, A. 2007, PhD thesis, Zentrum für Astronomie und Astrophysik, TU Berlin, Berlin, D

Winters, J. M., Dominik, C., & Sedlmayr, E. 1994a, A&A, 288, 255

Winters, J. M., Fleischer, A. J., Gauger, A., & Sedlmayr, E. 1994b, A&A, 290, 623

—. 1995, A&A, 302, 483

Winters, J. M., Fleischer, A. J., Le Bertre, T., & Sedlmayr, E. 1997, A&A, 326, 305

Woitke, P. 1997, PhD thesis, Technische Universität, Berlin, Germany

—. 2006, A&A, 452, 537

Woitke, P., Helling, C., Winters, J. M., & Jeong, K. S. 1999, A&A, 348, L17

Woitke, P., Krüger, D., Goeres, A., & Sedlmayr, E. 1994, AG Abstr. Ser., 10, 160

Wood, P. R. 1979, ApJ, 227, 220